

Nuclear excitation functions for medical isotope production:  
Targeted radionuclide therapy via natIr(d,2n)<sup>193m</sup>Pt

Hannah Lovise Okstad Ekeberg

June 2020



# Contents

<b>1 Targeted radionuclide therapy</b>	<b>5</b>
1.1 Particle interaction in tissue . . . . .	7
1.2 Production of radionuclides . . . . .	10
1.3 $^{193m}\text{Pt}$ as a potential therapeutic agent . . . . .	11
<b>2 General nuclear reaction theory</b>	<b>15</b>
2.1 Radioactive decay law . . . . .	15
2.2 Nuclear reactions and reaction cross sections . . . . .	17
2.2.1 Constraints in nuclear reactions . . . . .	19
2.2.2 Deuterons and stopping power . . . . .	21
2.3 Nuclear reaction models . . . . .	21
2.4 Detection and identification of radionuclides . . . . .	21
2.4.1 High purity Germanium detector . . . . .	21
2.4.2 Gamma-ray spectrum . . . . .	23
<b>3 Experimental setup</b>	<b>25</b>
3.1 Lawrence Berkeley National Laboratory's 88" Cyclotron . . . . .	25
3.2 The experiment . . . . .	25
3.2.1 Target design and foil characterization . . . . .	27
3.2.2 Irradiation of target stack . . . . .	27
3.2.3 Counting on high purity detectors . . . . .	29
<b>4 Analysis</b>	<b>33</b>
4.1 Gamma-ray spectroscopy . . . . .	33
4.1.1 Energy and peak-shape calibration . . . . .	33
4.1.2 Background subtraction . . . . .	35
4.2 Efficiency calibration . . . . .	35
4.3 End of beam activities . . . . .	36
4.4 Estimation of the beam current . . . . .	37
4.4.1 Variance minimization of the deuteron transport calculations . . . . .	39
4.5 Cross section measurements . . . . .	41
<b>5 Discussion</b>	<b>47</b>
5.1 Uncertainties . . . . .	47
5.2 Beam current variance minimization . . . . .	47
5.3 Cross section products . . . . .	49
5.3.1 Nickel products . . . . .	49
5.3.2 Copper products . . . . .	55
5.3.3 Iron products . . . . .	57
5.3.4 Iridium Products . . . . .	57
<b>A Statistics</b>	<b>65</b>

## CONTENTS

---

<b>B Tables</b>	<b>67</b>
B.1 Product nuclei, Q-values and gammarays . . . . .	67
B.2 Production cross sections . . . . .	74
B.2.1 $^{nat}Ir(d,x)$ . . . . .	74

# Chapter 1

## Targeted radionuclide therapy

All written in this chapter needs to be rewritten as a lot of the text is just copied from various citations.

Today, multiple options for treatment of cancerous tissue are available, such as chemotherapy, surgery, immunotherapy, external beam therapy, brachytherapy and targeted radionuclide therapy. The latter three are treatment types utilizing ionizing particles to induce damage to the DNA. In external beam therapy X-rays, high-energetic gamma-rays, or accelerated particles like protons and heavier ions are focused externally towards the tumor, and in brachytherapy an unsealed radioactive source (usually a wire or pellet containing for instance a  $\beta$ -emitter), is placed in proximity to tumor (handbook of nuclear chemistry, p. 2180). Targeted radionuclide therapy is an emerging alternative, which can deliver a cytotoxic level of dose to the site of disease (handbook of nuclear chemistry p. 2180). It offers a patient-specific treatment dependent on choice of radiopharmaceutical which targets a type of tumor or cell. A radiopharmaceutical consists of a radionuclide and a cell-targeting molecule called a tracer. Meanwhile brachytherapy and targeted radionuclide therapy are limited by the cancer location and the existence of metastasis, along with required knowledge of the tumor to maximise the dose over the tumor and minimizing the dose to healthy tissue (Handbook of nuclear chemistry, p. 2180), targeted radionuclide therapy utilizes radiopharmaceuticals which are typically injected intravenously and utilized the biochemical pathways in the body. thus with an appropriate tracer, targeted tissue with a high uptake of the radiopharmaceutical will receive a high dose, and healthy tissue can be spared [1].

A therapeutic agent needs to have the two components optimized for the radiation from the radionuclide to have a high probability of being deposited in the tumor, and ideally cytotoxic dose to all cancerous cells within a tumor and sparing all healthy cells. The decay mode and radiation range are in coherence with the size and location, as well as the geometry of the tumor, and ranges from multicellular, cellular and subcellular ranges are typically accomplished with beta, alpha and auger electrons, respectively. However, geometrical factors of both the distribution and the tumor itself can have a degree of variations in the dose distribution due to differences in cross fire dose and the fraction of the radiation bound to the cell that is deposited in the tumor. Particularly apparent for micrometastatic disease which presents as small cluster of tumor cells, magnifying the impact of these factors. In addition, it is important to achieve a homogeneous dose deposition within the tumor, so that regrowth from an untreated subpopulation will be avoided. For the radionuclide, along with range and decay mode, the half-life production method, chemistry and biological behavior are important characteristics (all above in paragraph: handbook p. 2180-2182). For the tracer, a rapid blood clearance and transport (6, p. 145) and high uptake and retention in the tumor (9. p. 2) (special curriculum p. 4) are important characteristics. It can target the desired cells by for instance a specific receptor, enzyme, membrane, transporters or antigens (6, p. 145). Radiometals are also used, which consists of a bifunctional chelator, which is a molecule containing molecules which can donate a lone pair of electrons, like nitrogen, oxygen or sulfur. If the radiometal has an oxidation state of  $3^+$ , it will be tightly bound by the chelator, and can be transported to the tumor (special curriculum p. 4-5).

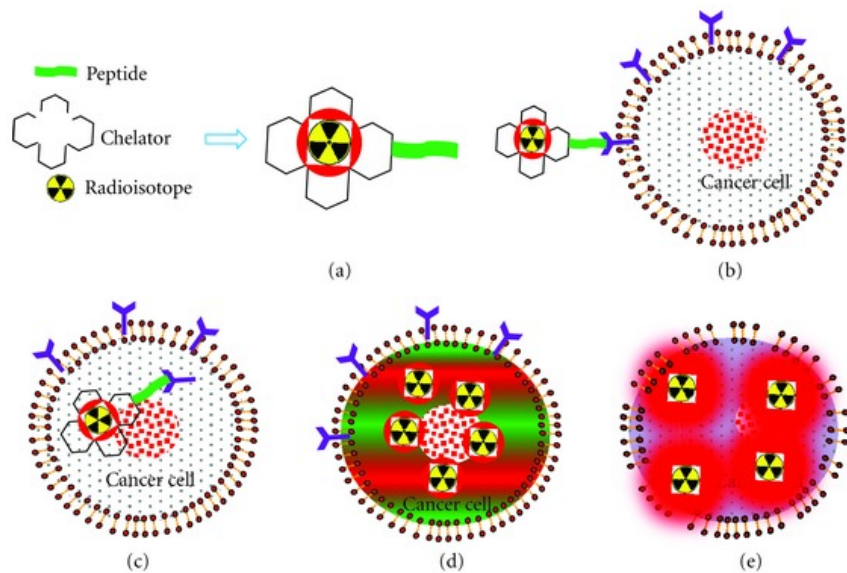


Figure 1.1: A radionuclide is bound to a chelating agent, and with a peptide, the radiopharmaceutical targets the cancer cells. Figure is from citation [8] in the special curriculum.

Figure 1.1 shows an illustration of how a radionuclide is attached to a chelator, and is transported to cancer cells with a specific peptide.

Whenever something is cited like (3), it means citation 3 in special curriculum Special curriculum p. 4: as mentioned above there are many requirements before a radiopharmaceutical can be used clinically, there are physical properties concerning the radionuclide, such as physical half-life, decay-mode and decay product, radiation energy and in-tissue range, and biological properties concerning the tracer such as tissue targeting, biological half-life, retention in tumor and the uptake in healthy tissue (3). Thus, the radiopharmaceutical requires two components in which complement each other to deposit the dose in the cancerous tissue.

In nuclear medicine, the effective half-life of the radiopharmaceutical is important as it takes both the physical half-life and the time it takes for the radiopharmaceutical to be cleared or excreted from the body (3). Thus it should be long enough to permit radiosynthesis and quality control (handbook, chapter targeted radionuclide therapy). Should be compatible with the pharmacokinetics of localization in tumor and clearance from normal tissue. However, as for therapy, high radiation dose is desired, which is easier to achieve with shorter half life, so that should also be compensated for. The choice of radionuclide should match the uptake rate and the retention, to avoid radioactive waste handling and dose to healthy tissue (3). Therapeutic radionuclides typically have half-lives in order of a few hours to several days (9, p. 1) (special curriculum p. 4).

Knowledge about the decay products are also important, if unstable, how it the dose distributed, and how long range, half life etc, and if unstable, is the daughter contributing to a cytotoxic effect, or taking part of the natural processes in the body.

In addition, the chemical-biological properties are important, as it must be chemically possible to attach radionuclide to the targeting molecule. Also, the bond must be stable in the body, over a time period which is stable as long as the physical half life. (handbook p. 2185)

Along with the ability to use radionuclides in therapy, radionuclides can also be used for diagnostic purposes with imaging, either with positron emitters (positron emission tomography) in which annihilates with atomic electrons close to the site of decay, and sends out two 511 keV photons, or emission of a strongly fed gamma-decay energy which is detected (single photon emission tomography). The combination of a diagnostic and a therapeutic agent with similar properties so that the biochemical

uptake in the body is a new approach in which can give information of how the uptake is distributed in the body, and can image the state of decease after therapies (The beginning and development of the theranostic approach in nuclear medicine.... 86/90Y). This is called theranostics..

## 1.1 Particle interaction in tissue

Ionizing radiation are particles with sufficient energy to cause ionizations along the particle track, thus separating an atom and one or more electrons. The free electron(s) can ionize further, and the positive ion can cause undesired reactions. DNA is a large molecule with two strands bound in a double helix structure. Each strand is composed of sugar and phosphate groups, and nitrogenous bases which bind the two strands (biobook p. 11). These bases are called adenine & guanine and cytosine & thymine (always bound pairwise), and are bound through weak hydrogen bonds which are exposed for strand breaks. The cell is equipped with an impressive repair mechanism, and unless both strands of the DNA is damaged, called a double stranded break (DSB), most damages are repaired. Radiation damages in the DNA can be caused directly by the ionizing particle or indirectly via free radicals, which are subject to other ionizations. Since the body contains large amounts of water, ionization of water molecules giving for instance  $H^\bullet$  or  $OH^\bullet$  are important damaging factors. Damages induced in the DNA can be lethal to the cell and either cause apoptosis or mutation in which can cause cancer. In therapy, the goal is to make malignant cells to undergo apoptosis, thus DNA is referred to as the target (book, p. 9). Choosing a particle with a high probability of inducing damage will induce multiple double stranded breaks if passing near by (special curriculum).

Linear energy transfer (LET) describes the energy absorbed by the medium, and is defined as the average energy (typically in keV) deposited per unit length (typically measured in  $\mu\text{m}$ ) of the density material (biobook, p. 101)

$$\text{LET} = \frac{dE}{dx} \quad (1.1)$$

To maximise the chances of inducing damages in the DNA and minimizing exposure of healthy tissue, choosing a particle with a high linear energy transfer is important in targeted radionuclide therapy. Figure 1.1 illustrates how  $\beta^-$ -particles, alpha-particles and auger electrons deposit energy on the scale of DNA.

Beta decays occur whenever there is an overweight in number of protons/neutrons.  $\beta^-$ :  $n \rightarrow p + e^- + \bar{\nu}_e$ . The contrary  $\beta^+$  decay:  $p \rightarrow n + e^+ + \nu_e$ . Neutron mass is higher than proton mass with  $2m_e \text{ MeV}/c^2$ , thus energy threshold for beta+ reaction must overcome this. If not high enough E, electron capture happens:  $p + e_{\text{atomic}}^- \rightarrow n + \nu_e$ . For beta is distributed between three particles thus the energy is not discrete. Alpha decay occur when the nucleus is so large about to overcome Coulomb barrier. Thus emission of an alpha particle lowers the binding energy as the alpha particle carries a high B.E. These are discrete. Auger electrons are result from electron capture or internal conversion, which happens when a gamma-ray interacts electromagnetically with atomic electron, and emit with high energy. The vacancy in the atomic shell can lead to a cascade of X-rays and auger electrons with energies in the X-ray range. These energies are discrete, as the X-ray energy is discrete (minus atomic binding energy). From beta and sometimes alpha decay, the daughter nucleus is left in an excited state and decays by gamma-emission (all from special curriculum).

A medium consists of positively charged nuclei and negatively charged electrons. Charged particles have a short range in a medium compared to neutral particles, as the Coulomb force forces the particle to interact continuously along the path either by scattering inelastic with the atomic electrons or scattering elastic with the nuclei. Elastic scattering is the less dominant process, where the energy loss is small, as long as the nuclei in the medium are larger than the incoming particle(Techniques for Nuclear and Particle Physics Experiments, William R. Leo, p. 21). **Inelastic collisions dominates where the atomic electrons are either excited or ionized (which citation???? Instrumentation book?).**

Under the assumption that the collision is elastic, the collision is head-on and the particle has high energy, the maximum energy transfer can be calculated using conservation of momentum and energy

$$Q_{\max} = \frac{4m_e M}{m + M} E \quad (1.2)$$

where  $m_e$  is the mass of an atomic electron,  $M$  is the mass of the incoming charged particle and  $E$  is the kinetic energy of the incoming charged particle<sup>1</sup>. While LET describes the energy transferred per unit length, the stopping power describes the energy loss of a charged particle per unit distance. The collision loss for heavy charged particles (protons and above) at high energies is therefore low. The stopping power for heavy charged particles (protons and up) is described by Bethe-Block. As the particle slows down, the more energy per unit length will be deposited, as the charged particle picks up electrons. This is known as the Bragg peak. most of the energy is deposited near the end stop. The stopping power of heavy charged particles are proportional to the charge of particle and the inverse velocity squared. Therefore, particles with a higher charge will have a higher Bragg-peak and a shorter range in tissue, if energy was the same. This behaviour of heavy charged particles is especially useful in external beam therapy and is utilized to have a very specific dose over tumor as the dose before is low and the dose after bragg peak is zero (instrumentation, p. 27-28).

Electrons can experience energy loss either from collisions, or via the electromagnetic radiation that arises when electrons are losing energy (bremsstrahlung), due to the small mass. However, for energies up to a few MeV, the collision energy loss dominates (Techniques for Nuclear and Particle Physics Experiments, WilliamR. Leo, p. 37). For electrons, the maximum energy transfer per collision is half of the initial energy, which means that electrons lose energy fast via collisions. Electrons scatters rapidly, and changes direction continuously due to the equal mass of the atomic electrons. The energy loss of electrons fluctuates much more than heavy charged particles which is due to much greater energy transfer per collision and to the emission of bremsstrahlung. To absorb major part of the electron's energy, is a few collisions, and results in greater range straggling. (instrumentation p. 42)

Beta-electrons have a continuous spectrum of energies and absorption of beta decay electrons exhibit behaviour which is well approximated to an exponential form (instrumentation p. 42). Low energetic electrons are small in mass to large angle deflection by scattering from nuclei (p. 48).

Photons and neutrons however are neutral particles and are not energy-degraded. Instead neutral particles are attenuated as a function of distance traversed  $x$  and the attenuation coefficient  $\mu$  of the material

$$I = I_0 e^{-\mu x} \quad (1.3)$$

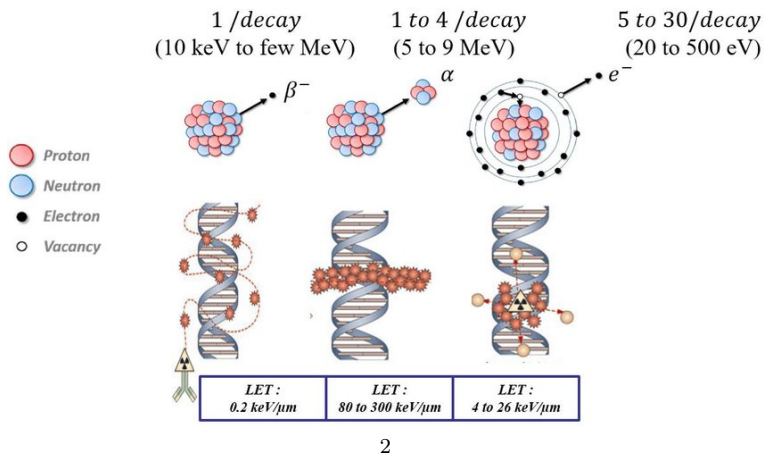
where  $I$  is the intensity as a function of distance and  $I_0$  is the intensity at  $x=0$ . X-rays produced from a X-ray tube and gamma-rays degrades exponentially, thus have a high dose over a long distance. As gamma emitters are not directly used in targeted radionuclide therapy, the gammaradiation following alpha or beta decay, or X-rays following electron capture or internal conversion needs to be taken into account.

For high energetic X-rays, there is also a build up effect, where the photons induce ionizations, and the free electrons contribute to a higher dose. This is utilized in external beam therapy, maximizing the dose over the tumor.

Figure 1.3 illustrates how various particles interact in a medium. For photons, there is an exponential tale, and for high energetic X-rays it is clear that there is a build up effect. For protons, the Bragg peak is very evident. For 22 MeV electrons, it is clear that there is bremsstrahlung energy loss due to the exponential tale.

---

<sup>1</sup><https://ocw.mit.edu/courses/nuclear-engineering/22-55j-principles-of-radiation-interactions-fall-2004/lecture-notes/energydeposhcp.pdf>



3

Figure 1.2: The figure illustrates how  $\beta^-$ -particles,  $\alpha$ -particles and auger electrons deposit their energy on the scale of DNA.

4

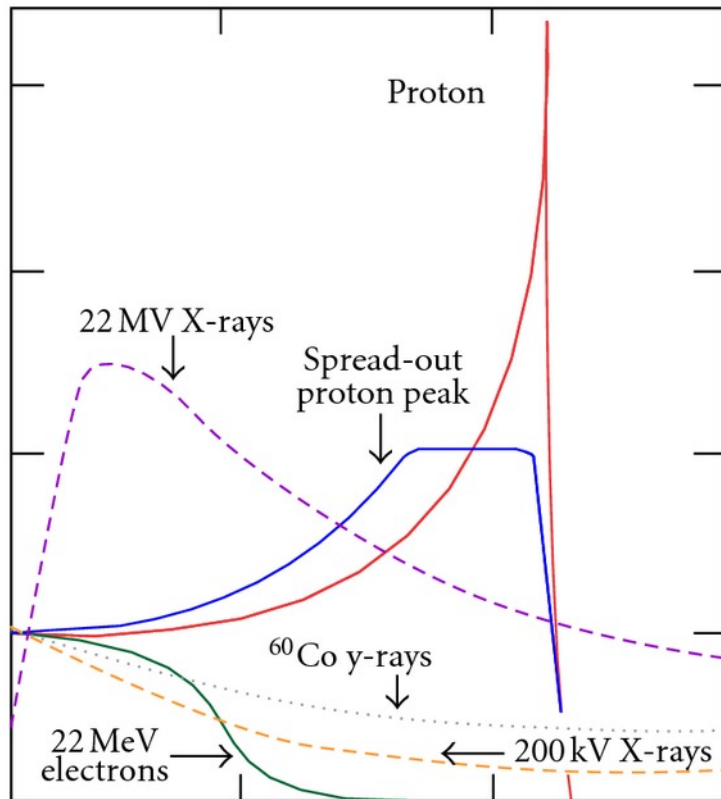


Figure 1.3: Medium depth along x-axis, energy deposition in tissue (or dose?) on y-axis. Find citation in special curriculum.

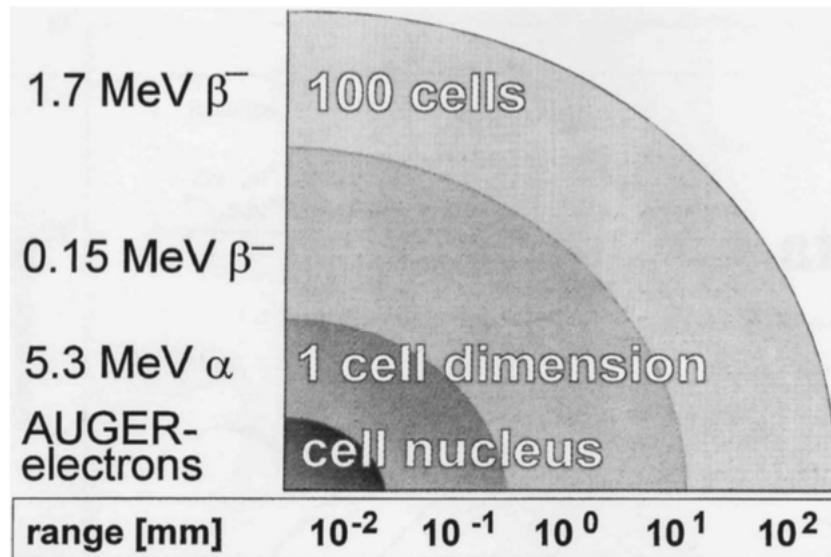


Figure 1.4: The figure illustrates the ranges of auger electrons, 5.3 MeV alpha particles and low and high energetic  $\beta^-$  particles.

Figure 1.4 shows an overview of the ranges of auger electrons, 5.3 MeV alpha particles, low and high energetic  $\beta^-$  particles of 0.15 MeV and 1.7 MeV. Thus  $\beta^-$ -particles have a relatively long range in tissue, and can be up to a few mm dependent on the energy spectrum (handbook, chapter TRNT (TARGETED RADIONUCLIDE THERAPY). Beta-particles have relatively low LET and are thus suited for treating large tumors, but the dose to healthy tissue is hard to avoid. Alpha-particles have short range in tissue, typically a one to a few cells in diameter. Has a high LET-value, radiation with  $\text{LET}=100 \text{ keV}/\mu\text{m}$  has the distance between ionizing events is nearly identical to that between DNA strands increasing the probability of creating highly cytotoxic double strand breaks (handbook, TRNT). One of the major problems with alpha-emitters however is the decay products, as a typical alpha decay chain results in multiple emission of alpha and beta (??). For low energetic electron emitters such as auger emitters, the range is so low that in order to deposit energy in the DNA, must be incorporated into the cellular nucleus. Thus, it will only affect the cell targeted, and as we can see in figure 1.1 when incorporated into DNA, will induce many breaks and kill cell!! (book: chapter targeted radionuclide therapy, whole paragraph)

## 1.2 Production of radionuclides

The radionuclide availability is an important factor, and must obviously be high. Reactors, cyclotrons and natural decay chains have traditionally been used as radionuclide sources (Handbook of ... , p. 2185). Proton rich nuclei are typically produced in accelerators/cyclotrons using positively charged particles, and neutron rich nuclei are typically been products of fission or produced in the neutron flux resulting from fission in a reactor. Thus therapeutic radionuclides producing  $\beta^-$ -emitters needs neutrons, which are the main source of reactors. With research reactors today aging ([3], in special curriculum p. 10), alternative production routes to produce critical medical radionuclides.

There are many different production routes available for a single radionuclide, dependent on choice of target, particle beam and beam energy. The production route has an associated reaction cross section which is dependent on the beam energy. The nuclear cross section data is very important in optimization of production processes, achieving the maximum yield of the desired radionuclide combined with the minimum level of radionuclidic impurities ([9], in special curriculum p. 3). A high degree of radionuclidic purity is required for therapeutic radiopharmaceuticals depending on the nature of the molecule that will be labelled, specific activity (GBq/mmol) may also be important

consideration. It is impossible to chemically separate isotopes of the same element ([4], in special curriculum p. 10). We want to be sure that the what is injected into the patient does not have isotopic impurities which gives undesired dose to the tissue, nor will we have isotopes with no therapeutic effect, both for most effective treatment, but especially in cases where the body does not excrete the element from the body, and we can have poisoning. Carrier-free production which are molecules which exclusively contain the desired radionuclides is desired because it gives the highest specific activity. The only option to minimize impurities is to choose an appropriate energy window which minimizes the production of co-products.

There already exists large amounts of information on neutron induced reactions. However the information on charged particle induced reactions is not as strong so we need more data on this behalf ([4] in special curriculum p. 10). Production of medical radionuclides should be cheap and available for everyday medical purposes. Cyclotrons good: Accelerators can be small in size and handled easily by medical personnel. Many hospitals which performs nuclear medicine even have a cyclotron facility on site, which is advantageous as its practical to avoid travelling logistics and to have medical radionuclide supply in proximity of examination/treatment site.

### 1.3 $^{193}\text{m}\text{Pt}$ as a potential therapautic agent

$^{193m}\text{Pt}$  ( $t_{1/2}=4.33$  days) is an auger-emitting isomer which decays by isomeric transition (100%) to the long-lived  $^{193g}\text{Pt}$  groundstate ( $t_{1/2}=50$  years) [2]. Radionuclides produced from deuterons on natural iridium such as  $^{191}\text{Pt}$ ,  $^{193m}\text{Pt}$ ,  $^{192}\text{Ir}$  and  $^{194}\text{Ir}$  are believed to have potential in medicine, like chemotherapy, brachytherapy, radioimmunotherapy and imaging (Tarkanyi et.al 2006). Platinum radionuclides are of special interest, as platinum is the main element in chemotherapeutic agents such as cisplatin, which is a drug which is used clinically in treatment of testicular and ovarian cancer mainly, but also to treat esophagus, head and neck and bladder cancer<sup>5</sup>. Cisplatin (cis-dichlorodiammine platinum(II)) is an inorganic molecule which contains one stable platinum atom surrounded by two chlorine atoms and two ammonia molecules ( $\text{NH}_3$ ). The cisplatin-molecule enters the cell nucleus, and binds to the DNA, example-wise shown in figure 1.5, where the chlorine-atoms are de-attached and the platinum-atom binds through covalent bonds to the DNA base guanine (and in some cases adenine, **is that correct?**), and breaks the bonds between the DNA nitrogenous bases. Cisplatin thus targets the DNA. One of the major challenges with cisplatin is the chemical toxicity, but when auger-emitters such as  $^{193m}\text{Pt}$  or  $^{195m}\text{Pt}$  replace the stable platinum atom, the local auger-damage effect increases the chemical damage of cisplatin, suggesting that a smaller amount of the drug is required, and chemical toxicity can be avoided. <sup>6</sup>. **exactly how does it target the specific target cells, how is the uptake? how does the uptake of a healthy cell differ from cancer cells?**

By replacing either of the stable nitrogen atoms with the PET-radionuclide  $^{13}\text{N}$  ( $t_{1/2}=9.965$  minutes), or by a radionuclide platinum, where  $^{191}\text{Pt}$  ( $t_{1/2}=2.83$  days, decay by electron capture (100%) to  $^{191}\text{Ir}$  (stable)),  $^{193m}\text{Pt}$  and  $^{195m}\text{Pt}$  ( $t_{1/2}=4.010$  days, decay by isomer transition (100%) to  $^{195g}\text{Pt}$  (stable)) is of special interest, cisplatin can be used for imaging or therapy<sup>7</sup>, but therapy is most common.

As  $^{191}\text{Pt}$  is electron-capture emitter, can be used in imaging, with for instance 129.4 keV (38.0%) or 172.19 keV (43.2%). Combining  $^{191}\text{Pt}$  with a therapautic agent might be possible for theranostic pair with either  $^{193m}\text{Pt}$  or  $^{195m}\text{Pt}$ ? Can be combined with therapy as it releases auger electrons?

Gamma-decay is a result of de-excitation of a nucleus with the release of a photon equal to the energy difference between the two states. The typical half-life of a populated excited state is less than  $10^{-9}$  seconds, and states with longer half-lives are called isomeric states (Krane p. 175). This isomer decays by isomeric transition. In all decays, there are certain quantities which needs to be conserved;

<sup>5</sup>[https://www.sciencedirect.com/science/article/pii/S0969804399000822?casa\\_token=ZLJ8YPQzGZMAAAAAA:264QzKWpH8Kv6iHotiGMeoHTk8jKqmnoDgf709SrAD8BUWVwbRXriZbHgkYOtHg-2qyX3Hvt9E](https://www.sciencedirect.com/science/article/pii/S0969804399000822?casa_token=ZLJ8YPQzGZMAAAAAA:264QzKWpH8Kv6iHotiGMeoHTk8jKqmnoDgf709SrAD8BUWVwbRXriZbHgkYOtHg-2qyX3Hvt9E)

<sup>6</sup><http://citeseerx.ist.psu.edu/viewdoc/download?doi=10.1.1.987.2577&rep=rep1&type=pdf&page=506>, p. 493

<sup>7</sup>[https://www.sciencedirect.com/science/article/pii/S0969804399000822?casa\\_token=ZLJ8YPQzGZMAAAAAA:264QzKWpH8Kv6iHotiGMeoHTk8jKqmnoDgf709SrAD8BUWVwbRXriZbHgkYOtHg-2qyX3Hvt9E](https://www.sciencedirect.com/science/article/pii/S0969804399000822?casa_token=ZLJ8YPQzGZMAAAAAA:264QzKWpH8Kv6iHotiGMeoHTk8jKqmnoDgf709SrAD8BUWVwbRXriZbHgkYOtHg-2qyX3Hvt9E)

angular momentum, parity. Krane says that a multipole of order  $\ell$  transfers angular momentum  $\ell\hbar$  per photon (Krane p.333). A nuclear state has a definite angular momentum  $\ell$  (ang mom + spin?) and parity, and if a gamma transition is to happen between two states the photon must connect the two states by conserving angular momentum and parity. In order for the quantity  $\ell$  to be conserved, the angular momentum can be integers between

$$|I_i - I_f| \leq \ell = I_i + I_f \quad (1.4)$$

where i is initial and f is final. I is the total spin (angular momentum and spin). The parity decides whether the radiation is electric multipole or magnetic multipole (equations from Krane p.311)

$$\pi(ML) = (-1)^{\ell+1}, \quad \pi(EL) = (-1)^\ell \quad (1.5)$$

There are three populated states, the isomer state at 149.8 keV, with nuclear spin  $13/2^+$  (4.33 d), a state at 14.3 keV with nuclear spin  $5/2^-$  (2.52 ns), a state at 1.6 keV with nuclear spin  $3/2^-$  (9.7 ns) and the ground state at 0.0 keV with nuclear spin  $1/2^-$  (50 y)<https://www.nndc.bnl.gov/nudat2/getdecayscheme.js> [2].

For the decay of  $^{193m}\text{Pt}$  (E level=149.8 keV) to the excited state (E level=14.3 keV), the spin and parity changes from  $13/2^+$  to  $5/2^-$ , which gives possible values for  $\ell = 4, 5, 6, 7, 8, 9$ . The electric decays have even parity when  $\ell$ =even, and magnetic has even when  $\ell$ =odd. If parity is unchanged in the decay ( $\Delta\pi=\text{no}$ ), the electric multipoles are even and magnetic multipoles are odd. If the parity does change ( $\Delta\pi=\text{yes}$ ) there would be odd electric and even magnetic multipoles. Hence for the possible transitions between  $13/2^+$  to  $5/2^-$  are whenever  $\Delta\pi=\text{yes}$  and  $\ell = 4, 5, 6, 7, 8, 9$ , which gives possible M4, E5, M6, E7, M8 and E9 transitions.

In general, the lowest possible multipole dominates, and the emission of a multipole of one order higher ( $\ell + 1$  than  $\ell$ ) is reduced by a factor ca.  $10^{-5}$  (Krane, p. 335). Thus a multipole of order 4 or 5 has a low probability of occurring and thus the isomer has a long half-life. In comparison, the decay from  $5/2^-$  to  $3/2^-$  gives possible radiation  $\ell = 1, 2, 3, 4$ ,  $\Delta\pi=\text{no}$ , gives possible M1, E2, M3, E4 and the same for decay from  $3/2^-$  to  $1/2^-$ .

Whenever gamma-decay is possible, another process called internal conversion is competing. It is an electromagnetic process where the nucleus electromagnetically with the atomic electrons, and an atomic electron is emitted instead of the photon (Krane, chapter 10, p. 341). The kinetic energy of the emitted electron is the transition energy minus the electron binding energy

$$T_e = \Delta E - B \quad (1.6)$$

where B is the binding energy. The emitted electron is called a conversion electron, and the energy is comparable to the gamma-ray energy. The conversion electron varies with the atomic orbital (Krane, p.??), and the electrons following internal conversion are in a spectrum of different discrete energies. The transition energy must be higher than the electron binding energy, and as a consequence the electron is labelled with the shell it was emitted from (remember that atomic shells are labelled with n: n=1=K, n=2=L, n=3=M, n=4=N, etc).

For  $^{193m}\text{Pt}$ , internal conversion is highly favoured before gamma-decay, thus the observed gamma in gamma-ray spectroscopy is difficult. The total probability is the summed decay probability for gamma-decay and internal conversion

$$\lambda = \lambda_\gamma + \lambda_{\text{IC}} \quad (1.7)$$

and the internal conversion coefficient  $\alpha$  can be defined as

$$\alpha = \frac{\lambda_{\text{IC}}}{\lambda_\gamma} \quad (1.8)$$

High values for  $\alpha$  indicates high probability of internal conversion relative to the probability of gamma emission but the coefficient diverges towards infinity when  $\lambda_\gamma$  reaches towards zero, which for

instance is when the gamma transition is zero. In general, the coefficient increases  $Z^3$ , which will give a much greater coefficient for heavy nuclei than for lighter nuclei. In addition the coefficient decreases rapidly (ca.  $E^{-2.5}$ ) with increasing transition energy. The multipole order also affects the coefficient, where a higher multipole order indicates a higher value. For higher atomic shells than the K shell ( $n=1$ ) the coefficient decreases like  $n^{-3}$  (Krane chapter 10, p. 346).

From a therapeutic point of view, the most important process is the process which occurs after the release of the conversion electron. There is a vacancy in the shell following the emission of the atomic electron, and an electron from a higher shell or subshell fills this vacancy. Radiative or non-radiative processes can take place after to conserve energy<sup>8</sup>. To conserve energy, an X-ray with the energy equal to the difference between the atomic states can be emitted, or that X-ray can interact electromagnetically with atomic electrons in same subshell, a higher subshell or shell (remember shell:  $n=1,2,\dots$ , subshell: spdf..). Dependent on where the ejected electron originated from, the electrons are called super Coster-Kronig, Coster-Kronig or auger electrons respectively. In practice the vacancy moves up to higher atomic shells and the result is a cascade of electrons and Auger electrons, until the reaction "fades out". Due to the low energies, they need to be located close to the cellular nucleus or incorporated into the DNA to induce damage (Handbook of nuclear chemistry, p. 2203). When incorporated into DNA they are equally almost effective as alphaemitters [3] + handbook p. 2203).

---

<sup>8</sup><https://sci-hub.tw/https://doi.org/10.1118/1.596927>

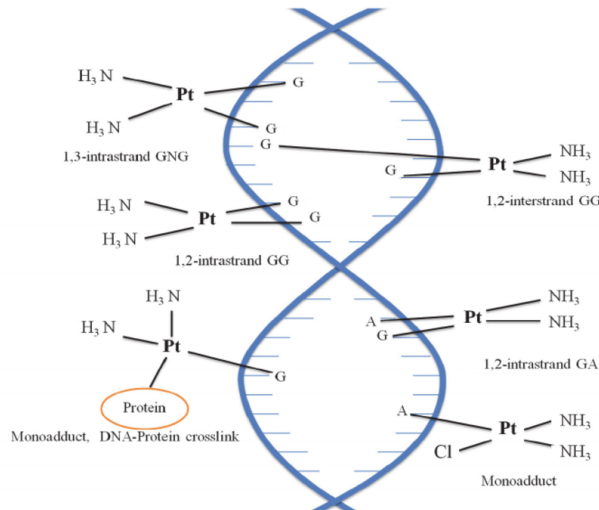


Figure 1.5: A DNA Repair Protein BRCA1 as a Potentially Molecular Target for the Anticancer Platinum Drug Cisplatin - Scientific Figure on ResearchGate. Available from: [https://www.researchgate.net/figure/Common-cisplatin-DNA-adducts-and-functions-For-instance-the-platination-of-human-serum\\_fig2\\_21919257](https://www.researchgate.net/figure/Common-cisplatin-DNA-adducts-and-functions-For-instance-the-platination-of-human-serum_fig2_21919257) [accessed 12 Apr, 2020].

**Energy loss of low E auger electrons.** In this energy region, is due to collision loss, not bremsstrahlung. Deflects frequently due to low mass, and the max energy loss is  $T_e/2$  per collision, as described in equation 1.2.

General stuff <sup>193m</sup>Pt: Cellular nucleus is approximately 6 μm, while thickness of DNA is ca 2 nm (wikipedia). Range of the electrons from the decay is between 3.29nm-231μm, according to simulation done by Howell (1992) [4], so well within cellular nucleus. In its decay, it emits 26.4 coster-konig and auger electrons (energy released per decay: 10.353 keV) and internal 3 conversion electrons (energy released per decay: 126.738 keV). According to the simulation, an additive 12.345 keV is for X-ray energy deposition per decay.

Production: there are multiple ways that this isomer can be produced, either in a neutron field in a reactor, or in a charged particle accelerator like a cyclotron: <sup>192</sup>Pt(n,γ) or via <sup>192</sup>Os(α,3n). One of the issues with production is that <sup>193m</sup>Pt (and <sup>195m</sup>Pt) are difficult to produce with high specific activity [5], and are not well investigated. This study gives an examination of a new route. Many reasons, reactors are on their way out, and Osmium is a poisonous and difficult target to work with, so using iridium as target is easy, (expensive though?) and the production of radionuclides below iridium is evidently in this work and in papers tarkanyi et al (2006,2019) low.

By itself, not useful for imaging. <sup>191</sup>Pt and <sup>195</sup>mPt can. Can replace stable N with <sup>13</sup>N, but the half life is so short that the radionuclide can not image the distribution it self, so not as a theranostics pair?? or does cisplatin distribute so fast within the body?

Pt-poisoning

## Chapter 2

# General nuclear reaction theory

paragraph based on special curriculum need to rewrite this part as some of this is already mentioned above.. Medical radionuclides can be produced directly using charge particle (cyclotron) or neutron beams (reactors), or indirectly using radionuclide generators or fission (reactor). Medical radionuclides are typically produced in reactors, cyclotrons or by a longer lived-parent decaying into a short-lived daughter in a radionuclide generator system. In general, the production should be cheap, available. Today many radionuclides are only produced in reactors, which is the main source of neutrons, and with reactors aging (Chai Hong Yeong, Mu hua Cheng, and Kwan Hoong Ng. Therapeutic radionuclides in nuclear medicine: Current and future prospects. Journal of Zhejiang University: Science B, 15(10):845–863, 2014.), we need alternative routes to produce critical radionuclides. Cyclotrons have many benefits, like size so that it can be produced directly at the site of usage. One of the major disadvantages is that there is a need to enriched targets to get the desired reaction, and those can be very expensive. Along with high beam intensity the melting of the target can give challenges, so target cooling techniqueis need to be there.

In order to create isotopes, nuclear reactions need to occur. There are many different production routes available for a single radionuclide, which is dependent on multiple factors such as choice of target, incident particle-beam and beam energy. To each reaction route, there is an corresponding excitation function which tells us how probable the reaction channel is at various energies. The nuclear reaction data is very important for the optimization of the product, achieving minimal level of isotopic impurities and maximum yield (S M Qaim, R Capote, and F Tarkanyi. Nuclear Data for the Production of Therapeutic Radionuclides. Trs 473, (473):395, 2011., p. 3).

Isotopic purity is important as it is impossible to separate isotopes of the same element [5]. An undesired radionuclidel can lead to undesired dose to healthy tissue, and a non-radioactive nuclide may lead to poisoning (if large amounts injected), but it will not have any therapaetic effect. This is especially important when working with poisoneos elements such as platinum. The only option to minimize isotopic impurities is to choose an appropriate energy window.

Using charged particles instead of neutrons allows for measurement at multiple energies as the particle energy degrades in the foils. The neutron energy is not degraded in the same way, due to electric neutrality, thus can only give cross section at one single energy.

### 2.1 Radioactive decay law

where to place this?

From here based on Krane chapter 6 <sup>1</sup>

The activity of a nucleus is defined as the number of decayed nuclei per unit time of a radioactive product, which is equal to the radioactive decay rate

$$A = \frac{dN}{dt} = -\lambda N \quad (2.1)$$

---

<sup>1</sup><https://faculty.kfupm.edu.sa/phys/aanaqvi/Krane-Ch-6.pdf>

where  $N$  is the number of nuclei,  $t$  is the time and  $\lambda$  is the decay constant. Solving equation 2.1 gives number of decayed products at time  $t$

$$N(t) = N_0 e^{-\lambda t} \quad (2.2)$$

Since  $N \propto A$ , the relations  $\frac{N_0}{A_0} = \frac{N(t)}{A(t)}$  are valid, and we can rewrite the equation 2.2 to

$$A(t) = A_0 e^{-\lambda t} \quad (2.3)$$

This accounts for single nucleus decaying into a daughter product, without anything first decaying into the parent nucleus. However it is common that a radioactive nucleus decays into another radioactive nucleus. Hence the daughter activity will increase due to feeding from the parent. For multiple decay, Bateman equation is used describing the activity in nucleus  $n$  of the decay chain ([Voyles2018, which article??](#))

$$A_n = \lambda_n \sum_{i=1}^n \left[ \left( A_{i,0} \prod_{j=i}^{n-1} \lambda_j \right) \cdot \left( \sum_{j=i}^n \frac{e^{-\lambda_j t}}{\prod_{i \neq j}^n (\lambda_i - \lambda_j)} \right) \right] \quad (2.4)$$

where  $A_n$  is the activity of nuclei  $n$  in the decay chain, with the corresponding decay constant  $\lambda_n$ . The equation sums over all nuclei in the decay chain.  $A_{i,0}$  is the initial activity of nucleus  $i$ , and  $j$  is the nucleus which is feeding into nucleus  $i$ .

If a target of stable nuclei is assumed, which is exposed to a particle beam which induces various nuclear reactions, the constant rate of production of a specific reaction is dependent on the number of target nuclei, the current of flux of the particle beam and the reaction cross section

$$R = N_T \Phi \sigma \quad (2.5)$$

where  $R$  is the production rate,  $N_T$  is the number of target nuclei,  $\Phi$  is the beam current or flux and  $\sigma$  is the reaction cross section. In the assumption of the production rate being a constant value, the number of transformed target nuclei is small in comparison to the total number during the irradiation time. The number of produced nuclei from a specific reaction per unit time is thus the produced nuclei minus the decayed nuclei (activity)

$$dN = R dt - \lambda N dt \quad (2.6)$$

which has the solution

$$N(t) = \frac{R}{\lambda} (1 - e^{-\lambda t}) \quad (2.7)$$

From equation 2.1, the total activity produced during irradiation time  $t$  is thus

$$A(t) = R(1 - e^{-\lambda t}) = N_T \Phi \sigma (1 - e^{-\lambda t}) \quad (2.8)$$

At the end of beam, the activity is denoted as  $A_0$ , and  $t$  is the irradiation time:

$$A_0 = N_T \Phi \sigma (1 - e^{-\lambda \Delta t_{\text{irr}}}) \quad (2.9)$$

When a target is irradiated, the activity of the product nucleus will increase until secular equilibrium is achieved, which is when the product rate and decay rate are constant. Hence it is not necessary to irradiate a target for more than 2-3 half lives.

If a spectrum is counted at a delay time  $\Delta t_d$  after end of beam with a counting time  $\Delta t_c$  the total number of decayed products are

$$N_D = \int_{\Delta t_d}^{\Delta t_d + \Delta t_c} A(t) dt \quad (2.10)$$

Using equation 2.3 for  $A(t)$ , the solution to the above equation is

$$N_D = \frac{A_0}{\lambda} e^{-\lambda \Delta t_d} (1 - e^{-\lambda \Delta t_c}) \quad (2.11)$$

which again is equal to

$$N_D = \frac{A(t)}{\lambda} (1 - e^{-\lambda \Delta t_c}) \quad (2.12)$$

We can only know the number of decayed products which are detected. This is dependent on the efficiency of the detector, the intensity of the gamma-rays and the true number of decayed products

$$N_C = N_D \epsilon I_\gamma \quad (2.13)$$

where  $N_C$  is the number of observed/ counted gamma-rays,  $\epsilon$  is the efficiency of the detector and  $I_\gamma$  is the gamma-ray intensity.

Thus, we can obtain an expression for  $A(t)$  after a delay time:

$$A(t) = \frac{N_C \lambda}{\epsilon I_\gamma (1 - e^{-\lambda \Delta t_c})} \quad (2.14)$$

Again using 2.3 for  $A(t)$ , the above expression can be rewritten using  $A_0$  and the delay time  $\Delta t_d$

$$A_0 = \frac{N_C \lambda}{\epsilon I_\gamma (1 - e^{-\lambda \Delta t_c}) e^{-\lambda \Delta t_d}} \quad (2.15)$$

## 2.2 Nuclear reactions and reaction cross sections

A nuclear reaction occurs when a collision between two nuclei or a nucleus and a subatomic particle takes place. Collision between an accelerated subatomic particle or small nucleus and target nuclei is common in isotope production. A nuclear reaction is denoted as

$$X(a, b)Y \quad (2.16)$$

where X is the target, a is the incoming projectile, b is the outgoing decay channel and Y is the product of the nuclear reaction (Krane, chapter 11.1). There are multiple processes which can occur, radiative capture is the process where a particle is captured and a  $\gamma$ -ray is emitted in a  $(x, \gamma)$  process. If the incoming and outgoing particle is the same, it is a scattering process, where elastic scattering leaves the target nucleus in the energy same state, and inelastic if the target nucleus is in an excited state. In these type of experiments however, we are interested in emission of particles to create products in which we can measure the reaction cross section.

In a nuclear reaction, the total energy and linear momentum, proton and neutron number, angular momentum and parity are conserved quantities (assuming no meson formation) (Krane, p.380). In the low energy-region in which isotope production typically takes place ( $\text{180 MeV?}$ ), compound nucleus reactions take place, where an incoming particle and target nucleus merges by sharing the kinetic energy on all nucleons, and particle emission takes place to reduce the excess energy. <sup>2</sup>Involves nucleon nucleon interactions, lead to a complete thermal equilibrium inside the CN. Releases energy by emission of neutrons, protons, alpha particles and gamma rays. A consequence of equilibrium is that the decay of CN should not depend on the way it was formed. "forgets" in all the collisions. Consequently, the decay of the compound nucleus depends only on the mass and atomic numbers, excitation energy and angular momentum. The contrary are direct reactions, where an incoming particle interacts (over such a short time period) so that the incoming particle only interacts with one single nucleon, typically on the surface of the target nucleus (thus probably in high nucleon shells, with high spin). Angular distributions of direct reaction products are sensitive to the momentum transfer and

<sup>2</sup>blue text:<https://web-docs.gsi.de/wolle/TELEKOLLEG/KERN/LECTURE/Fraser/L24.pdf>

parity change during the reactions. Thus based on the selection rules from angular momentum and parity conversion the angular distribution measurements in direct reactions yield spin and parities of states populated in the exit channel. Write about feeding to the compound peak???. So in general; emission of protons and neutrons are more fed, because the probability of emitting one single nucleons is easier for the system. Since the reaction forgets the incoming projectile, and interacts with the whole nucleus, the prob of emission of t,  $^3\text{He}$  and d is lower, and the binding energy does not do that the channel is more fed, its only a lower Energy threshold. For alpha particles however, the binding energy which is about 28 MeV lowers the energy quite a lot, therefor favourable if Coulomb barrier is low enough?

The cross section for a reaction can be divided into the cross section of the formation of the compound nucleus via interaction with the incoming projectile a, and the probability that the compound nucleus decay by decay channel b. The total reaction cross section is thus the sum of all the different reaction channels (Handbook of nuclear chemistry, p. 157 (nuclear reactions)),

$$\sigma = \sum_b \sigma(a, b) \quad (2.17)$$

where b can be multiple particles. The general equation which is used to calculate cross sections in this experiment (solving equation 2.15) is the following equation

$$\sigma(E) = \frac{A_0 \cdot t_{\text{irr}}}{N_T \cdot \Phi(E)(1 - e^{-\lambda t_{\text{irr}}})} \quad (2.18)$$

where  $A_0$  is the end of beam activity of the resulting product nucleus (Y),  $t_{\text{irr}}$  is the irradiation time,  $N_T$  is the number of target nuclei (X),  $\Phi(E)$  is the projectile flux or current (a), and  $\lambda$  is the decay constant of the product nucleus.

The compound nucleus model (Bohr, 1936) is a model which describes the formation of a compound nucleus by absorption of an incoming projectile by a nucleus close enough to interact with the strong nuclear force, and the decay of the compound nucleus. The kinetic energy shared between the incoming projectile and the nucleon which was struck leads to multiple collisions with other nucleons and rapid exchange of energy. The energy is distributed throughout the nucleus, leaving the original nucleus in an highly excited state. The average energy per nucleon is not sufficient to overcome the binding energy of the nucleus, but due to the statistical distribution in energies there is a probability that one or more nucleons may get sufficient energy to escape the nuclear potential (Krane, chapter 11.10, p. 416). This is decay of the compound nucleus, and this will lower the excitation energy. We can include the formation of the compound nucleus in the nuclear reaction as



where  $C^*$  is the excited compound nucleus (Krane, chapter 11.10, p. 416)

For each possible decay channel of the compound nucleus, there is an associated probability or cross section, which is dependent on the energy of the incoming projectile. A function which evaluates the various cross sections at different energies is called an excitation function. In figure 2.1, the excitation function of the reactions channels for the platinum isotopes  $^{188,189,191,193m}\text{Pt}$  resulting from deuterons on natural iridium is plotted (using TENDL nuclear reaction code [cite](#)). Natural iridium consists of two stable isotopes,  $^{191}\text{Ir}$  (37.3% abundance) and  $^{193}\text{Ir}$  (62.7% abundance).  $^{193m}\text{Pt}$  can only be produced from  $^{193}\text{Ir}$ , ejecting 2 neutrons in the process, which can be denoted as  $^{193}\text{Ir}(d,2n)^{193m}\text{Pt}$  ( $^{193}\text{Pt}$  is the compound nucleus formation of deuteron on  $^{191}\text{Ir}$ , which has a low production cross section). The other platinum isotopes can be produced as  $^{191}\text{Ir}(d,2n)^{191}\text{Pt}$  or  $^{193}\text{Ir}(d,4n)^{191}\text{Pt}$ ,  $^{191}\text{Ir}(d,4n)^{189}\text{Pt}$  or  $^{193}\text{Ir}(d,6n)^{189}\text{Pt}$  and  $^{191}\text{Ir}(d,5n)^{188}\text{Pt}$  or  $^{193}\text{Ir}(d,7n)^{188}\text{Pt}$ . For each reaction route possible, there is a resulting compound peak, hence,  $^{193m}\text{Pt}$  has only one peak, and the other platinum isotopes has two. The desired particle emission is energy dependent, and the higher energy provided to the compound nucleus, the probability that more particles will be emitted is higher (Krane, chapter 11.10, p.

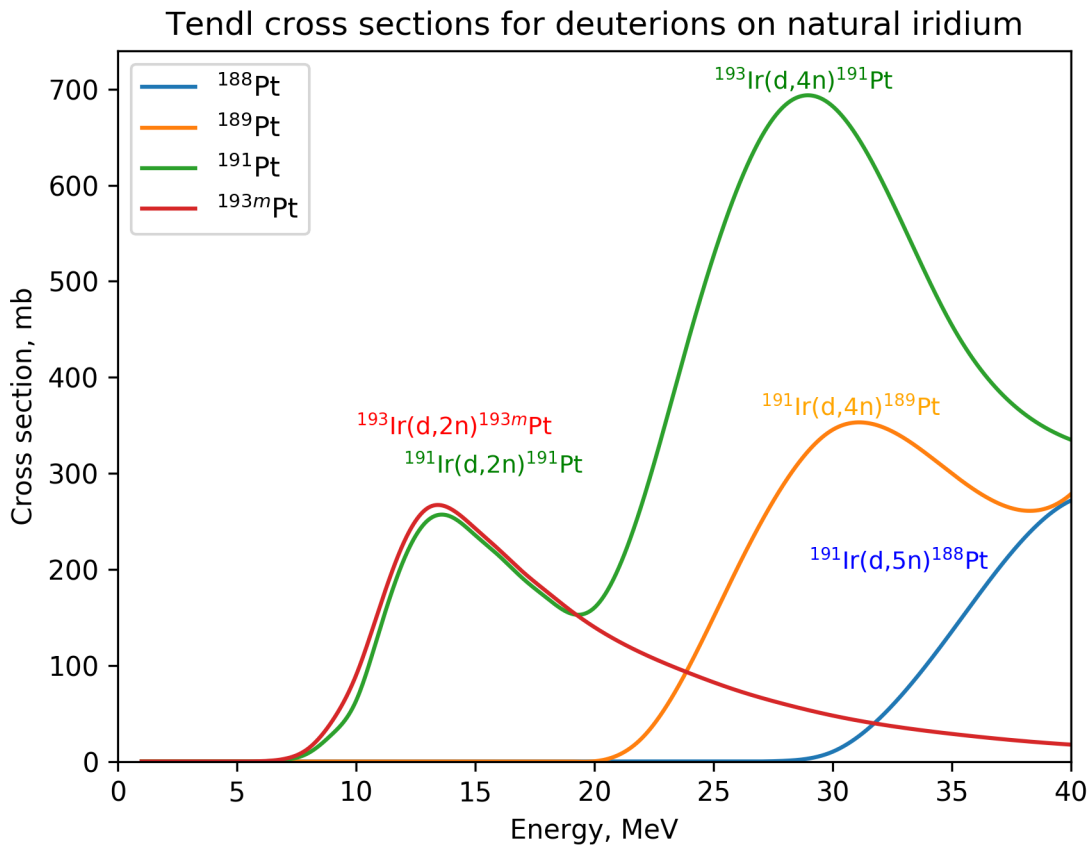


Figure 2.1: Reaction cross sections provided by Tendl for the reactions  ${}^{nat}\text{Ir}(d,x){}^{188,189,191,193m}\text{Pt}$

419). When a specific isotope is desired, the excitation function can tell us which energy window that maximizes the production and most importantly minimizes particularly other isotopes of the same element, due to the difficulty of separating same chemical elements.

### 2.2.1 Constraints in nuclear reactions

The potential energy of a nucleus is the sum of the attractive well from the strong nuclear force and the repulsive Coulomb barrier which acts repulsive between charged particles and the nucleus, acting long range (p. 152, Handbook of nuclear chemistry). The radius of the potential well is up to a few femtometer. For a positively charged particle induced nuclear reaction, the energy of the particle should exceed the barrier, or there will be an elastic scatter. However, there is a chance of tunneling, which drops with a factor  $1/r$  where  $r$  is the distance from the center of the nucleus (Handbook of Nuclear Chemistry, chapter 3 - Nuclear Reactions, section, 3.2.3). The barrier also constraints the emission of particles for a decay channel of the compound nucleus, as the energy for an outgoing decay channel of positive particles must exceed the barrier.

The height of the Coulomb barrier is dependent on the radius and charge of the incoming or outgoing particle a and the target nucleus b.

$$U_{\text{Coulomb}} = \frac{1}{4\pi\epsilon_0} \frac{e^2 Z_a Z_b}{r_a + r_b} \quad (2.20)$$

In addition, there is a centrifugal barrier, which can constraint some of the incoming particle energy in rotational energy, **which depends on the angular momentum of the incoming particle and the nucleus???** (handbook of nuclear chemistry p. 155.)

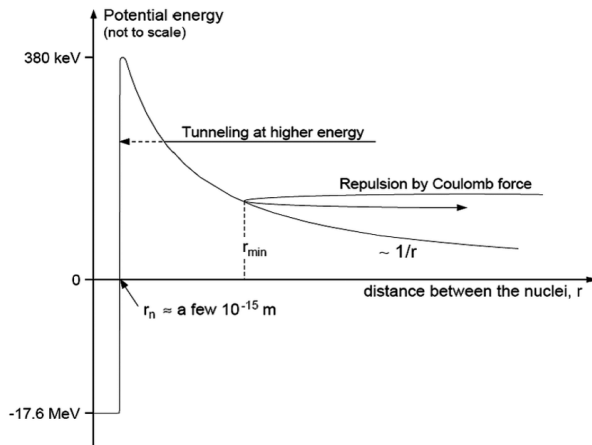


Figure 2.2

$$U_{\text{centrifugal}} = \frac{\hbar\ell(\ell + 1)}{r^2} \quad (2.21)$$

The sum of the barriers are the total barrier but the Coulomb barrier is the most important. In a nuclear reaction, the mass-energy is conserved, which is denoted as the Q-value. The reaction Q-value is the difference in masses between before and after the nuclear reaction occurred (Krane, chapter 11.2). It is defined as

$$Q = (m_i - m_f)c^2 = (m_X + m_a - m_Y - m_b)c^2 \quad (2.22)$$

where  $m_i$  is the initial mass,  $m_f$  is the final mass and  $c$  is the speed of light. If  $Q > 0$ , then the reaction is exoergic, which means that energy is released in the reaction. There is no threshold energy of the projectile required for the reaction to occur, if only the projectile is present the reaction can occur. If  $Q < 0$ , then the reaction is endoergic, which means that the kinetic energy of the incoming projectile is converted into nuclear mass or binding energy. For endoergic reactions to occur, there is a minimum threshold energy of the projectile in order for the reaction to happen, which is defined as (Krane, 11.2, p. 382)

$$E_{\text{threshold}} = (-Q) \cdot \frac{m_Y + m_b}{m_Y + m_b - m_a} \quad (2.23)$$

The energy threshold thus depend on the Q-value, the Coulomb barrier for charged particles, and the centrifugal barrier if angular momentum  $\ell \neq 0$ . The parity though depend, even numbers of  $\ell$  mix with even, and odd with odd (Handbook of Nuclear Chemistry, chapter 3Nuclear Reactions, section, 3.2.3). This gives an indication on when a reaction can energetically occur, but does not tell us how probable the reaction is.

The binding energy is the mass-difference between the nucleus as a whole, and the number of protons and neutrons added

$$B = c^2(z \cdot m_p + n \cdot m_n - m_N) \quad (2.24)$$

where  $z$  is the number of protons,  $n$  is the number of neutrons,  $m_p$  is the proton mass,  $m_n$  is the neutron mass,  $M_N$  is the mass of the nuclide, which is the number of nucleons A minus the number of electrons,  $M_P = m_A - z \cdot m_e$  (the electronic binding energy per electron is excluded). From Krane's derivation of the nuclear binding energy (Krane, chapter 3.3, p. 65).

From equation 2.22, the larger the mass of the outgoing decay channel, the more negative the Q-value will be. Protons (+1 charge) and neutrons (neutral) are the simplest decay channels of the compound nucleus, each carry a spin of 1/2, with masses  $m_p = 938.28 \text{ MeV}/c^2$ , and  $m_n = 939.57 \text{ MeV}/c^2$ . Combinations like deuterons ( $d=1p+1n$ , charge +1) has a mass difference of  $\Delta = 2.2 \text{ MeV}/c^2$  from realising 1 proton and 1 neutron separately, a triton ( $t=2n+1p$ , charge +1) with  $\Delta = 8.5 \text{ MeV}/c^2$ , 3-Helium ( ${}^3\text{He}=1n+2p$ , charge +2) with  $\Delta = 7.7 \text{ MeV}/c^2$  and alpha-particle ( $\alpha=2n+2p$ , charge +2)

with  $\Delta = 28.3 \text{ MeV}/c^2$ . Thus, Q-values are higher in value, the lighter the particle is. However, in this work, we can clearly see that protons, neutrons and alpha-particles are strongly fed decay channels, while the other don't even appear. The suggested reason for this is that due to **blablabla nuclear physics stuff, like shell structure**, protons and neutrons are favoured, but since the alpha-particle has such a large binding energy, this channel is also favoured.

### 2.2.2 Deuterons and stopping power

The deuteron consists of a neutron and a proton, and is the simplest bound state of nucleons. Nucleons have an average binding energy per nucleon of 8 MeV. The deuteron with an observed mass value of 2.224 MeV (Krane, p. 81) is a weakly bound. Thus little energy required to break up the deuteron. **does this affect?**

The stopping power of a deuteron beam running through forms the Anderson & Ziegler. **write about Anderson and Ziegler. And how does the stopping power give a flux??**

(Technique nuclear and particle physics p. 30-31): For a particle beam the energy loss is not a continuous process, but collisions based on statistics. A measurement of identical particles will thus show a statistical distribution of ranges centered about the same mean value. This is called range straggling **this part relevant for describing Ziegler flux?**.

Energy straggling: the energy loss distribution: (instrumentation p. 49) "For any given particle however, the energy lost will not be equal to this mean value because of statistical fluctuations which occur in the number of collisions suffered and in the energy transferred in each collision. An initially monoenergetic beam will therefore show a distribution of energy rather than a delta function peak shifted down by the mean energy loss given by the  $dE/dx$  formula after passing through a fixed thickness of material.. see if more necessary?"

## 2.3 Nuclear reaction models

The optical model (proton/neutron, and alpha/deuteron), gamma strength function.

**EMPIRE 3.2.3**

**CoH 3.5.3**

**ALICE 2017**

**TALYS 1.9**

**TENDL 2019**

## 2.4 Detection and identification of radionuclides

Gamma-ray spectroscopy is a method to identify and obtain information about radioactive nuclei present in a detector. As beta and alpha decay can result in an excited daughter product, the spectrum in fact shows the de-excitation of the daughter product. Since we know that these gamma-lines are transitions which happens right after a beta or alpha decay (or isomer transition), we identify the parent with gamma-ray spectroscopy. A detector has channels in which counts are registered. These channels are ... similar to the gamma-ray energy. Thus a spectrum has channels (which increases in energy) along the x-axis and counts along the y-axis. If a detector registers many counts, it means that the state is highly populated, and the intensity of the gamma is strong (Krane, p. 351).

### 2.4.1 High purity Germanium detector

High purity Germanium detector is a type of semiconductor, which is a material where the energy required to remove an electron from the valence band (in the outer atomic shell) to the conduction band is small. The germanium atom has atomic number 32, and 4 valence electrons in the outer p4 shell (need citation?). The atoms in the detector are bound through covalent bonds in a crystal

structure. The main mechanism of a semiconductor is creation of electron-hole pairs after energy deposition of an ionizing particle in the crystal. If an electron is excited to the conduction band, a hole is left. This hole can move as a neighboring electron fills this spot, and it can cause a chain reaction, and the hole will move in the crystal. Both the electron in the conduction band and the hole in the valence band contributes to an electric current. Under influence of an electric field, the electron-hole pairs will be collected and we can measure the incident as a count. The major advantage with semiconductor detector is that the average energy to create an electron-hole pair is very low, which results in a superior energy resolution in comparison to other detectors like gas and scintillation detectors. High energy resolution advantageous in gamma-ray spectroscopy which makes it possible to separate gamma-ray peaks within less than a keV. At room temperature, thermal energy can excite the electron from the valence to the conduction band and cause noise in spectra. Therefore, Germanium detectors are operated at 0 Kelvin. Write about recombination and trapping, noise, np semiconductor junction, depletion depth?? (Techniques for Nuclear and Particle Physics Experiments, William R. Leo, p. 215-216).

Ideally, for all gamma-rays with the same energy, should be detected in the same channel giving a step function. However, realistically, the resolution of a detector is not that good, and instead of seeing a delta peak, the peak is typically gaussian shape with a finite width. The full width half maximum  $\Delta E$  of the peak tells us how well the relative resolution at gamma-energy  $E$ ,

$$\text{resolution} = \frac{\Delta E}{E} \quad (2.25)$$

The energy resolution is important, as it tells us how well it can distinguish two close lying peaks from each other (Techniques of Nuclear and particle Physics.. , p. 117). The resolution of a germanium detector very good (0.1% for a 1 MeV gamma-ray) in comparison to for instance NaI detector (8-9% for a 1 MeV gamma-ray) (Techniques of Nuclear and particle Physics.. , p. 117). **explain why, prob in semiconductor chapter!**

The peak itself is not directly gaussian. Ionizing radiation statistics is based upon Poisson statistics, where the probability of observing  $N$  events is a discrete value

$$P(N) = \frac{\mu^N e^{-\mu}}{N!} \quad (2.26)$$

where  $\mu$  is the mean value. This distribution counts when the probability is small (eg decay prob?) value and that the total number of trials are large (number of decays) (Techniques of Nuclear and particle Physics.. , p. 85). For poisson distribution, the average is equal to the variance;  $\sigma^2 = \mu$ . From there, the standard deviation ( $\sigma$ ) is thus equal to the square root of the average.

The distribution is not symmetric, but as  $\mu$  increases in value, the peak approxes a gaussian shape. The total number of counts is the area of the peak. The total peak is a Gaussian assumption but with an exponential skew towards low  $E$  caused by incomplete charge collection, abd a step function for taking compton background into account.

In calculation of the peak area, there are two uncertainties of relevance, the relative statistical uncertainty in the counting from the Poisson statistics,

$$\sigma N_i = \sqrt{N_i} \quad (2.27)$$

If number of counts  $N_i = 10000$ , the relative uncertainty ( $\frac{\sigma N_i}{N_i} = \frac{1}{\sqrt{N_i}} = 1\%$ ). Therefore we say that a good number of counts is 10000 or more to reduce the statistical uncertainty. The other is systematic in the detector, and can for instance be due to a process called annealing, which is heat damage to the detector. Can fix by taking a blanket of resistor wrap crystal in, rise to high temp, let it sit and slowly deheat to room temp, traps will diffuse and detector is repaired (this is notes from Andrew).

Also write about deadtime!

### 2.4.2 Gamma-ray spectrum

Spectrum: consists of photopeaks, a compton continuum, compton edge, backscatter peak, single escape double escape. In cases where positrons exist, chances of having a broad fat 511 keV peak.

Germanium detectors, highest resolution for gamma-rays, from few keV to 10 MeV. The peak to Compton ratio is much greater due to the higher photoelectric cross section of Germanium. The largest challenges are with signal to noise ratio, it is important to shield very well to minimize background radiation (Techniques for Nuclear and particle.... William R. Leo, p. 241).

here from another citation: "Practical Gamma-ray Spectroscopy". Gordon R. Gilmore. Nuclear Training Services Ltd Warrington UK. (can be found under articles in masterthesis). This book can also be used in particle interaction in matter check!! In a detector, the particles interact as the photons described in particle interaction, via photoelectric, compton scattering and pair production. Photoelectric absorption where the photon is completely absorbed by atomic electron is desired because all of the energy is deposited within the detector. For a compton scattering event, if the resulting photon's energy is also deposited in the detector (for a large detector), then the total energy would add up. Same for pair production. The photon must interact in the detector volume, and the resulting electron and positron energy is deposited in the detector volume. However when the positron slows down, it annihilates with one atomic electron, releasing two 511 keV photons. If both annihilation photons's energy is deposited in the detector volume this will also contribute to a full width peak. If one 511 photon escapes and the other is deposited, there will be a peak at  $E_\gamma - 511$  keV, and if both peaks escape, there will be a double escape peak at  $E_\gamma - 1022$  keV. The "degree of incomplete absorption" depends upon the size of the detector and the gamma-ray energy. As previously discussed photoelectric effect dominates at low energies, and the less compton scattering and of course pair production (for E gamma higher than the threshold.). The detector size also matters because the larger the more room for the photon to scatter in and lose energy before escaping. (p. 32)

The total spectrum can be seen on p. 33 in the book. Pile-up is done because of random summing, determined by the statistical probability of two gamma-rays being detected at the same time and therefore on the sample count rate.

Interaction with detector shielding: Photoelectric effect can be followed by emission of characteristic X-ray of the absorbing medium. X ray can escape the shielding and be detected by the detector. Compton scattering: most gamma rays are scattered through a large angle by the shielding, BACKSCATTERED. Whatever the initial energy was (if scattered by more than 120 degrees) are within 200-300 keV. Peak appears as broad. Pair production: annihilation peak (511 peak) caused by the escape of one of the 511 keV photons from the shielding following annihilation of the pair production positron. Analogous to the single and double escape mechanisms within the detector but only on 511 keV photons can ever be detected since they are emitted in the opposite direction. So in order to have a 511 peak, energy of gamma ray must be more than 1022 keV. (p. 34-35).

The 511 peak can also be expected when positron emitters are present since beta + particle interacts with electron.

Since Compton scattering can be in a spectrum of energies, it gives rise to a Compton continuum, before the gamma-ray escapes the detector.

The shape of the peak: The peak is a histogram that approximates a Gauss curve (p. 186). Peak searching (SAMPO) using first and second order derivatives to search for peaks (p.185) Due to incomplete charge collection (that electrons or holes are not collected) no matter how caused moves counts from the centre of the Gaussian distribution to lower channels, creating a low energy tail to the peak (p.135).

**Include a picture of peak shape and gamma-ray spectrum!! from the same book**



# Chapter 3

## Experimental setup

The thin foil stacked-target technique was applied to measure the experimental cross sections for reactions induced in iridium, iron, nickel and copper with deuteron energies ranging from ca. 33-5 MeV. This method is well-described in literature<sup>12</sup> for protons. This is however the first experiment using deuterons and the results may differ as for instance the deuteron break up effect is unknown.

### 3.1 Lawrence Berkeley National Laboratory's 88" Cyclotron

Lawrence Berkeley National Laboratory (LBNL) is a national research laboratory on behalf of the U.S. Department of Energy through its Office of Science, and is operated by University of California, Berkeley. LBNL was founded by Ernest Orlando Lawrence, the inventor of the cyclotron<sup>3</sup>.

The 88" Cyclotron has many purposes, and can accelerate both light and heavy ions up to Uranium, with a cyclotron number K=140<sup>4</sup>.

There are multiple programs that takes place in the facility<sup>5</sup>; chip testing and space effects testing, super heavy element searches, fundamental nuclear structure measurements, novel scintillation characterization, fission yield and neutron inelastic scattering measurements (GENESIS) (from Andrew).

A cyclotron is a device that accelerates positively charged particles. It is operated by an alternating electric field, and a perpendicular magnetic field, which by the Lorentz Force forces the particle to accelerate in an outward spiral. The facility is figured in figure 3.1, which consists of a cyclotron vault, and experimental caves in which the beam can be bent to with bending magnets. Faraday cups (not in figure) can measure the beam current at different steps along the tube, which makes it possible to measure the transition efficiency of the beam. Faraday cups are dense metal block, usually 6-7 cm broad Copper and Tantilum. It works as a beam stopper, and can be lowered into the beam line to measure the current. It is electrically isolated, which makes it possible to measure the current, since we know the number of initial particles accelerated. Due to electrons close to surface might be scattered off, it can read off higher positive charge than what is correct. Therefor, a magnet surrounds the cup to bend the electrons back to the Faraday cup in what is called magnetic suppression. Cave 0 is used mainly for neutron beam, chemistry, and isotope production, and was used for irradiation of the target stack.

### 3.2 The experiment

The main motivation of this experiment was to measure production cross sections of the products produced after irradiation of a stack of thin iridium foils along with thin monitor foils Nickel, Copper

---

<sup>1</sup><https://sci-hub.tw/https://doi.org/10.1016/j.nimb.2016.09.018>

<sup>2</sup>Niobium paper and iron paper from Andrew

<sup>3</sup><https://www.lbl.gov/about/>

<sup>4</sup><http://cyclotron.lbl.gov/home>

<sup>5</sup><https://ieeexplore.ieee.org/abstract/document/7999622/authorsauthors>

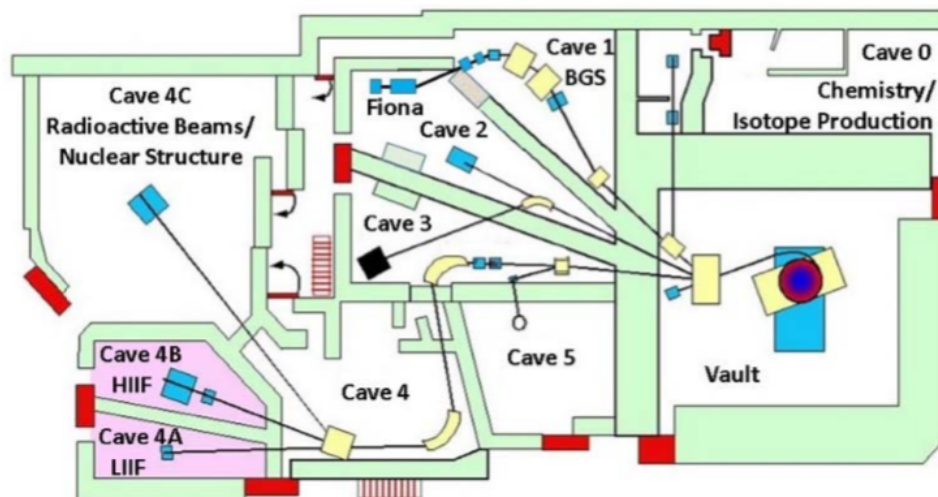


Figure 3.1: An overview of the 88" Cyclotron facility.

<https://cpb-us-e1.wpmucdn.com/sites.usc.edu/dist/7/89/files/2018/04/133-18q03um.pdf>

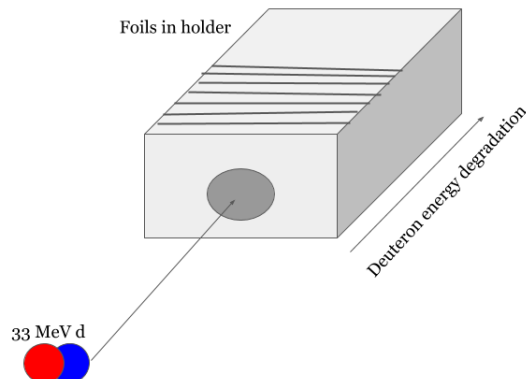


Figure 3.2: The fundamental idea of the experiment where a stack of targets are placed in a target holder, and irradiated with accelerated 33 MeV deuterons. As the energy degrades through the beam stack, it is possible to have multiple cross section measurements at different energies.

and Iron foils, with a 33 MeV incident deuteron beam, as shown in figure 3.2.

The beam was ca. 1 cm in diameter, and with each target foil being ca. 25 by 25 mm, the beam was underfilled. As the energy was degraded through the stack, multiple cross sections at different energies were possible to measure for the different induced reactions. For production cross section data experiments, thin targets (foils) are used, in the other of a few  $\mu\text{m}$ <sup>6</sup> are used, since the induced activity is low, meaning that the deadtime of the detector and the dose to human will be low.

Equation ?? is the equation which is used in the calculation of the cross sections. In order to calculate the cross section of a product, end of beam activity, number of target nuclei and beam current must be found, where for the end of beam activity, the detector efficiency need to be estimated. The number of target nuclei was estimated through characterization of the foils.  $A_0$  was estimated using equation 2.15, which depends on the efficiency calibration of the detectors as a function of gamma-ray energy, the number of counts registered and the intensity of the gamma-rays emitted by the source, the decay constant of the source and the delay time. Some of the nickel, copper and iron deuteron-induced cross

<sup>6</sup>(Syed M. Qaim. Nuclear data for production and medical application of radionuclides: Present status and future needs. Nuclear Medicine and Biology, 44:31–49, jan 2017.)

section are well-established, and can be used to determine the beam current throughout the stack.

### 3.2.1 Target design and foil characterization

**why was the order what it was??** In this experiment, the target stack was composed of ten natural iridium foils (99.9%) foils, along with ten natural nickel foils (..%), ten natural copper foils (..%) and three natural iron foils (..%) (from Goodfellow Corporation, Corapolis, PA 15108, USA) serving as monitor foils. Along with two stainless steel foils in the front and the back of the stack, a proton degrader (a 6061 aluminum alloy), and an extra nickel neutron monitor foil was used to obtain production cross sections at multiple energies, using one incident deuteron beam. The full order of the stack and the characterization of each foil can be seen in table 3.1.

Each foil were cut into approximately 25 by 25 mm squares, and each foil was characterized using a caliper (Mitutoyo Absolute Digimatic) to measure the length across each side, a gauge caliper (Mitutoyo IP65 Coolant Proof) to measure the thickness and an analytical balance weight (Mettler Toledo) to measure the mass of each foil which was prewashed with isopropanol. For each measurement, the unit was measured 4 times, and the values listed in table 3.1 are averaged values. The length and mass were used to measure the mass density. The thickness was not used in the calculation of the mass density, but was a good indication that the foil thicknesses were consistent. **For underfilled beams, the mass density of the foil is used to find the number of nuclei per cm<sup>2</sup>, by using the area of each foil.** The mass density was calculated using the mass of each foil divided by the area

$$\rho\Delta r = \frac{m}{A} \quad (3.1)$$

The uncertainty in each parameter was calculated using the standard deviation (equation A.2) of the four measurements per unit, and the total uncertainty was calculated using the approximation of uncorrelated variables used in equation A.13. The conversion from mg per cm<sup>2</sup> to nuclei per cm<sup>2</sup> was done numerically, by multiplying the mass density with Avogadro's number  $N_A$  and dividing by the mol-mass of the target atoms.

After the characterization, each foil was mounted on a plastic frame with an open space in the middle and attached with capton tape along the edges (from previous experiments, capton tape have shown to be a large **proton?** degrader, so it was important that the tape was not in the beamline **Article by Andrew**). The target frames can be seen in figure 3.3.

### 3.2.2 Irradiation of target stack

The irradiation included tuning of the beam and one hour of radiation over the target stack. Whenever the beam was turned on, the beam tube had to be pumped down to a vacuum, to not attenuate the beam. The target holder was a 6061 aluminum alloy with a hole in the front for the beam. The targetholder was placed in the end of the beam tube (**mounts of the end of an electrically-isolated beamline, (iron paper andrew)**). The targetholder can be visualized in figure 3.4, with a spring holding the foils stable (??a) and placed in the end of the beam tube (??b).

#### Tuning the beam

The cyclotron was tuned for a 33 MeV deuteron beam, and needed to have the correct beam spot. First, the beam spot was visualized using a ca. 2.5 cm thick borosilicate glass, painted with a mixture of phosphor powder and vacuum grease (so that the paint does not evaporate as the tube was pumped down to vacuum). When ionizing radiation strikes the phosphor, the phosphor is excited and emits light in the de-excitation, called phosphorescence. The glass is placed on the end of the beam tube. With a camera placed in cave 0, from the control room, the beam spot could be visualized, and could be steered to be centered and ca. 1 cm in diameter. Secondly, visualization of the beam throughout the beam stack was important to see that the beam did not diverge converge/diverge or move in the wrong direction over the target stack. Gafchromic films which change color if struck by ionizing

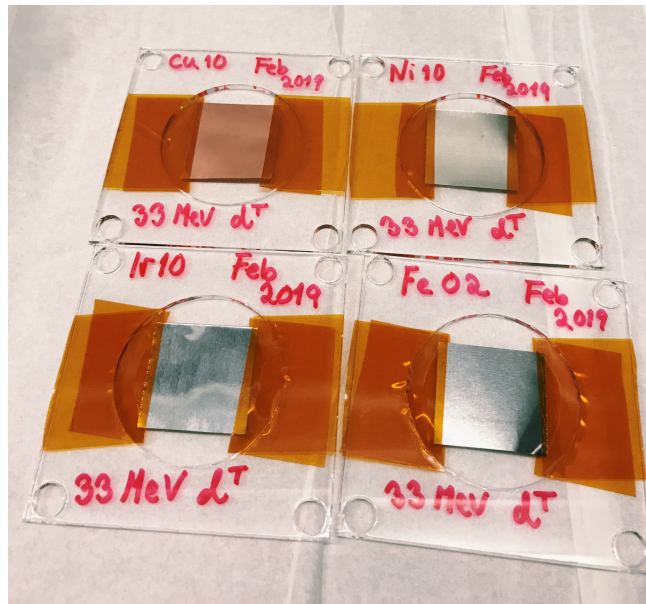


Figure 3.3: The figure shows the four different targets mounted on plastic frames with capton tape attached along the edges of the foils.

radiation was placed in the front and the back of the target holder, separated by the spring. The films were exposed for a brief second, and the blue spot was evaluated. This was done until the beamspot was good both in the front and in the back of the stack.

The beam efficiency transmission was calculated by measuring the current at the Faraday cup right after the cyclotron vault (BS-02) and right before cave 0 (FC-01). BS-02 was measured to be 420 nA and FC-01 was measured to be 285 nA. This gave beam efficiency of transmission

$$\frac{FC - 01}{BS - 02} = 67\%$$

### Irradiation of the target stack

The targetstack was irradiated for exactly an hour, and the current was read of the beam integrator evenly, to assure that the it increased constantly. The beamcurrent from the beam integrator read 128.5 nA. Right after end of beam, the targets were sealed in plastic bags to avoid contamination. The foils were counted at the seven different detectors for the following 4 weeks after end of beam, first short counts to get as many observations as possible of the short-lived activities and longer and longer counts as the times since end of beam passes, so that the counting statistics for the longer lived activites are good.

### Intensity profile of the beam

After irradiation, gafchromic film were attached to the activated stainless steel in the front and the back of the stack, to obtain an intensity profile of the beam. The radius of the activity from stainless on gafchromic film is used in the imaging process program Image-J, which can be seen on figure 3.5. The gafchromic films were scanned, and the intensity data (**x and y arrays**) were obtained by inverting the scanned image, and drawing a line segment along the beam spot that automatically created an position dependent intensity array. The intensity profile can be fitted to a Gaussian, which is shown examplewise in figure 3.6, which is the horizontal beam profile in the front and the back of the stack. In the assumption that the beam was underfilled, it was important to build confidence in that the beamspot was ca. 1 cm in diameter, which was done estimating the full width half maximum of the Gaussian profile. The FWHM over SS1 was 1.2017 cm horizontally ( $\sigma^2 = 0.2604 \text{ cm}^2$ ) and 1.1420 cm vertically ( $\sigma^2 = 0.2352 \text{ cm}^2$ ). The FWHM over SS2 was 0.6706 cm horizontally ( $\sigma^2 = 0.0811 \text{ cm}^2$ ) and

Table 3.1: Characterization of each foil, along with calculated mass density. Each length is measured in mm, and mass in grams.

Foil	Length1 (mm)	Length2 (mm)	Thickness (mm)	Mass (g)	Mass density (mg/cm <sup>2</sup> )
SS1					...
Ni01	25.228	25.293	0.0285	0.1453	22.772 ± 0.138
Ir01	24.943	24.968	0.0295	0.3436	55.174 ± 0.053
Cu01	25.553	24.883	0.0341	0.1420	22.338 ± 0.048
Fe01	24.400	26.068	0.0278	0.1274	20.030 ± 0.110
Ni02	25.288	25.428	0.0295	0.1487	23.118 ± 0.096
Ir02	24.923	25.005	0.0278	0.3465	55.601 ± 0.238
Cu02	25.443	25.550	0.0348	0.1451	22.325 ± 0.028
Fe02	25.525	23.800	0.0274	0.1216	20.017 ± 0.034
Ni03	25.295	25.210	0.0270	0.1425	22.338 ± 0.066
Ir03	24.885	24.983	0.0243	0.3459	55.643 ± 0.121
Cu03	25.560	25.508	0.0343	0.1455	22.313 ± 0.043
Fe03	26.113	25.235	0.0310	0.1315	19.948 ± 0.114
Ni04	25.303	24.888	0.0273	0.1304	20.704 ± 0.068
Ir04	24.960	24.833	0.0261	0.3471	56.000 ± 0.109
Cu04	25.153	25.603	0.0333	0.1435	22.284 ± 0.027
Ni05	25.325	25.495	0.0263	0.1406	21.768 ± 0.045
Ir05	24.948	24.958	0.0256	0.3435	55.161 ± 0.081
Cu05	25.213	25.573	0.0334	0.1447	22.443 ± 0.028
Ni06	25.530	25.195	0.0285	0.1471	22.861 ± 0.123
Ir06	24.760	24.960	0.0240	0.3444	55.731 ± 0.088
Cu06	25.343	25.513	0.0340	0.1448	22.396 ± 0.012
Ni07	25.338	25.278	0.0268	0.1479	23.092 ± 0.078
Ir07	24.955	25.008	0.0278	0.3538	56.685 ± 0.085
Cu07	25.625	25.248	0.0326	0.1444	22.320 ± 0.014
Ni08	25.205	24.950	0.0256	0.1409	22.409 ± 0.124
Ir08	24.723	24.985	0.0281	0.3585	58.030 ± 0.130
Cu08	25.370	24.885	0.0333	0.1414	22.401 ± 0.033
Ni09	25.220	25.378	0.0257	0.1392	21.741 ± 0.073
Ir09	24.670	24.993	0.0273	0.3494	56.669 ± 0.043
Cu09	25.390	26.455	0.0331	0.1506	22.425 ± 0.041
Ni10	25.285	24.405	0.0271	0.1425	23.093 ± 0.024
Ir10	24.973	24.980	0.0270	0.3435	55.065 ± 0.055
Cu10	25.470	25.338	0.0355	0.1440	22.314 ± 0.047
SS2					...
P-degrader					...
Ni neutron monitor					...

0.5783 cm vertically ( $\sigma^2 = 0.0603 \text{ cm}^2$ ).

Normally the beam broadens throughout the stack due to scattering. As we can see, this is not the case, since the beam is stopped in the targetstack, and therefore we do not know how much the beam truly scatters. This gives a higher uncertainty. The stainless steel (which consists of ..) has fast decay time. However since it emits beta-particles, the radius will slightly increase, and the true beam spot is slightly smaller. Thus the estimated FWHM values for SS1 seem to be within the criterion for underfilled targets.

### 3.2.3 Counting on high purity detectors

Seven different detectors were used, six IDM Ortec detectors (detectors 1-6) with detector diameter 85 mm, detector length 30 mm and hole depth 15 mm, and one Germanium detector (detector 7) with detector diameter 64.9 mm, detector length 57.8 mm and hole depth 48.6 mm **from detector diagrams**. Besides, IDM detectors were located in cave 4c (see figure 3.1), which have previously been used as



(a) The target stack in target holder

(b) Target holder placed in the end of beam tube

Figure 3.4: Figure shows the target stack and how it was placed in the beam tube.

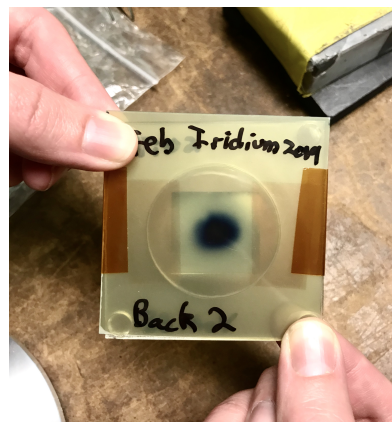
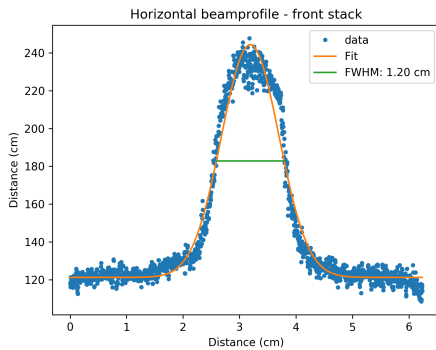
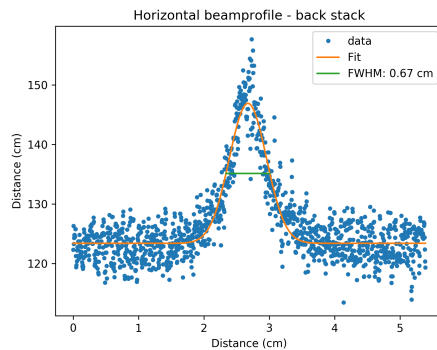


Figure 3.5: The gafchromic film on the activated SS1 foil.



(a) Horizontal intensity profile of SS1



(b) Horizontal intensity profile at SS2

Figure 3.6: Figure shows the intensity profile of the deuteron beam in the front and in the back of the stack horizontally.



Figure 3.7: The calibration point sources that were used in the efficiency calibration of the detector. ( $^{22}\text{Na}$  was excluded because it was difficult to work with. )

Table 3.2: The calibration point sources along with gamma lines used in the calibration of the detectors. \* indicates that the value has been averaged over two peaks with similar energy, less than 1 keV. For the intensity its just added together.

$^{137}Cs$		$^{133}Ba$		$^{152}Eu$	
$E_\gamma$	$I_\gamma$	$E_\gamma$	$I_\gamma$	$E_\gamma$	$I_\gamma$
32.005*	5.63*	53.1622	2.14	121.7817	28.53
36.3405*	1.02*	80.9979	32.9	244.6979	7.55
661.657	85.10	160.6120	0.638	295.9387	0.440
		223.2368	0.453	344.2785	26.5
		276.3989	7.16	367.7891	0.859
		302.8508	18.34	411.1165	2.237
		356.0129	62.05	244.4853*	3.125*
		383.8485	8.94	503.467	0.1524
				586.2648	0.455
				678.623	0.473
				688.670	0.856
				719.353*	0.345*
				778.9045	12.93
				810.451	0.317
				867.380	4.23
				963.712*	14.65*
				1112.076	13.67
				1212.948	1.415
				1299.142	1.633
				1408.013	20.87

radiation chamber. Thus, background radiation was present. For detector 7, there was led shielding around the detector. Spectra taken on the Germanium detector is preferred. In order to visualize the signal from the detector, Maestro (Multichannel Analyzer Emulation Software<sup>7</sup>) was used.

The detectors were calibrated for efficiency, peak shape and gamma-ray energy using  $^{137}Cs$  ( $t_{1/2} = 30.08$  years [6]),  $^{133}Ba$  ( $t_{1/2} = 10.551$  years [7]) and  $^{152}Eu$  ( $t_{1/2} = 13.517$  years [8]) point sources, using the gammalines listed in table 3.2. The calibration was done at various distances from the detector surface. The point sources can be seen on figure 3.7. The energy and peakshape calibration was done in FitzPeakz which is described in section 4.1.1. The efficiency calibration is described in section 4.2.

The iridium foils were counted within 15 minutes after end of beam, and the other foils following up after. All the foils were counted for ca. four weeks following end of beam, with short counts in the beginning to have good statistical data for the short-lived activities, and longer and longer counts as the shorter and medium-lived activities decayed out, to have good statistics (enough counts). Since the detectors were calibrated at various distances, the deadtime of the foils right after end of beam could be reduced, however, as high as 16-22% deadtime was present, but reduced to less than 5% within a certain time after end of beam.

---

<sup>7</sup><https://www.ortec-online.com/products/application-software/maestro-mca>

# Chapter 4

## Analysis

The analysis of estimating production cross sections consisted of multiple steps. To obtain the end of beam activities the peak areas (number of counts) were found with gamma-ray spectroscopy using FitzPeakz<sup>1</sup>. The efficiency calibration as a function of gammaray energy was done using <sup>137</sup>Cs, <sup>133</sup>Ba and <sup>152</sup>Eu point sources. The energy degradation in the foils were simulated using NPAT<sup>2</sup>, giving the deuteron flux as a function of energy. Along with the simulation and IAEA recommended cross sections for the monitor reactions<sup>3</sup>, the weighted average beam current was estimated in each foil.

### 4.1 Gamma-ray spectroscopy

The spectra were analyzed in FitzPeakz<sup>4</sup>. The mathematic algorithm in which FitzPeakz is based upon is SAMPO80<sup>5</sup>. The peaks are assumed Gaussian with an exponential tale on both sides of the peak. The exponential tale and Gaussian function are joined so function and first derivative are continuous. The algorithm searches for peaks by using the smooth second difference (derivative?) Particularly good for detecting small peaks on a high or low background. The peak areas are calculated by fitting the precalibrated modified Gaussian to the data with a weighted least squares formula using a parabolic background. Fitting intervals are determined automatically by the program. Peaks separated by less than 4 times the average fwhm are fitted together.

For each spectra, a report file containing peak energy, centre channel, full width half maximum, significance, goodness of fit, peak area, uncertainty in peak area, gammas per second, uncertainty in gammas per second and a background estimation for each peak was provided. The most important parameters were the energy, the peak area  $N_C$  and uncertainty in peak area. Peak area was needed for the activity calculation in equation 2.15 which is an important parameter in the calculation of the cross section (equation ??), and in the calculation of the efficiency for the calibration sources (equation 4.1). Gammas per second (also called countrate) was used to get an indication if the rate of gammas, which were used as a critical tool to evaluate background contamination in a peak for instance.

Figure 4.1 shows an example of a gamma ray spectrum for one of the iridium spectra (Ir05) approximately 35 hours after end of beam. Figure 4.2 shows the X-ray region and gamma region of <sup>193m</sup>Pt.

The nuclei were identified on behalf of their gamma-ray energy. The feeding of multiple nuclei into one gamma-ray peak was avoided by using other gamma-lines.

#### 4.1.1 Energy and peak-shape calibration

Used calibration sources <sup>137</sup>Cs ( $t_{1/2} = 30.08$  years [6]), <sup>133</sup>Ba ( $t_{1/2} = 10.551$  years [7]) and <sup>152</sup>Eu ( $t_{1/2} = 13.517$  years [8]), which can be seen on figure 3.7.

<sup>1</sup><https://www.jimfitz.co.uk/fitzpeak.htm>

<sup>2</sup><https://pypi.org/project/npat/>

<sup>3</sup>[https://www-nds.iaea.org/medical/monitor\\_reactions.html](https://www-nds.iaea.org/medical/monitor_reactions.html)

<sup>4</sup><https://www.jimfitz.co.uk/fitzpeak.htm>

<sup>5</sup>[https://sci-hub.tw/https://doi.org/10.1016/0029-554X\(81\)90209-3](https://sci-hub.tw/https://doi.org/10.1016/0029-554X(81)90209-3)

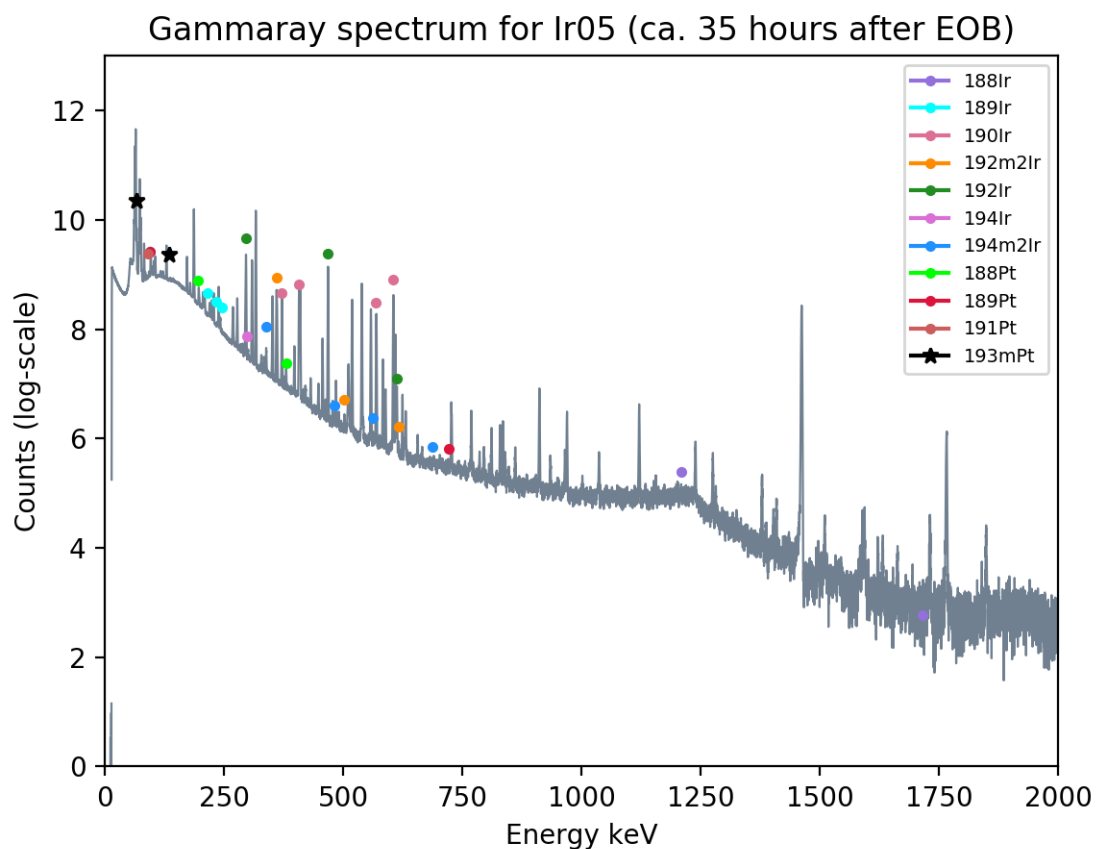


Figure 4.1: Gammaray spectrum for Ir05 taken approximately 35 hours after end of beam. Nuclei does not necessarily represent what is present in the spectrum, but where the peak would have been. Hard to include all since there are different decay times.

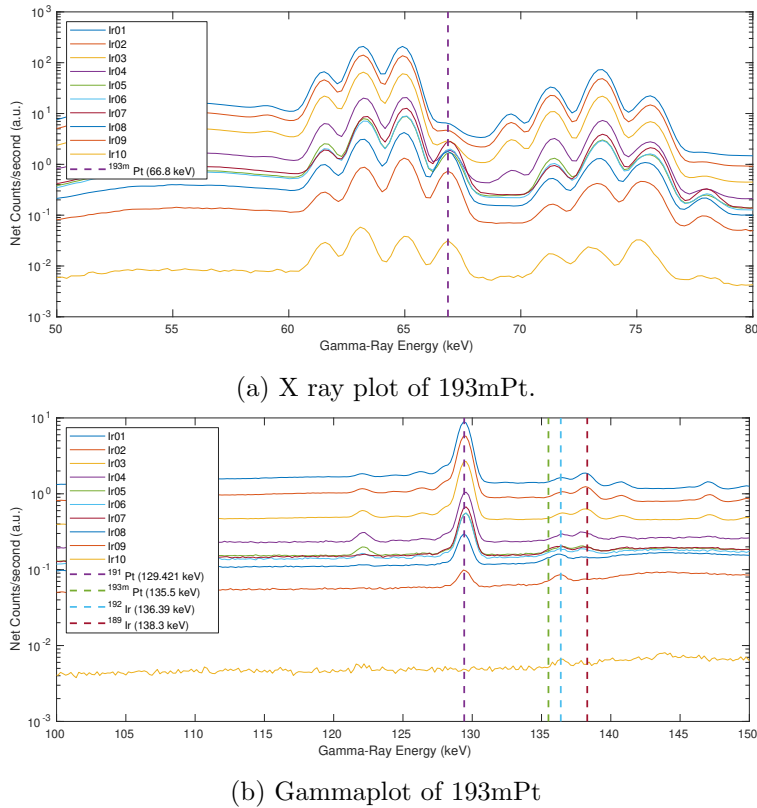


Figure 4.2: Which spectra are these??

The calculated peak locations and areas are finally corrected with energy and efficiency calibration data to yield peak energies and intensities. For the energy calibration, linear interpolation on a linear scale and for the efficiency calibration linear interpolation on a log-log scale are used in this code. Calibration errors are added to the peak location and intensity errors to give the final result (p.94). The peak shape calibration uses 7 parameters; two background peaks, peak height and location, peak width, distance from peak centroid to the starting point of exponential on either side. The minimization of the least-squares expression to solve for the peak parameters is done by a subroutine package with an iterative gradient algorithm utilizing the variable metric method. Minimization is terminated when all components in the next step change by less than  $10^{-8}$ , if four succeeding values of  $\chi^2$  are the same or if 100 iterations have been completed. The performed shape calibration can be checked with a few parameters, goodness of fit,  $\chi^2$  per degree of freedom, sigma and error correlation. Sigma below 5 and error correlation between -1 and 1 are acceptable values. (p.90)

From the webpage [jim-fitzy.com/calib.html](http://jim-fitzy.com/calib.html): Each detector was calibrated with peak shape and energy for the calibration sources. Fitzpeakz takes in energy (.enc) and peak shape (.shp) calibration source files, containing the energies listed in table 3.2. For the peak shape, the program determines the parameters of width and the amount of low energy tailing. The energy calibration and peak shape calibration was estimated to a 1st order function.

### 4.1.2 Background subtraction

How it was done very simple!!

## 4.2 Efficiency calibration

The efficiency calibration is an important factor in the calculation of the cross section in equation ???. The detector efficiency is the number of events registered divided by the events emitted by the source. The absolute efficiency can be divided into intrinsic and geometrical efficiency, where the intrinsic

efficiency is the number of events registered divided by the number of events hitting the detector. The intrinsic efficiency thus depends on the interaction cross section between incident particle and detector material. For neutral particles, the size of the detector affects the intrinsic efficiency, the larger crystal the larger the probability of interaction is. The geometrical efficiency is the radiation emitted by the source which hits the detector. (Techniques for Nuclear and Particle Physics Experiments. William R. Leo. Second Revised Edition. Springer Verlag Berlin Heidelberg GmbH, New York (1994). p. 121-122 )

The efficiency was measured using calibration point sources  $^{137}\text{Cs}$  ( $t_{1/2} = 30.08$  years [6]),  $^{133}\text{Ba}$  ( $t_{1/2} = 10.551$  years [7]) and  $^{152}\text{Eu}$  ( $t_{1/2} = 13.517$  years [8]). Figure 3.7 shows the calibration points sources ( $^{22}\text{Na}$  was excluded during the data-analysis since it only contains a single gamma-line and gave poorer results). On each calibration source, a reference date is given with an activity, which here is referenced to as  $A_0$  of the calibration sources.

Solving Equation 2.15 for efficiency,  $\epsilon$ , the analytical efficiency as a function of gamma-ray energy and intensity is

$$\epsilon(E_\gamma) = \frac{N_C \lambda}{A_0 I_\gamma (1 - e^{-\lambda \Delta t_c}) e^{-\lambda \Delta t_d}} \quad (4.1)$$

where  $\lambda$  is the decay constant and  $N_C$  is the number of counts in the measured spectra, and  $\Delta t_d$  is the delay time since the reference date. The analytical efficiency gives one single value for the efficiency at energy  $E_\gamma$ , but we want a continuous function which gives the efficiency at any gamma-energy. A model based upon Gallagher, W. J., Cipolla, S.J. (1974) was applied which takes the probability of penetration through the deadlayer of the detector and the probability of interaction in the detector volume into account

$$\epsilon(E_\gamma) = B_0 + \underbrace{(e^{-B_1 E_\gamma^{B_2}})}_{\text{dead layer}} \underbrace{(1 - e^{-B_3 E_\gamma^{B_4}})}_{\text{interacting with volume}} \quad (4.2)$$

where  $B_i$  is optimum parameters minimizing the  $\chi^2$  in the scipy optimizing curve fit function<sup>6</sup>). Figure 4.3 shows an example of an efficiency curve for a detector at a specific distance from the detector. The uncertainty of the efficiency was estimated using equation A.6 numerically. For each source, the gamma-lines with the intensities which were used to calculate the efficiency points for each source is listed in table 3.2.

### 4.3 End of beam activities

The end of beam activities were estimated by extrapolating backwards in time, with the measured activities at various timepoints after the end of beam. The activities as a function of time sine EOB was calculated using equation 2.14, along with a self-attenuation correction:

$$A(\Delta t_d) = \frac{N_C \lambda}{\epsilon_\gamma (1 - e^{-\lambda \Delta t_d}) e^{-\mu \rho \Delta r / 2}} \quad (4.3)$$

where  $\mu$  is the photoon attenuation coefficients from the XCOM photon cross section database<sup>7</sup>, and  $\rho \Delta r$  is the mass density of the foil. The gammas which were used are listed in tables B.2, B.1, B.3 and B.4 for iron, nickel, copper and iridium respectively. The gamma-ray self-attenuation (which is typically less than 0.2 % (Iron paper, Andrew)) correction is based on the assumption that all activity that is made is located midway in the foil thicknesses. In reality however, the activity profile will follow the same shape as the excitation function over the energy range that expands over the foil, **if we assume that the stopping power dE/dx=0 which is a good estimation for thin foils less than 100 mg/cm<sup>2</sup>??** (since activity and cross section are proportional). We do not know the excitation function

<sup>6</sup>[https://docs.scipy.org/doc/scipy/reference/generated/scipy.optimize.curve\\_fit.html](https://docs.scipy.org/doc/scipy/reference/generated/scipy.optimize.curve_fit.html)

<sup>7</sup><https://www.nist.gov/pml/xcom-photon-cross-sections-database>

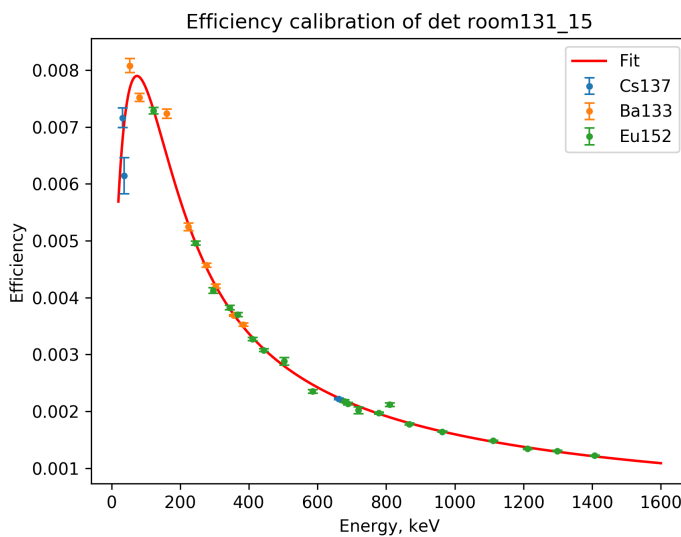


Figure 4.3: An example of an efficiency curve with exact points calculated from equation 4.1 and a curve fit from equation 4.2.

ahead of time, and the excitation function does not change much either, since the foil thicknesses are so thin. So instead, this simplification is done, assuming that the average attenuation is through half of the foil thickness.

The equation describing the shape of the decay curve is given in equation 2.3 for single decay or 2.4 for multiple decay. Decay chains of single and two-step decay ( $n=1,2$ ) was sufficient in this analysis;

$$A = A_0 e^{-\lambda \Delta t_d}, \quad \text{single step decay} \quad (4.4)$$

and

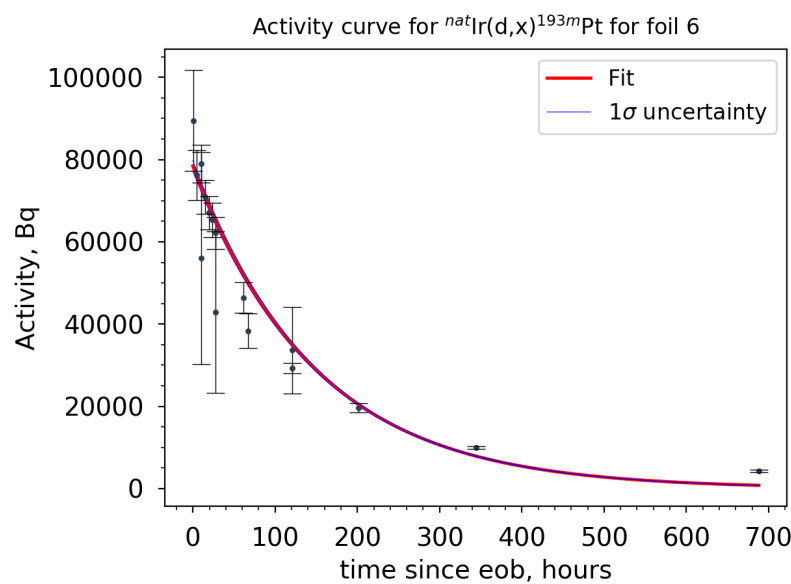
$$A_2(t) = \lambda_n \left[ A_{1,0} \lambda_1 \frac{(e^{-\lambda_1} + e^{-\lambda_2})}{\lambda_1 - \lambda_2} + A_{2,0} e^{-\lambda_2 t} \right], \quad \text{two step decay} \quad (4.5)$$

where subnumber 1 is the parent nucleus, and subnumber 2 is the daughter nucleus. Parent activity is calculated from single step decay. The uncertainty was treated as **covarianced variables?**

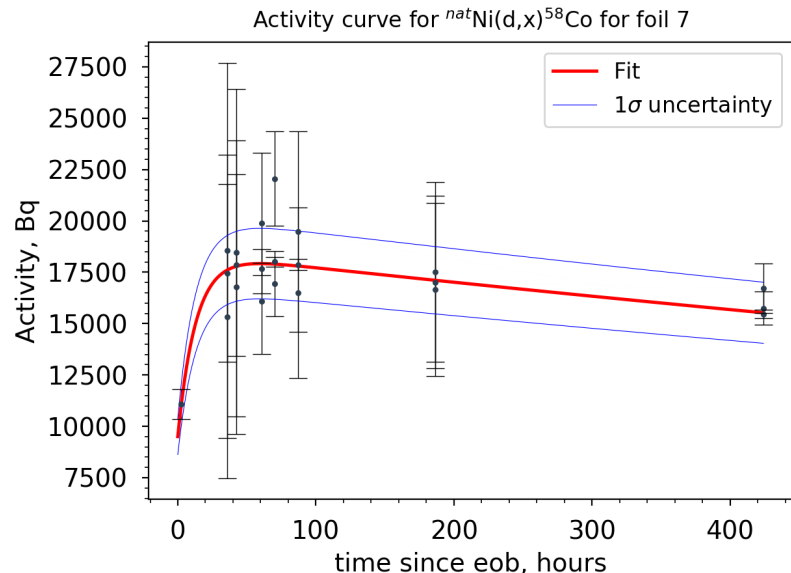
The way in which the extrapolation was done was the scipy optimize curve fit function, where the  $A_0$  of the daughter was the optimizing parameter. Since there is only one optimized parameter, there was no covariance and the uncertainty was calculated using equation A.13. In the cases where neither parent or daughter activity were known, which were the case for the monitor reaction  $^{58}\text{Co}$  with  $^{58m}\text{Co}$  decaying into the ground state by internal conversion, both parent and daughter activity were optimizing parameters which are very correlated and thus the uncertainty in end of beam activity was calculated A.6. Figure 4.4 shows two examples of the two different activity curves; one step decay for  $^{193m}\text{Pt}$  ( $t_{1/2}=4.33$  days) and two step decay for the monitor product  $^{58}\text{Co}$  ( $t_{1/2}=70.86$  days) with feeding from the isomer  $^{58m}\text{Co}$  ( $t_{1/2}=9.10$  hours).

## 4.4 Estimation of the beam current

The beamintegrator measured a current of 128.5 nA in front of the beam stack. However in order to have precise cross section measurements, the beamcurrent in each foil was estimated. The IAEA recommended monitor reactions (2017)  $^{nat}\text{Ni(d,x)}^{61}\text{Cu,56,58Co}$ ,  $^{nat}\text{Cu(d,x)}^{62,63,65}\text{Zn}$  and  $^{nat}\text{Fe(d,x)}^{56}\text{Co}$  were used to obtain a weighted average beam current in each foil solving equation 2.15 for beam current  $\Phi$ :



(a) Activity of  $^{193m}\text{Pt}$  ( $t_{1/2}=4.33$  d) produced from iridium. The end of beam activity was estimated using a one step decay (equation 4.4)



(b) Activity of  $^{58}\text{Co}$  ( $t_{1/2}=70.86$  d) produced from nickel. The end of beam activity is estimated using a two step decay (equation 4.5. The feeding is from  $^{58m}\text{Co}$  ( $t_{1/2}=9.10$  h.)

Figure 4.4: Two examples of activity curves. The uncertainty in activity decreases with increasing time since end of beam which is due to longer counts decreases the uncertainty. (from theory, counting statistics)

$$\Phi(E) = \frac{A_0}{N_T \sigma(E)_{\text{mon}} (1 - e^{-\lambda \Delta t_{\text{irr}}})} \quad (4.6)$$

Equation 4.6 builds upon the thin target assumption, which implies that the energy degradation  $dE/dx=0$ . However, we know that there is an energy distribution, which was estimated using NPAT's (Nuclear Physics Analysis Tool) Ziegler simulation. The ziegler code simulates the deuteron transport based upon the Anderson & Ziegler stoppingpower formalism, using Monte Carlo simulations **write a few sentences in theory...** The code provides the full deuteron energy and flux degradation in each foil,  $d\phi/dE$ , which can be visualized for the iridium foils in figure 4.5. Can be seen that as the deuteron energy is degraded, the mean value is shifted towards the low energy side, and the peak width increases. As stoppingpower is inversely proportional to the charge particle energy ( $-\frac{dE}{dx} \propto \frac{1}{\beta^2}$ , bethe block), and along with scattering taking place towards the end of stack, the low energy tail is more degraded, and we see a skew towards the low energy, creating a broader energy-flux profile and a shift of the mean value (centroid). This shift leads to an increasing uncertainty in energy. The (normalized) flux-weighted average energy for each foil was calculated, **ironpaper: which takes into account the slowing down of deuterons, and reports effective energy centroid of each foil**, using the energy distributions  $d\phi/dE$  provided by the Ziegler code:

$$\langle E \rangle = \frac{\int E \frac{d\phi}{dE} dE}{\int \frac{d\phi}{dE} dE} \quad (4.7)$$

The uncertainty in beam energy is divided into low energy and high energy tale, with the FWHM split by the centroid (figure 4.5).

Likewise, the energydependent monitor IAEA cross sections need to be flux-weighted over each foil. In order to do this, a spline interpolation over the energy array over each foil provided by the Ziegler simulation was spline interpolated with the IAEA recommended cross section data. Thus, the monitor cross section in equation 4.6 is modified to

$$\sigma(\langle E \rangle) = \frac{\int \sigma_{\text{mon}} \frac{d\phi}{dE} dE}{\int \frac{d\phi}{dE} dE} \quad (4.8)$$

With the end of beam activities for the monitor reactions, number of target nuclei and the flux-weighted IAEA cross sections, the beam current as a function of the flux-weighted average beam energy was estimated for each reaction in each foil.

#### 4.4.1 Variance minimization of the deuteron transport calculations

In theory, the estimated beam current of a charge particle beam should be constant, until completely stopped, since the majority of the incident particles does not interact in nuclear reactions, but only lose energy via elastic and inelastic scattering. However, non-consistant values of the beam current, especially in the back of the stack can be due to energy bins being assigned wrongly in the energy distribution simulation done in Ziegler or a systematic error in the areal density which gets progressively worse further back in the stack (Niobium paper, Andrew). A way to work around these errors was to perform a variance minimization varying the beam energy and the areal density of the foils with 20% increase and decrease systematically, and estimate the reduced  $\chi^2$  (equation A.4) over compartment 3,6 and 9. Variance minimization (Andrew's Niobium and iron paper + <https://sci-hub.tw/https://doi.org/10.1016/j.nimb.2016.09.018>).

For compartment 3 ( $E_d=25$  MeV) all seven monitor reactions were above threshold, thus 6 degrees of freedom. However, early in the target stack, the scattering was low, and the  $\chi^2$  does not tell how well the energy bin assignment work further back in the stack. For compartment 6 ( $E_d=18$  MeV), all the six possible monitor reactions (for nickel and copper) were above threshold, and it gave a good estimate of how the beam current was developing throughout the stack. In compartment 9 ( $E_d=10$  MeV), five monitor reactions are above threshold (except for  $^{62}\text{Zn}$ ). At the very end it is possible to

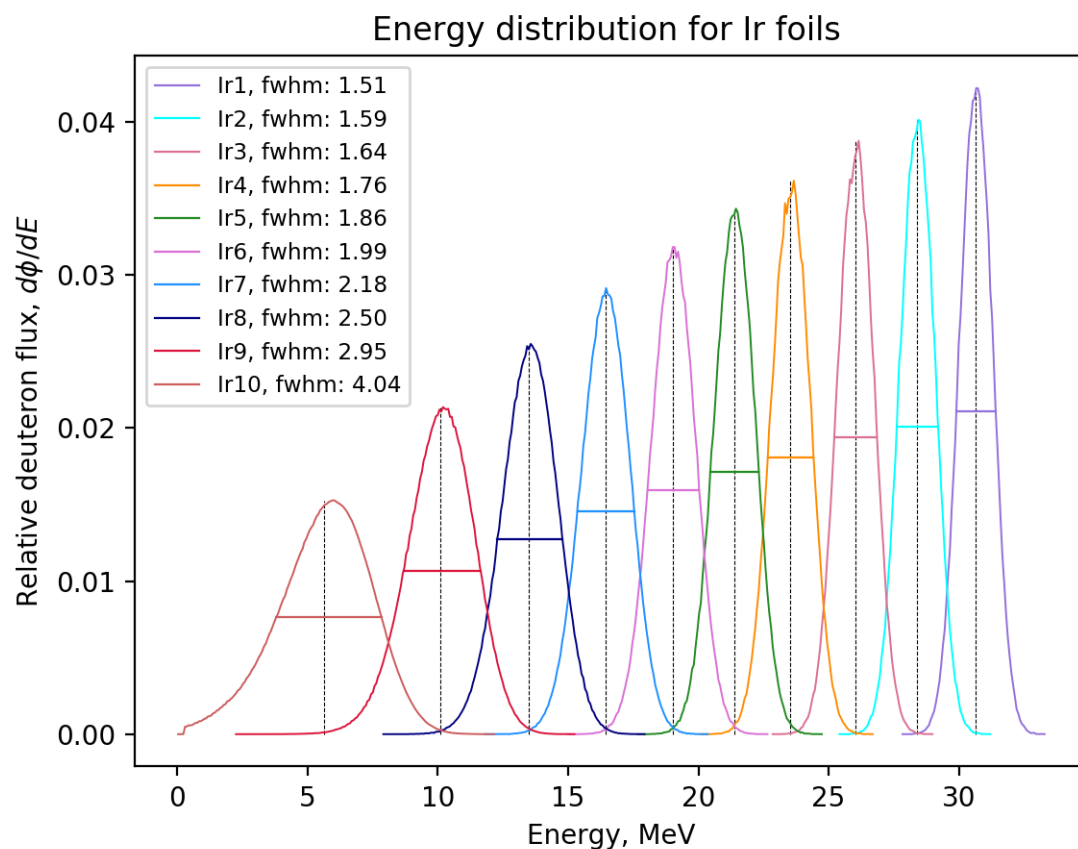


Figure 4.5: Iridium energy flux distribution over the 10 foils. As the energy degrades, skewed and larger full width half max. The vertical line in each peak is the mean value. This indicates that at lower energies, the right uncertainty is greater than the left uncertainty in the peak.

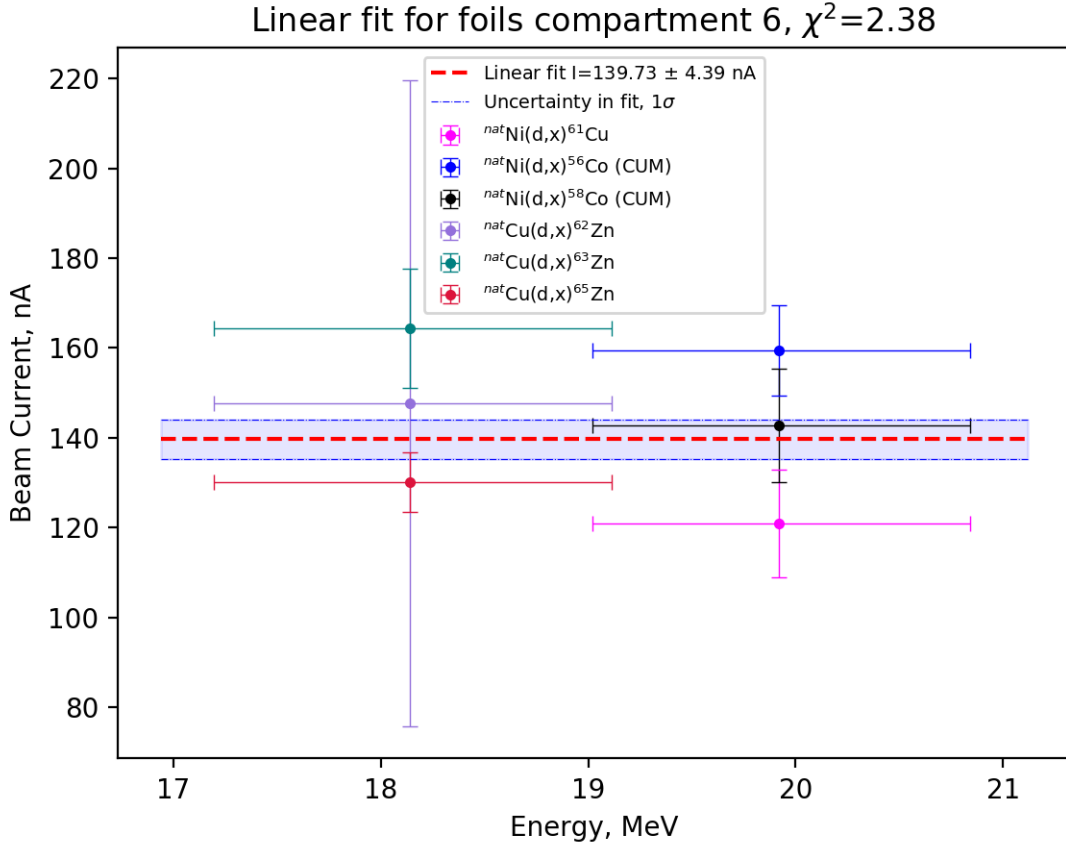


Figure 4.6: The estimated (uncertainty weighted) beamcurrent over compartment 6.

see the full effect of the scattering.

With the assumption that the beamcurrent loss is zero over one compartment, a linear fit-model (using the scipy optimize curvefit function) with a slope equal to zero was used to estimate the beam current in each compartment, and with the estimated  $\chi^2$ .

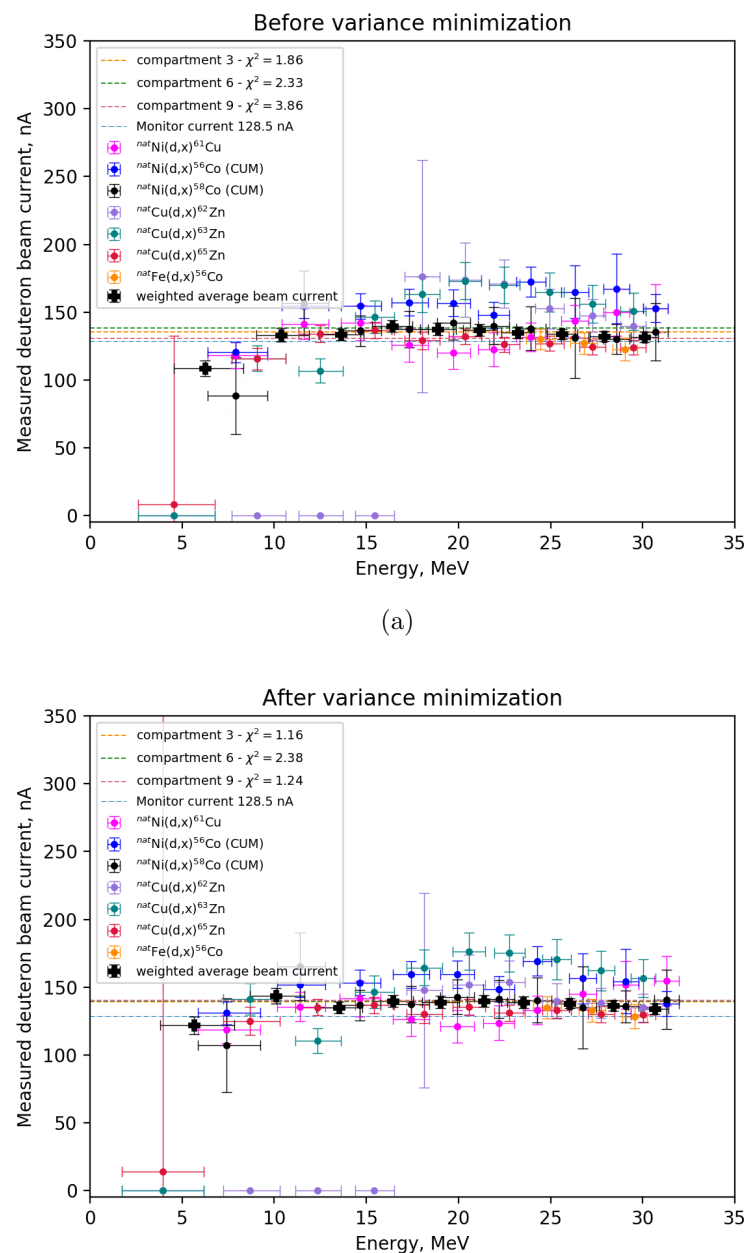
Figure 4.6 shows the uncertainty weighted linear fit over compartment 6.

Figure 4.7 shows the beam current before and after variance minimization, and the weighted average beam currents are listed in table 4.1 estimated before and after the variance minimization. After variance minimization, the beam current estimated in each compartment (stabled lines) were similar, and meanwhile the weighted  $\chi^2$  was about the same in compartment 6, it has improved in compartment 3 and very visible in compartment 9. In general the points are also more aligned.

For cross section calculations, equation ?? is used, with the estimated weighted average beam current. Figure 4.8 shows the estimated cross sections for the monitor reactions, using the weighted average beam current over all monitor foils. The recommended monitor cross section data for the monitor reactions are also plotted, which was used in the cross section calculation.

## 4.5 Cross section measurements

With all variables for cross sections, cross sections can be calculated using equation ???. Since the energy was a flux-weighted average beam energy, the value that is provided as cross section is a flux-averaged cross section. An accurate measure of the cross section as a function of deuteron energy was possible, as the thin foils provides smaller average beam energy intervals, and it makes it possible to have more measurements if thick foils are replaced with several thinner (one single foil represents a single measurement). **in theory: Thin foils also produce minimal amounts of radioactivity, thus the**



(b) A 2% increase in beam current and a 4.25% increase in areal density gave the overall most consistent beam current, with reasonable values for the weighted .

Figure 4.7: Beam current before and after variance minimization.

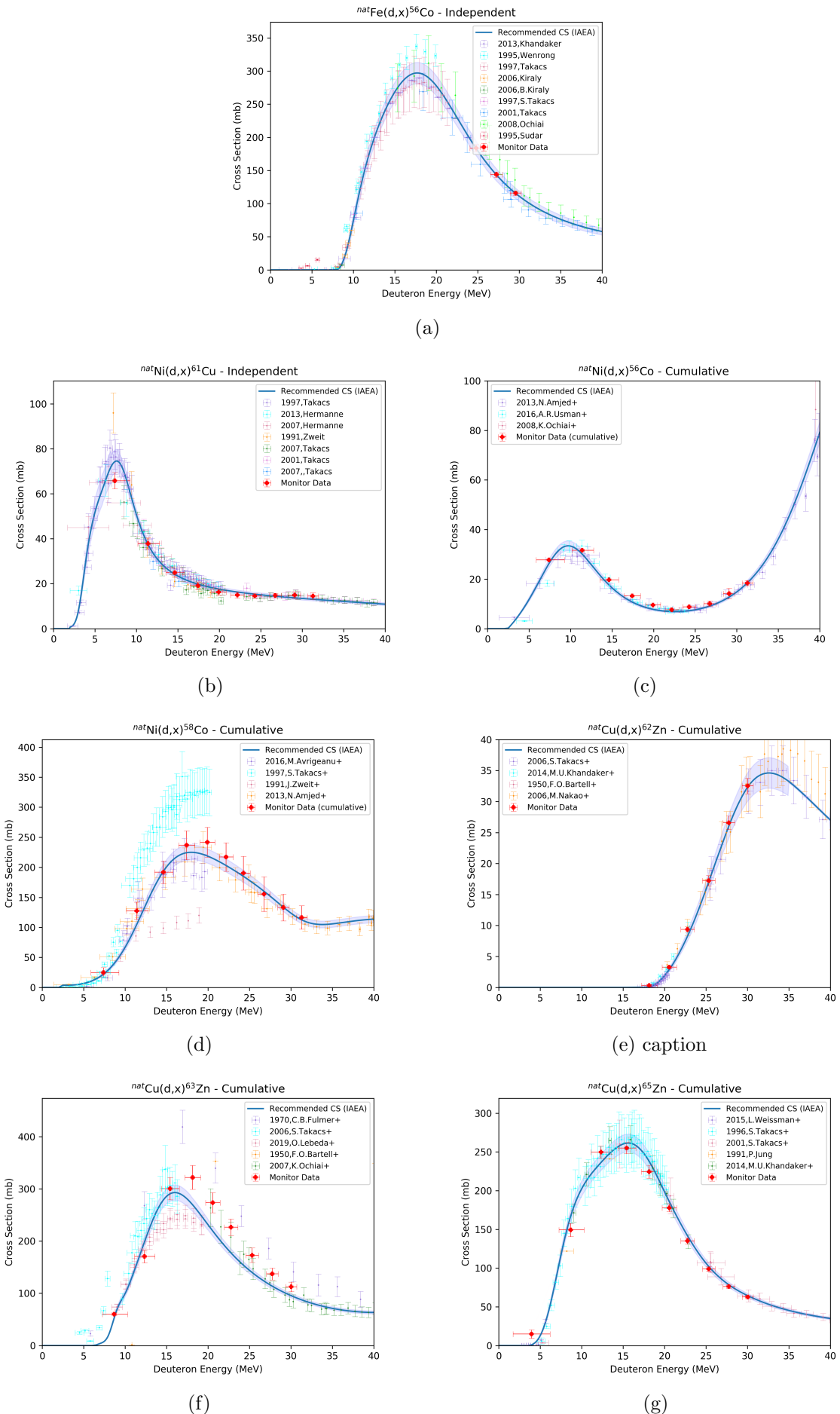


Figure 4.8: Figure shows the estimation of monitor cross section using the estimated weighted average beam current for each reaction (not the total). It is compared along with the recommended (IAEA) monitor data, and other experimental data

Table 4.1: The weighted average beam current before and after variance minimization in each compartment. The beam current on the 88-Inch Cyclotron beam integrator was 128.5 nA.

Compartment	Before	After
01	131.56 $\pm$ 3.64	134.08 $\pm$ 3.70
02	132.23 $\pm$ 3.74	136.42 $\pm$ 3.83
03	133.81 $\pm$ 3.64	138.02 $\pm$ 3.75
04	134.89 $\pm$ 4.21	138.88 $\pm$ 4.31
05	136.85 $\pm$ 4.21	139.67 $\pm$ 4.29
06	137.40 $\pm$ 4.53	138.85 $\pm$ 4.58
07	139.55 $\pm$ 4.37	139.77 $\pm$ 4.37
08	133.60 $\pm$ 4.27	134.96 $\pm$ 4.32
09	133.16 $\pm$ 5.04	143.59 $\pm$ 5.67
10	108.49 $\pm$ 5.80	121.75 $\pm$ 6.65

deadtime of the detector and the dose to humans is low.

Thin foils decreases the energy width, making a more precise measurement dependent on energy. However the reported cross sections are flux-averaged over the energy distribution subtended by each foil.

The cross sections are reported as independent if there is nothing decaying into it (beta feeding or from isomer transition), which means that the first observed element in a decay chain is reported as cumulative unless it is the first possible element (which are the nuclei with one more proton more than the target nuclei, which for this experiment is Platinum (from Ir), Zink (from Cu), Copper (from Ni) and Cobalt (from Fe). If there is feeding, and the half life is much shorter or much longer than the specific nuclei, can choose appropriate timewindow and report as independent, when we know that the feeding has either died out or is very low!

If possible with feeding: added together to get cumulative or subtracted giving independent. Multiplying by branching ratio.

The measured cross sections in this work was compared to previous experimental data, along with reaction modelling codes TALYS<sup>https://sci-hub.tw/https://doi.org/10.1016/j.nds.2012.11.002</sup>, TENDL, ALICE20 and CoH.

Optical model calculations performed first,

Talys takes in projectile, target element (specific isotope or all stable target isotopes), energy array with desired spacing and upper limit energy.

For COH: To get both 191Ir and 193Ir to run, we had to adjust the parameter "tweakSD", which adjusts the effective single-particle state density for a particular particle emission channel. In the end, we ran with tweakSD=0.25 for both outgoing alphas and neutrons (protons were unaffected). In other words, we set the single-particle state density for outgoing alphas and neutrons [(d,xa) and (d,xn) reactions] to be 25% of what they normally are, which is a HUGE change.

from talys cite p. 2843-2844: TENDL is developed from talys (TALYS evaluated Nuclear data Library). This library consists of a complete set of nuclear reaction data for incident neutrons, photons, protons, deuterons, tritons, Helium-3 and alpha particles, from  $10^5$  eV up to 200 MeV, for all 2430 isotopes from 6Li to 281Ds that are either stable or have a half-life longer than 1 second. All data are completely and consistently evaluated using a software system consisting of the TALYS nuclear reaction code, and other software to handle resonance data, experimental data, data from existing evaluations, and to provide the final ENDF-6 formatting, including covariance information. The result is a nuclear data library with mutually consistent reaction information for all isotopes and a quality that increases with yearly updates. To produce this library, TALYS input parameters are adjusted for many nuclides so that calculated cross sections agree with experimental data, while for important nuclides experimental or evaluated data are directly included. Also feedback from integral measurements is processed into the data libraries. For nuclides for which (almost) no experimental data exists, default TALYS calculations based on global models and parameters are used.

Dont understand this part.....



# Chapter 5

## Discussion

### 5.1 Uncertainties

While the uncertainties in intensity, and in efficiency, ..... the uncertainties in the number of counts (and number of decays???) have an independent impact on each activity and thus cross section. The relative efficiency uncertainty is typically ca. 5%. .....

For the activities, the scipy curve fit uses chi squared to estimate the A0, and thus the error is weighted. If there is enough points with low uncertainty the uncertainty in A0 will also be low. That is important, for the beam current and the cross sections.

### 5.2 Beam current variance minimization

The variance minimization (figure 4.7) led to an overall more constant weighted average beam current after the variance minimization, where Ni(d,x)<sup>56</sup>Co and Cu(d,x)<sup>62</sup>Zn in particular were affected positively. The other reactions have about the same values before and after variance minimization. With the exception of compartment 9, where the beam current is higher than before the variance minimization, the beam currents are more consistent (table 4.1). Figure 4.7 clearly show an improvement of <sup>56</sup>Co and <sup>63</sup>Zn. The gamma-lines used to estimated the end of beam activities are listed in tables B.2, B.1, B.3 and B.4 for iron, nickel, copper and iridium respectively.

The monitor reaction <sup>nat</sup>Fe(d,x)<sup>56</sup>Co ( $t_{1/2}=77.236$  d) decays by  $\epsilon$  (100%) to stable <sup>56</sup>Fe [9]. Figure 4.8a shows that the three cross section measurements are in very well agreement with the recommended IAEA cross sections. This nucleus can be produced directly via <sup>56</sup>Fe(d,2n) ( $Q=-7.6$  MeV), <sup>57</sup>Fe(d,3n) ( $Q=-14.2$  MeV) and via <sup>d,4n</sup> (-25.3 MeV). There is no feeding for this decay channel and the reaction is independent <sup>56</sup>Co. The activity of <sup>56</sup>Co was thus estimated using onestep decay, with the gamma-lines listed in table B.2. All the gamma-lines are not present in background spectra with the exception of 1238.288 keV (66.46%), with a countrate of  $10^{-2}$ , which is very low in comparison to the countrate of the peak. In general, <sup>56</sup>Co shares multiple lines with <sup>56</sup>Mn. **should exclude or do background subtraction??**. On figure 4.7, the datapoints for this reaction are in well agreement with the weighted average beam energy, but has a slightly lower value. The variance minimization did not change the beam current very much for this reaction.

The monitor reaction <sup>nat</sup>(d,x)<sup>61</sup>Cu ( $t_{1/2}=3.339$  h) decay by  $\epsilon$  (100%) to stable <sup>61</sup>Ni [10]. Figure 4.8b shows datapoints which are in accepted agreement with the recommended IAEA cross sections. However, in foil 1 and foil 2 the cross section is slightly overestimated, while foil 3-5 underestimates slightly. The cross section is difficult to measure precisely when the derivative of the excitation function is high, so the cross section of foil 10 does not fit the peak accurately, but all the measured cross section points are within the energy uncertainty. The activity was estimated using onestep decay, with the gamma-lines listed in table B.1. On figure 4.7, it is clear that the measured beam current points "oscillates" between the weighted average beam current, but the points are in well compliance with the weighted average beam current. The variance minimization did not change the beam current

very much for this reaction.

The monitor reaction  $\text{nat}(\text{d},\text{x})^{56}\text{Co}$  ( $t_{1/2}=77.236$  d) decays by  $\epsilon$  (100%) to stable  $^{56}\text{Fe}$  [9]. Figure 4.8c shows the cumulative cross section with feeding from  $^{56}\text{Ni}$  ( $\epsilon : 100\%$ ). However, since the Q-value (table B.1) for  $\text{Ni}(\text{d},\text{x})^{56}\text{Ni}$  is 24.6884 MeV, the activity of  $^{56}\text{Co}$  in foil 1, 2 and 3 which was exposed for deuterons energy above the threshold, were estimated using twostep decay, while the remaining activities were estimated using one-step decay. The gamma-lines used for the identification and estimation of activity are listed in table B.1. The cross section reported from IAEA is cumulative, thus the independent cross sections were summed to get the cumulative cross section. The measured cross section points are slightly overestimated in comparison to the recommended IAEA cross sections, but are in well compliance with the experimental data, and are thus accepted results. On figure 4.7, the overall estimated beam current for this monitor reaction shows that it is clearly high in comparison to the weighted average beam energy. However, the variance minimization helped to "pull" the values down, especially in foils 1-3.

The monitor reaction  $^{\text{nat}}\text{Ni}(\text{d},\text{x})^{58}\text{Co}$  (figure 4.8d) shows the cumulative cross section of the ground state ( $t_{1/2}=70.86$  d) which decay by  $\epsilon$  (100%) with feeding from the isomer  $^{58m}\text{Co}$  ( $t_{1/2}=9.19$  h, IT:100%) [11]. Since  $^{58m}\text{Co}$  lack observable gamma-lines, the activity was estimated using twostep decay, with two optimizing parameters, inwhich were the activities for both of them independently. Since the IAEA cross section is cumulative, the cross section provided here is the summation of the two independent cross sections of the isomer and ground state. Within uncertainties the estimated cumulative cross section of  $^{58}\text{Co}$  is in well agreement with the recommended IAEA cross sections. On figure 4.7, the estimated beam current is also in very well agreement with the weighted average beam energy. The variance minimization did no change the values very much.

Figure 4.8e shows the monitor cross section for reaction  $^{\text{nat}}\text{Cu}(\text{d},\text{x})^{62}\text{Zn}$  ( $t_{1/2}=9.193$  h) decays by  $\epsilon$  (100%) [12]. The activities for this product was estimated using onestep decay. The measured cross sections appear to be in well agreement with the IAEA recommended cross sections. This reaction has a Q-value (table B.3) -15.490 MeV, thus the cross section in foil 7-10 is below threshold and therefor zero. In figure 4.7, the measured beam current in foils 1-3 is in perfect compliance with the weighted average beam current, and foils 4-6 are slightly above. The uncertainty in the measured beam current in foil 6 is overestimated, which is because it is close to the threshold. The variance minimization contributed to "pulling" the beam current down, and reduce the uncertainty in foil number 6.

Figure 4.8f shows the monitor cross section for reaction  $^{\text{nat}}\text{Cu}(\text{d},\text{x})^{63}\text{Zn}$  ( $t_{1/2}=38.47$  m) decay by  $\epsilon$  (100%) [13]. The activities for this product was estimated using onestep decay. The Q-value (table B.3) for this reaction is -6.3733 MeV, and the reaction cross section is below threshold for foil 10. The cross sections estimated in foils 7-9 are in well compliance with the recommended cross section data, but the cross section in foil 8 is slightly underestimated. The rest of the points are off, and are overestimated, but it follows the expected shape. The beam current on figure 4.7 shows that the overall beam current for foils 1-6 is high, the beam current in foil 7 and 9 are in agreement with the weighted average beam current, and the beam current in foil 8 is underestimated. This particular cross section was tested for various beam currents with low values of  $\chi^2$  in each compartment, but did not change the cross section in figure 4.8f such that it was aligned within uncertainties of the IAEA cross section. This particular reaction thus contributes to the weighted average beam energy being pulled up slightly.

Figure 4.8g shows the monitor cross section for reaction  $^{\text{nat}}\text{Cu}(\text{d},\text{x})^{65}\text{Zn}$  ( $t_{1/2}=243.93$  d) decays by  $\epsilon$  (100%) [14]. The activities for this product was estimated using onestep decay. The measured cross sections in foil 1-5 is in excellent agreement with the IAEA recommended cross section data. The remaining points are within uncertainties agreeing with the IAEA data. The beamcurrent in figure 4.7 shows that the beam current for this reaction is in well compliance wiht the weighted average beam energy, and likewise  $\text{Fe}(\text{d},\text{x})^{56}\text{Co}$ , the values are slightly lower contributing to a lower weighted average beam energy. The variance minimization did not affect the estimated beam current particularly much.

To summarize, using the weighted average beam current (figure 4.8) in general shows good compliance with the recommended IAEA cross sections that were used in the calculation of the beam current. In general, the measured cross section values are within uncertainty of the recommended cross section. The high energy measurements are in general more precise, and it is clear that where it is a rapid change in the excitation function, the energy bins seems to be slightly wrong. However, the measured cross sections are within uncertainty in both energy and cross section, with the exception being the high energy exponential tail for  $^{63}\text{Zn}$ .

## 5.3 Cross section products

In general, the products that were expected were mostly seen, with a few exceptions which were mainly due to too short counting time and shared gamma-lines which were particularly evident in the iridium products. The Coulomb barrier for the compound nuclei resulting from deuterons were ca. 13.2 MeV for the compound platinum nuclei ( $^{\text{nat}}\text{Ir}(\text{d},\text{x})^{193^*/195^*}\text{Pt}$ ), ca. 6.7 MeV for the compound copper nuclei ( $^{\text{nat}}\text{Ni}(\text{d},\text{x})^{60^*/62^*/63^*/64^*/66^*}\text{Cu}$ ), ca. 6.9 MeV for the compound zink nuclei for protons... ( $^{\text{nat}}\text{Cu}(\text{d},\text{x})^{65^*/67^*}\text{Zn}$ ) and ca. 6.4 MeV for the compound cobalt nuclei for protons ( $^{\text{nat}}\text{Fe}(\text{d},\text{x})^{56^*/58^*/59^*/60^*}\text{Co}$ ). The observed products resulting from iridium were constrained by the high Coulomb barrier, and only radionuclides of iridium and platinum were observed.

In general, there was no clear evidence of decay of compound nuclei by emission of tritons, deuterons or  $^3\text{He}$  nuclei. As mentioned in the section ??, for compound nuclear reactions, decay channels with emission of single nucleons are more fed, and alpha-particles due to the large binding energy, but all energetically possible decay channels will be fed. The cross sections for those reaction channels were thus too low or overshadowed by other compound peaks to be observed.

Due to energy straggling and scattering the further back in the stack, the uncertainty in energy increases with beam energy.

### 5.3.1 Nickel products

From nickel, there are 5 stable nuclei,  $^{58}\text{Ni}$  (68.077%),  $^{60}\text{Ni}$  (26.223%),  $^{61}\text{Ni}$  (1.1399%),  $^{62}\text{Ni}$  (3.6346%) and  $^{64}\text{Ni}$  (0.9255%), resulting in many possible reactions. The observed reactions were the cumulative measurements of  $^{52}\text{Mn}$ ,  $^{59}\text{Fe}$ ,  $^{55}\text{Co}$ ,  $^{56}\text{Co}$ ,  $^{57}\text{Co}$ ,  $^{58}\text{Co}$ ,  $^{60}\text{Co}$ ,  $^{56}\text{Ni}$ ,  $^{65}\text{Ni}$  and  $^{57}\text{Ni}$  and the independent measurements of  $^{54}\text{Mn}$ ,  $^{56}\text{Co}$ ,  $^{57}\text{Co}$ ,  $^{58}\text{Co}$ ,  $^{58m}\text{Co}$ ,  $^{60}\text{Cu}$  and  $^{64}\text{Cu}$ . In addition, the  $^{59}\text{Fe}$  (cumulative),  $^{58}\text{Co}$  (independent) cross sections are the first reported.

#### $^{52}\text{Mn}$ (cumulative)

The cumulative cross section for  $^{52m}\text{Mn}$  ( $t_{1/2}=21.1$  m) and  $^{52g}\text{Mn}$  ( $t_{1/2}=5.591$  d) [15] is reported in table... and can be seen in figure ... The isomer decays by  $\epsilon$  (98.25%) to  $^{52}\text{Cr}$  and by IT (1.75%), hence the feeding is relatively low. The isomer and ground state share multiple gamma-lines, and the first registered count of  $^{52}\text{Mn}$  are about 2-3 hours after end of beam, where the isomer had more or less decayed out. Therefor, it was difficult to extract independent measurements of the isomer and ground state.  $^{52}\text{Mn}$  takes place in the decay chain decaying via  $\epsilon$  from  $^{52}\text{Co}$  (104 ms),  $^{52m+g}\text{Fe}$  (45.9 s/8.275 h) to stable  $^{52}\text{Cr}$ , but there was no evidence of the two former, thus this reaction is not subject to much feeding. The end of beam activities were estimated using onestep decay, with the gamma-lines listed in table B.1. This product can be produced via  $^{58}\text{Ni}(\text{d},2\alpha)$  with reaction Q-value -1.2356 MeV, via  $^{60}\text{Ni}(\text{d},2\text{n}2\alpha)$  with reaction Q-value -21.6226 MeV and via  $^{61}\text{Ni}(\text{d},3\text{n}2\alpha)$  with reaction Q-value -29.4427 MeV. It is clear that the alpha-reaction channels are constrained by the Coulomb barrier, which is approximately 14.4 MeV for alpha-particles from the compound nuclei, as the first observed measurement was at 14.63 MeV. With the two latter reaction channels, the excitation function steadily increases, and combined becomes a large compound peak.

The measured datapoints agrees with previous experimental data [16], [17], [18], [19]. CoH overestimates the compound peak, but follows the shape well, but the maximum seems to be slightly shifted towards lower energies. This is also the case for TENDL and TALYS, but here the cross sections are underestimated. ALICE follows the experimental shape of the excitation function, and although it underestimates the cross section values, it is still a relatively good model. **EMPIRE**—.

### $^{54}\text{Mn}$ (independent)

The independent cross section for  $^{54}\text{Mn}$  ( $t_{1/2}=312.20$  d) [20], are reported in table ... and in figure ..., and decays via  $\epsilon : 100\%$  to stable  $^{54}\text{Cs}$ . The end of beam activities were estimated using a onestep decay the gamma-line listed in table B.1.  $^{54}\text{Mn}$  can be produced via  $^{58}\text{Ni}(\text{d},2\text{p}\alpha)$  with reaction Q-value -8.5383 MeV, via  $^{60}\text{Ni}(\text{d},2\alpha)$  with reaction Q-value -0.6296 MeV, via  $^{61}\text{Ni}(\text{d},\text{n}2\alpha)$  with reaction Q-value -8.4497 MeV and via  $^{62}\text{Ni}(\text{d},2\text{n}2\alpha)$  with reaction Q-value -19.0454 MeV. The alpha-reaction channel is here also constrained by the alpha-barrier, which was approximately 14.4 MeV. However, there is one measurement below this alpha barrier, at 11.41 MeV. **is this due to tunneling of the alpha-particle or or an error, most likely not any other decay channel because of the energy threshold? The background spectra from cave 4c (detector 1-6) shows a gamma-line which is less than 1 keV in difference from the gamma-line used in the estimation of the cross section?** The datapoints before 14 MeV is most likely false. Should do background subtraction? The compound peak increases steadily as more reaction channels open.

For the two first points measured at 11.41 and 14.63 MeV, there was no previous experimental data: [16–19]. , and comparing to the reaction models, the suggested cross section is zero. However, the measured cross sections are very low. The point measured at 17.42 MeV is higher than the previous experimental data. **should not trust those 3 points? Threshold region is weird.** The measured points at 19.92 MeV and above are in agreement with the previous experimental data. For the measured points above 24.28 MeV, there is excellent compliance with the CoH reaction model and the previous measured datapoints, and the shape is also excellent. TALYS and TENDL follows the same shape, but underestimates the magnitude of the excitation function. ALICE suggests a higher threshold for the reaction, and that the compound peak is shifted towards higher energies. The magnitude also seems to be underestimated. **EMPIRE**...

### $^{56}\text{Mn}$ (cumulative)

????

### $^{59}\text{Fe}$ (cumulative)

The cumulative measurement of  $^{59}\text{Fe}$  ( $t_{1/2}=44.490$  d) [21] in table ... and figure .... It is part of a decay chain in which  $^{59}\text{Fe}$  is the first observed element. It decay by  $\beta^-$ -decay (100%) to stable  $^{59}\text{Co}$ . The end of beam activities were estimated using the gamma-line in table B.1, and fitted to a onestep decay.  $^{59}\text{Fe}$  can be produced via  $^{58}\text{Ni}(\text{d},3\text{p})$  with a reaction Q-value -12.3596 MeV,  $^{61}\text{Ni}(\text{d},2\alpha)$  with reaction Q-value -20.3596 MeV,  $^{62}\text{Ni}(\text{d},\text{p}\alpha)$  with reaction Q-value -2.6597 MeV and via  $^{64}\text{Ni}(\text{d},2\text{n}p\alpha)$  with reaction Q-value -19.1549 MeV. The threshold for the reaction is constrained by the Q-value of the two former reactions, and the alpha barrier for the third one. The first measured point is at 22.19 MeV, and the cross section is on the order of  $10^{-1}$  mb. From the reaction models, the suggested threshold is at ca. 14 MeV, which is the energy of the alpha-barrier. The reason that this nucleus was not observed at lower energies is due to the low activity and the long half-life. There was no activity registered at 24.28 and 29.08 MeV, but the cross section values of 22.19, 26.74 and 31.29 MeV is in great agreement with the CoH reaction model.

Alice overestimates the the compound peak, and oscillates. TALYS and TENDL follows the threshold well, but overestimates the cross section for higher energies. **EMPIRE**—

**$^{55}\text{Co}$  (cumulative)**

The cumulative measurement of  $^{55}\text{Co}$  ( $t_{1/2}=17.53$  h [22]) can be seen in figure ... and table ... It is part of a decay chain and this is the first element observed.  $^{55}\text{Co}$  decays by  $\epsilon$  (100%) to long-lived  $^{55}\text{Fe}$  ( $t_{1/2}=2.744$  y), which was not observed. The gamma-lines used in this identification are listed in table B.1. The most intense gamma-lines for this radionuclide were 477.2 keV (20-2%), 931.1 keV (75%) and 1408.5 keV (16.9%). However, due to background contamination in the former and latter, only the 931.1 gamma-line was used, along with other relatively weakly fed gamma-lines. The end of beam activity was estimated using one-step decay.  $^{55}\text{Co}$  can be produced via  $^{58}\text{Ni}(\text{d},\text{n}\alpha)$  with reaction Q-value -3.6 MeV,  $^{60}\text{Ni}(\text{d},3\text{n}\alpha)$  with reaction Q-value -23.9 MeV and via  $^{61}\text{Ni}(\text{d},4\text{n}\alpha)$  with reaction Q-value 31.8 MeV. **The first observed value for  $^{55}\text{Co}$  is at 7.39 MeV (foil 10). Peaks are no background. However, the threshold for the experimental data are also below alpha barrier. Is the tunneling more probable for this reaction? Because other reactions are not possible..**

The data points from this work agrees very well with previous experimental data [16–19, 23–26]. CoH overestimates the cross section, but does a good job estimating the shape. ALICE is slightl lower but does a pretty good job magnitude wise. TALYS and TENDL does not do a very good job, and does not estimate a distinct compound peak.

 **$^{56}\text{Co}$  (independent and cumulative)**

The cumulative cross section with feeding from  $^{56}\text{Ni}$  and independent cross section measurement of  $^{56}\text{Co}$  ( $t_{1/2}=77.236$  d) [9] can be seen in figures ,,, respectively and in table .... decays by  $\epsilon$  (100%) to stable  $^{56}\text{Fe}$ . The gamma-lines used to estimate this radionuclide is listed in table B.1, and the activity was estimated using a two-step decay, estimating the independent measurement of  $^{56}\text{Co}$ . Since the  $^{56}\text{Ni}$  reaction has a high threshold above 25 MeV, it was only feeding from the first 3 foils, so the three first was fitted using a two step decay and the latter were used single decay. To achieve the cumulative cross section, the  $^{56}\text{Ni}$  and  $^{56}\text{Co}$  cross sections were added. The cumulative and independent cross section looks very much the same, and looking at the cumulative, the feeding from  $^{56}\text{Ni}$  is in general very low due to the low cross section in comparison to  $^{56}\text{Co}$  (can be seen in table .... ).

This nuclide can thus be produced from  $^{56}\text{Ni}$  feeding or directly via  $^{58}\text{Ni}(\text{d},\alpha)$  ( $Q = 6.5$  MeV), via  $^{60}\text{Ni}(\text{d},2\text{n}\alpha)$  ( $Q=-13.9$  MeV), via  $^{61}\text{Ni}(\text{d},3\text{n}\alpha)$  ( $Q=-21.7$  MeV) or via  $^{62}\text{Ni}(\text{d},4\text{n}\alpha)$  ( $Q=-32.3$  MeV). In addition,  $^{58}\text{Ni}(\text{d},2\text{n}2\text{p})$  is possible with reaction Q-value -21.8 MeV. The first measured point is at 7.39 MeV which is equal to foil 10. experimental data have been shown before. **WHY IS IT POSSIBLE? tunneling, other stuff, spin???** . The first compound peak is due to the tunneling prob of the first reaction, and the opening of the second. The compound peak in this work suggests higher peak slightly shifted to higher energies. The second increase is due to other reaction channels opening up. There is a large coverage on experimental data for the cumulative reaction [16–19, 23–26] (some of them are stated cumulative, but some are also just assumed cumulative). ALICE does a terrible job, And the experimental data seems to be somewhere inbetween estimation done by TENDL and CoH. Both TALYS, TENDL and CoH does a good job for cross sections from 15-20 MeV, but CoH does the best job. **EMPIRE....** For the independent reaction, there is no explicit experimental data. The shape of the reaction models follows the data and the cumulative shape from other plot well. ALICE does a good job here. TENDL does the best job for low energy points while CoH, does the best job. All models follows the shape very well, but ALICE underestimates.

 **$^{57}\text{Co}$  (independent and cumulative)**

The independent and cumulative cross section for  $^{57}\text{Co}$  ( $t_{1/2}=271.74$  d) is reported in this work.  $^{57}\text{Co}$  decays by  $\epsilon$  (100%) to stable  $^{57}\text{Fe}$ , and is subject to feeding from  $^{57}\text{Ni}$  ( $t_{1/2}=35.60$  h) [27]. Can be seen in figure ... and in table ... The two strong gamma-lines 122.06065 (85.60%) and 136.47365 (10.68%) were used in the analysis, and was not subject to feeding from other nuclei. 122.06065 was however present in some background spectra in cave 4C, but with count rates in the order of  $10^{-3}$  it was ignored as it did not impact the result. With the feeding from  $^{56}\text{Ni}$ , the end of beam activity was estimated using twostep decay, with the  $A_0$  of  $^{57}\text{Co}$  being the optimizing parameter. This nuclide can be produced via  $^{58}\text{Ni}(\text{d},\text{n}2\text{p})$  ( $Q=-10.4$  MeV),  $^{60}\text{Ni}(\text{d},\text{n}\alpha)$  ( $Q=-2.5$  MeV),  $^{61}\text{Ni}(\text{d},2\text{n}\alpha)$  ( $Q=-10.3$  MeV)

and via  $^{62}\text{Ni}(\text{d},3\text{n}\alpha)$  ( $Q=-20.9$  MeV). The shape of the independent excitation function predicts that the threshold opens about 7 MeV, which is where the first measured point in this work predicts, with cross section 1.29 mb, and the excitation function increases once the two reaction channels from  $^{58}\text{Ni}$  and  $^{61}\text{Ni}$  opens. The compound peak also increases once the reaction channel from  $^{62}\text{Ni}$  opens at ca. 20 MeV. There is no previous experimental data for the independent measurement. TENDL, and TALYS predicts the magnitude quite well, but the peak seems to be shifted slightly towards lower energies, also counts for ALICE, which is too low in magnitude. Measured datapoints inbetween ALICE and TALYS, but TALYS closest magnitude wise!

The cumulative cross section is in well agreement with previos experimental data for lower energies, at higher energies the previos experimental data scatters. The data from this work lays in the middle of the data [16–19, 23–26]. **comment on curves**

#### $^{58m+g}\text{Co}$ (independent and cumulative)

The independent cross section of  $^{58m}\text{Co}$  and  $^{58g}\text{Co}$  are reported, along with the cumulative cross section of both. The isomer ( $t_{1/2}=9.10$  h) decay by IT (100%) to the ground state ( $t_{1/2}=70.86$  d), which decays to stable  $^{58}\text{Fe}$  [28]. The cross sections can be seen in figures .. and table .. The gamma-lines used to identify the ground state are listed in table B.1, with the most intense gamma-line at 810.7593 keV (99.450%) not being subject to background of feeding from other nuclei. For the isomer, there was no observed gamma-lines (with the only and most intense one being 24.889 keV (0.0397%)), so the activity for both of them was estimated using a two-step decay with the end of beam activities of the both serving as optimizing parameters. The groundstate can be produced via  $^{58}\text{Ni}(\text{d},2\text{n})$  ( $Q=-1.8$  MeV),  $^{60}\text{Ni}(\text{d},\alpha)$  ( $Q=6.1$  MeV),  $^{61}\text{Ni}(\text{d},\text{n}\alpha)$  ( $Q=-1.7$  MeV),  $^{62}\text{Ni}(\text{d},2\text{n}\alpha)$  ( $Q=-12.3$  MeV) and via  $^{64}\text{Ni}(\text{d},4\text{n}\alpha)$  ( $Q=28.8$  MeV), and the isomer can be produced equally, with the Q-value being the energy level higher (can be seen in table B.1).

#### what about the threshold, ift barrier?

The independent measurement of the isomer (figure ..) does not quite agree with the previous experimental data from Avrigeanu et. al. (2016) [24]. Avrigeanu et. al. used the same method, by minimization of the Bateman equataion, along with a direct measurement of the 24.9 keV gamma-line, which was consistent within 10% (correctly written?). One of the reason that it is hard to say is that a twostep decay with two optimizing parameters bring uncertainties to the second optimizing parameter, as they are correlated. The previous experimental data agrees well with TENDL and TALLYS, while this work agrees more with CoH, magnitude wise. The shape of the excitation function seems to be right for ALICE, TALYS and TENDL, but for CoH the compound peak seems to be shifted towards lower energies.

The independent measurement of the ground state (figure ...), does not have any reported independent measurements (the work done by Avruigeanu et. al. (2016) posted independent of the isomer but cumulative ground state). TALYS and TENDL agrees very well with the measurements in this work. CoH is too high magnitude wise, but predicts the shape very well. ALICE is too low magnituse wise and the compound peak is shifted towards higher energies.

The cumulative cross section of the ground state can be seen in figure ..., qith the two cross sections summed. This data agrees well with the experimental data from Zweit (1991), Amjad (2013) and Avrigeanu (2016) [19, 24, 26]. The work done by Takacs (1997) [25], are systematically higher for higher energies, in which the explanation that the nuclear activity was measured before the complete decay of the isomer was represented in the article. The work done by Takacs et al. however matches well with TENDL and TALYS magnitudewise. CoH does quite a good job in predicting the shape and magnitude of the excitation function. ALICE and TENDL are too high magnitude wise and seem to follow the shape of the independent ground state measurements. ALICE does not do a good job. **EMPIRE?**

### $^{60}\text{Co}$ (cumulative)

The cumulative measurement for  $^{60}\text{mCo}$  ( $t_{1/2}=10.467$  m) and  $^{60g}\text{Co}$  ( $t_{1/2}=1925.28$  d) [29] is reported in figure ... and table .... The isomer decays by IT (99.75%) and by  $\beta^-$  (0.25%).  $^{60}\text{Co}$  is the first observed element in a decay chain, and decay by  $\beta^-$  (100%) to stable  $^{60}\text{Ni}$ . Due to the long half-life of the ground state, long counts was required to have a low statistical error. Due to the short half-life of the isomer, independent measurements of the isomer and ground state were not possible to extract.  $^{60}\text{Co}$  is present in the background, and it was necessary to use background subtraction. perhaps should include 1173 keV even though it is fed by  $^{55}\text{Co}$ . Then only use counts registered after 170 hours?. with The activity was estimated using a one-step decay.  $^{60}\text{Co}$  can be produced via  $^{60}\text{Ni}(\text{d},2\text{p})$  with reaction Q-value -4.3 MeV,  $^{61}\text{Ni}(\text{d},\text{n}2\text{p})$  with reaction Q-value -12.1 MeV, via  $^{61}\text{Ni}(\text{d},\alpha)$  with reaction Q-value 5.6 MeV, and via  $^{64}\text{Ni}(\text{d},2\text{n}\alpha)$  with reaction Q-value -10.9 MeV. The first observed cross section was at 11.41 MeV, and within uncertainty, this can be when the  $^{61}\text{Ni}(\text{d},\text{n}2\text{p})$  reaction channel opens, combined with  $^{60}\text{Ni}(\text{d},2\text{p})$  reaction channel which opens at ca. 4 MeV. The excitation function steadily increases as the alpha-barrier is overcome, and all the reaction channels open.

TENDL, TALYS and CoH suggests a compound peak with a maximum at ca. 21 MeV. The experimental data does no agree clearly with this, and this work suggests that the compound peak should be shifted towards higher energies. The previous experimental data [16–18, 24] compared to this work is inconsistent. The work done by Takacs et. al. (2007) was based upon the expectation that the excitation function would increase above 25 MeV, and increase steadily up to 80 mb at 50 MeV. The estimated cross sections (above 25 MeV?) were estimated using a spline fit, and thus the values are higher than expected??. The data in this work seems to agree well with the work done by Usman et. al. (2016) and Avrigeneau et. al. (2016). Due to the long half-life of this nuclide, it was difficult to have statistically enough number of counts.

### $^{56}\text{Ni}$ (cumulative)

The cumulative measurement of  $^{56}\text{Ni}$  (6.075 d) decays by  $\epsilon$  (100%) to  $^{56}\text{Co}$  ( $t_{1/2}=77.236$  d).  $^{56}\text{Ni}$  is the first observed element of a decay chain with the parent being  $^{56}\text{Cu}$  ( $t_{1/2}=93$  ms) [9], and is therefor reported as cumulative. The gamma-lines used in the estimation of end of beam activity is listed in table B.1, with 158.38 keV (98.8%) being the strongest gamma-line. All the gamma-lines were used with the exception of 269.50 (36.5%) which was matched with background radiation in cave 4C. The end of beam activity was estimated using onestep decay. The nuclide can be produced via  $^{58}\text{Ni}(\text{d},3\text{np})$  ( $Q=-24.7$  MeV). From figure ..., it is clear that the threshold is at ca. 25 MeV, with the first measured point in this data being at 26.74 MeV, with cross section 0.06 mb.

The measured points in this work agrees well with other experimental datasets around threshold [16, 17, 19], for the three measured points in this work. CoH does a very good job with the prediction of the excitation function at this low cross section values. TENDL and ALICE also does a good job shapewise, but assumes slightly too high and lower threshold. ALICE predicts a way to rapid increase in the excitation function, it is clear that it is having trouble estimating the excitation function at this low cross sections. EMPIRE

### $^{57}\text{Ni}$ (cumulative)

The cumulative measurement of  $^{57}\text{Ni}$  ( $t_{1/2}=35.60$  h), and decays by  $\beta^+$  (100%) to  $^{57}\text{Co}$  ( $t_{1/2}=271.74$  d).  $^{57}\text{Ni}$  is the first observed element in a decay chain with  $^{57}\text{Cu}$  ( $t_{1/2}=196.3$  ms) [27] and is thus reported as cumulative. The gammalines which were used are listed in table B.1. The most intense gamma-line 1377.63 keV (81.7%) was excluded since the peak was contaminated with background radiation in cave 4C (in the order of  $10^{-2}$ ) which gave unrealistic measurements ca. 20 half-lives since end of beam. The other lines were sufficient to have a good measurement. This nuclide can be produced directly via  $^{58}\text{Ni}(\text{d},2\text{np})$  ( $Q=-14.4$  MeV) and via  $^{60}\text{Ni}(\text{d},3\text{np})$  ( $Q=-34.5$ ). In addition, the channel  $^{58}\text{Ni}(\text{d},\text{t})$  ( $Q=6.0$  MeV) seems to be fed, as the reaction cross section threshold seems to be at around 10 MeV, if we trust previous experimental data. As the  $^{58}\text{Ni}(\text{d},2\text{np})$  reaction channel opens, the cross section increases, and reaches more when ... Cant explain shape here ... The feeding from

$^{57}\text{Cu}$  has reaction Q-value of 24.0 MeV, and this might contribute to the compound peak being larger.

The data provided from this work is in well agreement with previous experimental data in the low energy region, but is too high for foil 1 and 2 [16, 17, 24–26]. ALICE overestimates the data, while ALICE and TENDL does a very good job with the experimental data. The CoH excitation function does a good job but suggests a more narrow peak and decreases before experimental data does.

#### $^{65}\text{Ni}$ (independent)

The independent measurement of  $^{65}\text{Ni}$  ( $t_{1/2}=2.51719$  h) is reported, which decays by  $\beta^-$  (100%) to stable  $^{65}\text{Cu}$  [30]. The gamma-lines used to estimate the end of beam activity are listed in table B.1 and are not subject to background radiation, nor feeding from other nuclei. The activity was estimated using a onestep decay. This product can only be produced via  $^{64}\text{Ni}(\text{d},\text{p})$  ( $Q=3873.5$  MeV). With the proton barrier for  $^{66}\text{Cu}$  being ca. 6.6 MeV, the threshold at 3 MeV makes sense? The reaction cross section is quite low, which is directly affected by the low abundance of  $^{64}\text{Ni}$  as natural nickel target.

Comparing to previous experimental data by Avrigeanu et. al. (2016) [24], the results obtained in this work is in quite good agreement, especially around the maximum of the peak. However, uncertainties are a little higher, and the high energy side of the tail seems to have moved a little to higher energies **why is this?**. From the reaction models, it is clear that TALYS & TENDL and CoH & ALICE uses different methods to estimate the peak. TENDL and TALYS get the shape best. **empire....**

#### $^{60}\text{Cu}$ (independent)

The independent measurement of  $^{60}\text{Cu}$  ( $t_{1/2}=23.7$  m) decays by  $\epsilon$  (100%) [29]. The gamma-lines listed in table B.1 are not subject to background feeding, nor feeding from other nuclei, with the exception of 1792.1 keV (0.082%) from  $^{55}\text{Co}$ . Since the gamma-line is weak and the half-life is much longer, this was ignored. The end of beam activity was estimated using onestep decay. The ways inwhich this nuclide can be produced is via  $^{60}\text{Ni}(\text{d},2\text{n})$  ( $Q=-9.1$  MeV),  $^{61}\text{Ni}(\text{d},3\text{n})$  ( $Q=-17.0$  MeV) or via  $^{62}\text{Ni}(\text{d},4\text{n})$  ( $Q=-27.6$  MeV). It is clear that the threshold opens at ca. 10 MeV, and that the compound peak is fed by the other possible reaction channels as the energy increases.

The datapoints in this work is in agreement with previous experimental data for Avrigeanu et. al. (2016), Ochiai et. al. (2006), and Takacs et. al. (1997) for low energies up to ca. 17 MeV [23–25]. A preposition for why these measurements are higher is not given in the article. ALICE seems to get the shape of excitation function good, while TENDL, TALYS and CoH does a good job magnitude wise. **EMPIRE...**

#### $^{61}\text{Cu}$ (independent)

The independent measurement of the monitor reaction alone can be seen in figure ....,

#### $^{64}\text{Cu}$ (independent)

The independent measurement of  $^{64}\text{Cu}$  ( $t_{1/2}=12.701$  h) is reported, and decays by  $\epsilon$  (61.5%) to stable  $^{64}\text{Ni}$  or by  $\beta^-$  (38.5%) to stable  $^{64}\text{Zn}$  [31]. The decay lacks gamma-lines, and from the gamma-decay of  $^{64}\text{Ni}$ , there is one gamma-line at 1345.77 MeV (0.475%), which is not subject to background feeding, or feeding from other nuclei. This nuclide can only be produced via  $^{64}\text{Ni}(\text{d},2\text{n})$  ( $Q=-4.7$  MeV), and the excitation function starts to increase around 5 MeV.

In comparison to previous experimental data [17, 24, 26], the uncertainties in the points measured in this work is much larger, but it follows a good shape. **why? is it because the counts were not counted for a sufficient time to have good statistics, since the gamma-line is weak?** . The intensity is quite low, and the peak was only observed once for each measurement, and never in multiple foils. Should have been counted over longer time periods. The uncertainty is directly related to the uncertainty

in the number of counts (foil 10: 47.8%, foil 9: 13.1%, foil 8: 48.1%, foil 6: 27.9%). So this is very clear. Even though particularly the measurement at 14.63 MeV is high, all points are still within uncertainties the same as previous data. ALICE follows the shape, of the experimental data, but all reaction models follows the data very well in both magnitude and shape. **EMPIRE...**

### 5.3.2 Copper products

Regarding the products produced from copper, the number of products are less, since there is only two stable target nuclei  $^{63}\text{Cu}$  (69.15%) and  $^{65}\text{Cu}$  (30.85%), and the nickel products (d,xnp) have many stable isotopes. For this target, independent measurements of  $^{65}\text{Ni}$  and  $^{64}\text{Cu}$ , and cumulative measurements of  $^{59}\text{Fe}$ ,  $^{60}\text{Co}$ ,  $^{61}\text{Co}$ ,  $^{61}\text{Cu}$ . In addition, the independent measurements of the monitor reactions  $^{62,63,65}\text{Zn}$  were made, which is described above. In addition, first measurement of  $^{61}\text{Co}$ . The Coulomb barrier for protons are ca. 6.8 MeV and for alpha ca. 14.4 MeV for the compound nucleus of  $^{65^*/67^*}\text{Zn}$ .

What did we expect??

#### $^{59}\text{Fe}$ (cumulative)

The cumulative measurement of  $^{59}\text{Fe}$  ( $t_{1/2}=44.490$  d) can be seen in figure ... and in table.. The nucleus decays by  $\beta^-$  (100%) to stable  $^{59}\text{Co}$  [21]. The gamma-lines used in the analysis is listed in table B.3, the two most intense gamma-lines 1099.245 (56.5%) and 1291.590 (43.2%) were used, which are not subject to background radiation, 1099.245 can be subject to feeding from  $^{61}\text{Cu}$  but with a large difference in half-life and intensity of the gamma-line, it is ignored. 1291.590 is not subject to feeding. The activity was estimated using a onestep decay. This nucleus is the first observed element in a decay chain and is therefor cumulative, with the possible feeding from  $^{59}\text{Mn}$  ( $t_{1/2}=4.59$  s, which can contribute via reaction  $^{65}\text{Cu}(\text{d},2\text{p}\alpha)$  ( $Q=-28.7$  MeV), as the cross section increases around 30 MeV.  $^{59}\text{Fe}$  can be produced directly via  $^{63}\text{Zn}(\text{d},2\text{p}\alpha)$  ( $Q=-8.8$  MeV) or via  $^{65}\text{Cu}(\text{d},2\alpha)$  ( $Q=1.7$  MeV). From figure ..., it is clear that the reaction channel opens at ca. 14 MeV, and the first measured point in this work is at 18 MeV (0.03 mb).

In comparison to previous data [32,33], the data from this work matches well well with data from Khandaker et. al. (2014), and for Tacaks et. al. (2006), the values are lower, but mostly within uncertainty. There is one measured point from Tacaks (2016) at ca. 5 MeV, which is not commented in the paper. In comparison to reaction models, CoH does a very good job magnitude and shape wise, TENDL and TALYS does a good job shape wise, and ALICE is off, predicting a large compound peak at 25 MeV.

#### $^{60}\text{Co}$ (cumulative)

The cumulative cross section of the isomer ( $t_{1/2}=10.467$  m, IT: 99.75%) and groundstate of  $^{60}\text{Co}$  ( $t_{1/2}=1925.28$  d) can be seen in figure... and in table.... The ground state decays by  $\beta^-$  to stable  $^{60}\text{Ni}$  [29]. The gamma-lines used in this analysis is listed in table B.3, with 1173.228 keV (99.85%) and 1332.492 (99.9826%).  $^{60}\text{Co}$  is present in the background, and it was necessary to use background subtraction. The cross section is reported as cumulative as there is possible feeding from the very long lived  $^{60}\text{Fe}$  ( $t_{1/2} = 2.62 \cdot 10^6$  y), but this was not seen.  $^{60}\text{Co}$  can be produced via  $^{63}\text{Cu}(\text{d},\text{p}\alpha)$  ( $Q=-0.5$  MeV) and via  $^{65}\text{Cu}(\text{d},2\text{n}\text{p}\alpha)$  ( $Q=-18.3$  MeV). On figure ... it is clear that the excitation function opens at ca. 10 MeV, and the first measured point in this work is at 11.41 MeV. The cross section increases to a compound peak when the next reaction channel opens.

In comparison to experimental data [32,33], this data aligns well with previous experimental data. As usual ALICE does a good job in predicting the compound peak shape wise. CoH is on the high side, but does better at higher energies, and TENDL does a very good job magnitude wise. TALYS is a little too low in magnitude.

**$^{61}\text{Co}$  (cumulative)**

The cumulative cross section of  $^{61}\text{Co}$  ( $t_{1/2}=1.649$  h) can be seen in figure.. and table .. It decays by  $\beta^-$  (100%) to  $^{61}\text{Ni}$  [10]. The gamma-line used in this analysis is listed in table B.3, which is not subject to background feeding, however, the shared gamma-line with  $^{61}\text{Cu}$  (which also  $\epsilon$ -decay into  $^{61}\text{Ni}$ ) with intensity 4.23% can contribute here. All points measured are above  $^{61}\text{Cu}$  threshold, so there might be some feeding here???. This cross section is reported as cumulative since there is possible feeding from short-lived  $^{61}\text{Fe}$  ( $t_{1/2}=5.98$  m), which can be produced via  $^{63}\text{Cu}(\text{d},4\text{p})$  ( $Q=-22.7$  MeV) and via  $^{65}\text{Cu}(\text{d},2\text{n}\alpha)$  ( $Q=-12.2$  MeV).  $^{61}\text{Co}$  can also be produced directly via  $^{63}\text{Cu}(\text{d},\text{n}3\text{p})$  ( $Q=-19.5$  MeV) or via  $^{65}\text{Cu}(\text{d},\text{n}p\alpha)$  ( $Q=9.0$  MeV). Dont see any evidence from the alpha-channels from either, as the reaction threshold is at ca. 20 MeV. Cross section increases rapidly after, due to both feeding and measurement?

No previous experimental data! Reaction models predicts well. While CoH and TENDL does a good job shapewise, in this energy region TALYS is closest in magintude, but seem to increase to slowly.

 **$^{65}\text{Ni}$  (independent)**

The independent measurement of  $^{65}\text{Ni}$  ( $t_{1/2}=2.51719$  h) can be seen in figure .... and in table .... The gamma-line used in the analysis can be seen in figure B.3, and it not subject to background.  $^{59}\text{Fe}$  can feed into this (1481.70, 0.059%) but since both cross section and intensity is low this was ignored. This product can only be produced via  $^{65}\text{Cu}(\text{d},2\text{p})$  ( $Q=-3.6$  MeV). From the figure, the threshold is suggested at ca. 10 MeV, but the first measured point here is at 18.14 MeV. The cross section is very low though. The uncertainty in this data is mainly caused by large uncertainty in efficiency (ASK ANDREW!!) and in the number of counts with relative uncertainty 22% and 26%. But as clearly can be seen the values are way to high in comparison to both experimental data [33] and in comparison to other reaction channel codes. These were also counted short time after end of beam. All reaction models and experimental data agrees quite well.

 **$^{61}\text{Cu}$  (cumulative)**

The cumulative cross section of  $^{61}\text{Cu}$  ( $t_{1/2}=3.339$  h) [10] can be seen in figure ... and table .... It decays by  $\epsilon$  (100%) to stable  $^{61}\text{Ni}$ . Three gamma-lines were used and are listed in table B.3, are not contaminated by background radiation, nor by other nuclei. The cross section is reported as cumulative with the possibility of feeding from  $^{61}\text{Zn}$  ( $t_{1/2}=89.1$  s,  $\epsilon$  (100%)) inwhich can be produced via  $^{63}\text{Zn}(\text{d},4\text{n})$  ( $Q=28.4$  MeV).  $^{61}\text{Cu}$  can be produced directly via  $^{63}\text{Zn}(\text{d},3\text{n})$  ( $Q=-15.5$  MeV) or via  $^{65}\text{Cu}(\text{d},5\text{n})$  ( $Q=-33.3$  MeV). The reaction channel opens at ca. 20 MeV, and it increases steadily, with the contribution from  $^{61}\text{Zn}$  feeding from ca. 30 MeV, and the latter direct reaction from ca. 34 MeV.

The measured datapoints are right around threshold, and the first observed point is at 25.32 MeV (1.18 mb). It aligns well with previous experimental data [34, 35], and CoH is doing an excellent job in predicting the excitation function. ALICE, TALYS and TENDL also do a very good job!

 **$^{64}\text{Cu}$  (independent)**

The independent measurement of  $^{64}\text{Cu}$  ( $t_{1/2}=12.701$  h) can be seen in figure.... an table .... It decays by  $\epsilon$  (61.5%) to stable  $^{64}\text{Ni}$  or  $\beta^-$  (38.5%) to stable  $^{64}\text{Zn}$  [14]. The gamma-line which was used is not subject to background radiation and is not shared with other nuclei. However, the intensity is weak, but the channel is heavily fed and the cross section is high which can be seen on figure.. This product can be produced via  $^{63}\text{Zn}(\text{d},\text{p})$  ( $Q=5.7$  MeV) or via  $^{65}\text{Zn}(\text{d},2\text{np})$  ( $Q=-12.1$  MeV). The reaction threshold is at ca. 2.4 MeV according to reaction modeling, and the first measured point in this work is at 3.94 MeV (73.54 mb). It is clear that the first reaction channel opens early,which contributes to the first compound peak, and then the other opens..

The experimental data [23, 32, 33, 35–37, 37, 38] aligns very well with this data. ALICE and CoH does a different approximation in comparison to TENDL and TALYS. TENDL and TALYS does a good job in predicting the compound peak, but should have been slightly broader. CoH and ALICE does not directly predict the compound peak, assumes no drop in the excitation function.

### 5.3.3 Iron products

Alpha barrier ca. 13.5 MeV, and proton barrier ca. 6.4 MeV.

$^{48}\text{V}$  (cumulative)

$^{51}\text{Cr}$  (cumulative)

$^{52}\text{Mn}$ (cumulative)

$^{54}\text{Mn}$  (independent)

$^{53}\text{Fe}$  (cumulative)

$^{59}\text{Fe}$  (independent)

$^{55}\text{Co}$  (independent)

$^{57}\text{Co}$  (independent)

$^{58}\text{Co}$  (cumulative)

can have isomer and groundstate

### 5.3.4 Iridium Products

$\alpha$ -barrier: ca 25 MeV, proton-barrier: ca 13.7 MeV

For a 33 MeV deuteron beam on the target stack, cross sections for  $^{188}\text{Ir}$ ,  $^{189}\text{Ir}$ ,  $^{190m1+g}\text{Ir}$ ,  $^{190m2}\text{Ir}$ ,  $^{192}\text{Ir}$ ,  $^{194m1+g}\text{Ir}$ ,  $^{194m2}\text{Ir}$ ,  $^{188}\text{Pt}$ ,  $^{189}\text{Pt}$ ,  $^{191}\text{Pt}$  and  $^{193m}\text{Pt}$  was measured, which described below. There was however no evidence that anything which would emit more than one proton in the decay of the compound nucleus, like Os, Re, W or Ta was produced. Identifying the Iridium products was a difficult task. Firstly, as the Coulomb-barrier equation... for these reactions is higher than for Ni, Cu and Fe as target nuclei, since the number of protons is higher. Thus we known that reactions like (d, $\alpha$ ), or (d,xp) would not be heavily fed. However, most of the energetic thresholds are less than 33 MeV, so even though they are weakly fed, they will still be fed if the channel is possible. This we did not see any evidence of. Secondly, many of the nuclei have gammas that are so close in energy that

the germanium detectors would identify the peak as one. As the reaction routes producing Ir- and Pt-radionuclides is heavily favoured, the peaks with feeding from multiple nuclei would still mostly be caused by those nuclides. The question is then, was anything else than Ir and Pt radionuclides produced, or were they produced but could not be distinguished because of the peaks. As a summary, a few of the nuclides were excluded, but a few of the nuclides is questionable. It can also be mentioned that the compound nuclei  $^{193}\text{Pt}$  and  $^{195}\text{Pt}$  are nuclei with even Z and odd N, thus proton emission would be more likely, as discussed in section ....

Production routes via  $\alpha$  emission is energetically possible.  $^{191}\text{Ir}(\text{d},\alpha)^{189}\text{Os}$  (stable) with reaction Q-value=12988.8 keV could not be observed since it is a stable product, and  $^{193}(\text{d},\alpha)^{191}\text{Os}$  (ground state  $t_{1/2}=15.4$  d, isomer  $t_{1/2}=13.10$  h) with reaction Q-value 12569.8 keV, was not observed.  $^{191}\text{Os}$  was expected to be produced, as the cumulative cross sections within the deuteron energy region have been observed [cite tarkanyi 2019](#). However measurements done in that work was small cross sections. The main hypothesis for  $^{191}\text{Os}$  not to be observed is that the only gamma-line of the ground state which was intense enough to be observed was 129.431 keV (26.50%) which was too close to  $^{191}\text{Pt}$  ( $t_{1/2}=2.83$  d) in energy. Thus the way to measure the  $^{191}\text{Os}$  cross section was to count long enough for  $^{191}\text{Pt}$  to decay completely, which would be for ten half lives which wold be approximately 1500 hours. The isomer also has one single gamma-line at 74.38 keV (0.0729%), which was not observed due to low intensity, and multiple nuclei with similar gamma-line.  $^{191}\text{Ir}(\text{d},2\alpha)^{185}\text{W}$  ( $t_{1/2}=75.1$  d) with reaction Q-value 14964.9 keV was not observed, nor was  $^{193}\text{Ir}(\text{d},2\alpha)^{187}\text{W}$  ( $t_{1/2}=24.0$  h) with reaction Q-value 13653.6 keV. Thus it was concluded that W and below in mass number was produced at all.

Another reaction route which was expected to be observed was  $^{193}\text{Ir}(\text{d},2\text{p})^{193}\text{Os}$  ( $t_{1/2}=30.11$  h) with reaction Q-value -2584.0 keV. Gamma-lines matched well with the spectra, and unique gamma-lines 321.616 keV (1.245%) and 387.509 keV(1.226%) (which was not in the background) was used to estimate the end of beam activity, the cross sections did not look reasonable. Re-radionuclides had similar gamma-lines to Pt and Ir-radionuclides, so we could not distinguish. No observation of Re-radionuclides were made, but a question-mark remain on this behalf, especially since  $^{190}\text{Re}$  and  $^{192}\text{Re}$  is even (odd-odd).

#### $^{188}\text{Ir}$ (Cumulative and independent)

$^{188}\text{Ir}$  ( $t_{1/2}=41.5$  h) is a radionuclide with one metastable isomer (with a half-life in the order of ms) along with the ground state, which decays by either isomeric transition or  $\epsilon/\beta^+$ , but the branching ratio is not stated. The reported cross sections for  $^{188}\text{Ir}$ , regardless of whether it is reported as cumulative or independent is the cumulative cross section of the ground state and isomer. Since an independent measurement of  $^{188}\text{Pt}$  ( $t_{1/2}=10.2$  d), which feeds into  $^{188}\text{Ir}$  (100%) was obtained, the independent measurement without feeding and the cumulative cross section with feeding is reported. The reaction threshold is  $^{191}\text{Ir}(\text{d},2\text{nt})$  with a reaction Q-value of -16231.0 keV. In this work, we did not see any evidence of this decay-route being fed. Thus,  $^{188}\text{Ir}$  can be produced via  $^{191}\text{Ir}(\text{d},4\text{np})$  with a reaction Q-value -24802.0 keV and an energy threshold of 25064.0 keV. From  $^{193}\text{Ir}$  as target nuclei, the threshold for 6np-particle emission is above energy threshold, so the only available route from this target nucleus is with emission of 4nt (Q-value is -30291.0 keV), which is not heavily fed either. It is clear that the excitation function first increases once the 4np-decay channel opens, but the measured points are at a low cross section value. The gamma-lines which were used are listed in table ..., The end of beam-activity was estimated using a single decay, where activity points ca. 200 hours after end of beam is slightly higher than the curve, because of the feeding. The end of beam activity however looks reasonable, and the cross section also looks reasonable. Comparing the measured cross section points to experimental data, F. Tarkanyi et. al. (2019), does not have any measured points below ca 35 MeV, but the points predicts that the excitation function increases in this region, where the measured cross sections in this work give reason to believe that the cross section increases from about 25 MeV. The independent measurement aligns well with TALYS and TENDL, but the large measurements 26 MeV is probably a little higher than then true value. [reaction models](#).

**$^{189}\text{Ir}$  (Cumulative and independent)**

This is weird. Expectedly, the cumulative cross section of  $^{189}\text{Ir}$  should be larger than the independent measurement of  $^{189}\text{Pt}$ , due to  $\epsilon$ -decay (100%). This is however not the case so the independent measurement of  $^{189}\text{Ir}$  is negative. This is also apparent in Tarkanyi et. al. (2019), so why is this?  $^{189}\text{Ir}$  ( $t_{1/2}=13.2$  d) is a radionuclide with two metastable states with half-lives in order of microseconds. Thus the total cross section in general is the two isomers and the ground state. However,  $^{189}\text{Pt}$  ( $t_{1/2}=10.87$  h) feeds into this radionuclide via  $\beta^+/\epsilon$  (100%), so both an independent measurement of the three states of  $^{189}\text{Ir}$  is reported along with the cumulative cross section with feeding from  $^{189}\text{Pt}$ . The gamma-lines which were used are listed in table ..., and the end of beam activity was estimated using single-step decay, although ideally this could have been fitted using a two-step decay with feeding from  $^{189}\text{Pt}$ , but due to overestimation in the end of beam activity, so it turned out large negative. Instead single-step decay was used where no peaks before 60 hours after end of beam was used, so that the  $^{189}\text{Pt}$  had decayed out.  $^{189}\text{Ir}$  can be produced via  $^{191}\text{Ir}(\text{d},3\text{np})$  with a reaction Q-value -16626.0 keV and energy threshold 16802.0 keV, or via  $^{193}\text{Ir}(\text{d},5\text{np})$  with reaction Q-value -30596.0 keV and energy threshold 30916.0 keV. This work provided four cross section measurements from 23-30 MeV, and it is clear that the cross section increases from ca. 20 MeV, comparing to experimental data from F. Tarkanyi et. al. (2006). The data provided by this work is in well compliance with the 2006 data, where the excitation function is at its highest between 30-35 MeV, when the other reaction channel has opened. However, 2019 data is shifted ca. 10 MeV higher in energy. Our data seems to agree with the 2006 version. The 2019 data seems to be agreeing more with when the excitation function starts to increase looking at ALICE, TENLD and TALYS, where at 20-25 MeV, the function is basically 0.

 **$^{190m1+g}\text{Ir}$  (Cumulative and independent)**

$^{190}\text{Ir}$  ( $t_{1/2}=11.78$  d) decays by  $\epsilon/\beta^+$ -decay to stable  $^{190}\text{Os}$  (100%). This radionuclide can be produced via  $^{191}\text{Ir}(\text{d},2\text{np})$  with a reaction Q-value -1769.3 keV and with an energy threshold 10359.2 keV or via  $^{193}\text{Ir}(\text{d},4\text{np})$  with a reaction Q-value -24221.2 and with an energy threshold 24474.0 keV. For this radionuclide, a total of eight cross section measurements were made in the energy region 13-30 MeV, and as expected, we did not see evidence that this radionuclide was produced for deuterons below 10 MeV. The excitation function steadily increases from 13-20 MeV, and once the next reaction channel opens, the excitation function increases more steeply. Due to the independent measurement of  $^{190m2}\text{Ir}$ , an independent measurement of the ground state and the m1-isomer was made, which is given in figure ... The excitation function looks almost identical due to the weak branching from  $^{190m2}\text{Ir}$  (8.60%), along with quite low measured cross sections of  $^{190m2}\text{Ir}$  (table...). Comment on reaction models.

 **$^{190m2}\text{Ir}$  (Independent)**

$^{190m2}\text{Ir}$  ( $t_{1/2}=3.087$  h) either decay by  $\beta^+/\epsilon$ -decay (91.4%) to  $^{190}\text{Os}$  or isomer transition (8.6%) to  $^{190g}\text{Ir}$ . figure out Q-values and e thresholds

 **$^{192g}\text{Ir}$  (Cumulative)**

$^{192g}\text{Ir}$  ( $t_{1/2}=78.829$  d) either  $\beta^-$  decays to stable  $^{192}\text{Pt}$  (95.24%) or  $\beta^+/\epsilon$ -decays to stable  $^{192}\text{Os}$  (4.76%). The radionuclide can be produced via  $^{191}\text{Ir}(\text{d},\text{p})$  with a reaction Q-value of 3973.55 keV, or via  $^{193}\text{Ir}(\text{d},2\text{np})$  with a reaction Q-value -9996.6 keV, and a energy threshold 10.1009 MeV<sup>1</sup>. Thus the reaction channel is energetically possible for 0 MeV deuterons. However, since there are two possible ways to produce this radionuclide, an increasing cross section would appear as the probability of proton emission as decay channel increases. With a proton Coulomb-barrier at approximately 13 MeV for both stable targets<sup>2</sup>, the first peak in the excitation function should be somewhere around there, which we can clearly see on the figure, in the experimental data in this work. Then the cross section decreases up to about 20 MeV, and increases up to about 35 MeV, where the experimental data suggests that the cross section flattens. This measurement is a cumulative cross section with

<sup>1</sup>(<https://www.nndc.bnl.gov/qcalc/qcalcr.jsp>)

<sup>2</sup>(<http://hyperphysics.phy-astr.gsu.edu/hbase/NucEne/coubar.html>)

$^{192m^1}\text{Ir}$  ( $t_{1/2}=1.45$  m) feeding in with isomer transition (99.98%), and  $^{192m^2}\text{Ir}$  ( $t_{1/2}=241$  y) feeding in with isomer transition (100%), where we did not make any independent measurements of either isomers due to too short and too long half life. We were able to produce and measure the cross section in each foil, and the cross section measurements done in this work is in well compliance with experimental data provided by Tarkanyi et. al. (2006, 2019), but the values are slightly higher for energies higher than 13 MeV. The gamma-lines which were used are listed in table ??, and all the gamma-lines are neither in the background or feeding from other gammas. The end of beam activity was estimated using a single-step decay, as there is nothing beta-feeding in, and the isomers are in the cumulative cross section. **The theoretical predictions are off. Make more comments.**

#### $^{194g}\text{Ir}$ (Cumulative)

The reaction Q-value for  $^{193}\text{Ir}(\text{d},\text{p})^{194g}\text{Ir}$  is 3842.22 keV, thus the energy threshold for the deuteron is 0 MeV. For this particular measurement, the cross section is reported as cumulative because of the  $^{194m^1}\text{Ir}$ -isomer ( $E=147.0785$  keV,  $t_{1/2}=31.85$  ms) feeds into  $^{194g}\text{Ir}$  by isomer transition (100%).  $^{194g}\text{Ir}$  decays by  $\beta^-$  to stable  $^{194}\text{Pt}$ . The gamma-lines which were used to calculate the activity in the foils were 293.541 (2.5%), 300.741 (0.35%), 589.179 (0.140%), 938.69 (0.60%), 1150.75 (0.60%), 1468.91 (0.19%). Most of the gamma-intensities are less than 1%, as more intense gamma-lines were either in the background or had gamma-lines which were overlapping with other nuclei. Thus the contribution to uncertainties can be of importance here. However, comparing the measured cross sections to other measured cross sections by Tarkanyi et. al. (2006, 2019), the uncertainty in cross section looks small. The end of beam activity was estimated using a single step decay, since the parent isomer  $^{194m^2}\text{Ir}$  does not feed (decay by  $\beta^-$  (100%)), and there is no chance that we can measure the  $^{194m^1}\text{Ir}$  isomer. The correspondence between the previous experimental data seems to be good. The measured points in this work seems to be a little on the high side on the tail, but yet within uncertainty. TENDL and TALYS does an ok job shaping the peak, but is both lower in magnitude and the maximum of the TENDL function shifted from about 13 to 10 MeV. The maximum of of the TALYS peak is in better compliance with the measured cross sections, and suggests a maximum at around 12 MeV. ALICE however is on **baertur**

#### $^{194m^2}\text{Ir}$ (Independent)

The reaction Q value for  $^{193}\text{Ir}(\text{d},\text{p})^{194m^2}\text{Ir}$  ( $t_{1/2}=171$  d) is 3652.22-X keV, due to the uncertain energy level of the isomer. Having a positive reaction Q-value, the deuteron energy threshold is 0 MeV. The cross section represented in this work is independent, as this isomer level is the highest one observed.  $^{194m^2}\text{Ir}$  decays by  $\beta^-$ -decay to stable  $^{194}\text{Pt}$ . In the estimation of cross section, one single line was used, which was 390.8 keV (35%). The more intense gamma-lines such as 482.6 keV (97%), 328.5 (93%) snf 600.5 (62%) were not used due to weak feeding from other nuclei, or being present in the background spectra. Thus, the total number of measured points are only five in the energy region 16-26 MeV, since stronger gamma-lines were excluded in the activity calculations. The end of beam activity was estimated using a one-step decay chain. The measurement of the reaction cross section for this nucleus is in well compliance with the results published by F. Tarkanyi et. al. (2006, 2019), magnitude wise (a little on the high side, but within uncertainty). There is however difficult to see if there is any clear curve shape of the excitation function, as especially the datapoints from F. Tarkanyi et. al. (2006) seems to have a high variation in the cross section values. The datapoints from F. Tarkanyi et. al. (2019) seems to be more systematic, along with smaller energy bins. The measured datapoints in this work suggests that the cross section increases with beam energy at least up to 26 MeV, which seems to be the general tendency for F. Tarkanyi et. al. (2019), without a few exceptions where the measured cross section decreases. Since this isomer only can be produced in one particular way, the expected shape of the excitation function is one global maximum, which should be shifted towards the low energy side due to the low energy threshold. There is no TALYS, TENDL or ALICE reaction code-data for this specific isomer (per april 2020), so it is difficult to determine the exact shape of the excitation function. With as long half-life as this isomer has, the foil should have been counted over a longer timeperiod after end of beam. Then multiple other gamma-lines could have

been used to measure the end of beam activity, by excluding the timepoints where multiple nuclei feeds the same gamma-energy.

#### $^{188}\text{Pt}$ (Independent)

$^{188}\text{Pt}$  ( $t_{1/2}=10.2$  d),  $\epsilon/\beta^+$ -decay to  $^{188}\text{Ir}$  (100%).  $^{191}\text{Ir}(\text{d},5\text{n})$  with a reaction Q-value -26109.0 keV and an energy threshold 26384.0 keV.  $^{193}\text{Ir}(\text{d},7\text{n})$  is not possible in this deuteron energy range under 40 MeV. Thus as expected, the measured cross sections are three points in the energy range 26-30 MeV, and the points are in the threshold region, which is in compliance with both talys and tendl. The experimental data done by T. Tarkanyi et. al. (2006, 2019) have not measured any cross sections below 32 MeV, but the measured points supports that the threshold should be close to where we measured the first points, and then the excitation function increases for this specific reaction route. The gamma-lines that were used are listed in table ..., and the end of beam activity was found via single-step decay. Around the threshold, ALICE, TALYS and TENDL agrees with the measured data.

#### $^{189}\text{Pt}$ (Independent)

$^{189}\text{Pt}$  ( $t_{1/2}=10.8$  h) decays by  $\epsilon/\beta^+$ -decay to  $^{189}\text{Ir}$  (100%). This radionuclide can be produced via  $^{191}\text{Ir}(\text{d},4\text{n})$  with a reaction Q-value -19389.0 keV and energy threshold 19593.0 keV, or via  $^{193}\text{Ir}(\text{d},6\text{n})$  with reaction Q-value -33359.0 keV and energy threshold 33707.0 keV. The measured cross sections suggest a energy threshold around 19 MeV, but the threshold of 19.5 MeV is within uncertainty in energy. Talys and Tendl suggests threshold 19.8 MeV. It seems like there is some disagreement on where the excitation function peak should be in the 30-35 MeV region, where in general, datapoints provided by this measurement suggests a higher cross sections shifted to slightly lower energies than experimental data by F. Tarkanyi et. al. (2006, 2019). It is also hard to say whether the next point would have been higher in cross section, if we could have measured that, but if not, TENDL and TALYS supports this curve shape. The 2006 data also suggests a lower but broader cross section peak, than the 2019 data. From TALYS and TENDL, it seems like the cross section is increasing from 37 MeV, where the 6n decay channel opens. The gamma-lines used are listed in table .., and to estimate the end of beam activity, the decay curve was estimated using a single-step decay.

#### $^{191}\text{Pt}$ (Independent)

$^{191}\text{Pt}$  ( $t_{1/2}=2.83$  d) decays by  $\epsilon/\beta^+$ -decay to stable  $^{191}\text{Ir}$  (100%). This radionuclide can be produced via  $^{191}\text{Ir}(\text{d},2\text{n})$  with a reaction Q-value -4017.0 keV and an energy threshold 4060.0 keV, or via  $^{193}\text{Ir}(\text{d},4\text{n})$  with a reaction Q-value -17988.0 keV and an energy threshold 18175.0 keV. In this work, ten independent measurements were made for this product nucleus, and the first one is right above energy-threshold at ca. 5.5 MeV, and the two peaks in the cross section matches the different reaction channels which opens at ca 4 MeV and 18 MeV. The measured data in this work matches the experimental data from F. Tarkanyi et. al (2016, 2019). The end of beam activity was estimated using a single step decay. **REMEMBER that when above threshold, all reactions can happen. And even though for instance d,n is not favoured at higher energies, it can still happen, and thus the second peak may look higher.**

#### $^{193m}\text{Pt}$ (Independent)

$^{193m}\text{Pt}$  ( $t_{1/2}=4.33$  d) decays by isomeric transition to long-lived  $^{193}\text{Pt}$  (100%). The isomer can be produced via  $^{193}\text{Ir}(\text{d},2\text{n})$  with a reaction Q-value -3063.5 keV and energy threshold 3095.5 keV. Made 10 independent measurements for this reaction. Comparing to experimental data, the result look reasonable. Talys and tendl peak seems to be shifted toward higher energies, while ALICE seems reasonable position wise, suggesting a excitation function maximum at ca. 12 MeV, which matches the experimental data well. However, for higher energies ALICE looks strange. Due to the weak intensity of the gamma-line provided by the IT decay, we had to use X-rays to be sure that we got the right cross section. However due to many X-rays being fed only 66.831 keV was used. Since

66.831 keV is also an X-ray present in  $^{192}\text{Ir}$  ( $t_{1/2}=73.829$  d) (intensity is 4.44%), this X-ray was used to obtain the  $^{193m}\text{Pt}$  activities. Single-step decay was used to obtain end of beam activity.

#### $^{52}\text{Mn}$ (Cumulative)

$^{52}\text{Mn}$  ( $t_{1/2} = 5.591$  d) (figure ??) is reported as a cumulative cross section, because of the unidentified decay rate of  $^{52m}\text{Mn}$  ( $t_{1/2} = 21.1$  m). The isomer and ground state share multiple lines, and using the values after the isomer was decayed completely ( $\simeq 5\text{ hours} = 10$  half lives after end of beam), the activities were fitted to a single step decay. Hence the cross section is cumulative. From table ??, the Q-value<sup>3</sup> in which  $^{52}\text{Mn}$  can be produced is -1235.6 keV, so the threshold is well within the energy range in which this work is operating in. As we can see in figure figure, the first observation is approximately at 14 MeV. The Coulomb barrier for the compound nucleus  $^{58}\text{Ni}(d)^{58*}\text{Cu}$ , the height is 12.7509 MeV, thus the chance of tunneling before that energy is relatively low. Once the reaction channel from  $^{60}\text{Ni}$  (with a Q value of -21622.6 keV), the increase in cross section is visible. The gammaslines which were used are strong, and as a consequence, the uncertainties in the cross section is relatively small.

$^{52}\text{Mn}$  is an odd-odd nucleus with 25 protons and 27 neutrons. Both proton and a neutron is unpaired, so this decay channel is not necessarily favoured as a d,pn, d,3p3n etc.

#### $^{54}\text{Mn}$ (Independent)

$^{54}\text{Mn}$  ( $t_{1/2} = 312.20$  d) is an independent measurement of the cross section. There are multiple measurements at low cross section values. The (d,2 $\alpha$ ) reaction channel is available at most energies, but the Coulomb barrier is which is at 12.7509 MeV, suggests that the probability of tunneling is relatively low below 10 MeV. The cross section first starts rising at around 18-20 MeV, where multiple reaction channels opens. In general, the measured cross sections done in this thesis matches the earlier experimental data within uncertainties, allthough a little on the high side in the low energy region.

#### $^{59}\text{Fe}$ (Independent)

There is no experimental data in this reaction, however the measured cross section data points agree well with talys. Tendl apparently has a harder time to find a good cross section model. This is not a strongly fed channel, first of all this is an even-odd nucleus with 26 protons and 33 neutrons, leaving one unpaired neutron. If we interpret the cross section correctly, the cross section starts to increase around when overcoming the coulomb barrier, and keeps increasing while other reaction channel opens.

#### $^{55}\text{Co}$ (Independent)

Agrees very well with other experimental data. Z=27, N=28. Cs not super high.

#### $^{60}\text{Co}$ (Independent)

Tendl looks off, however talys follows the experimental data pretty well. As we can see the experimental data is spread in the high energy region, and it is hard to say if actually have made good values. However we are well above energy threshold.

#### $^{56}\text{Ni}$ (Independent)

The only way  $^{56}\text{Ni}$  can be produced is via  $^{58}\text{Ni}$ . The threshold is

---

<sup>3</sup>Calculating the Q value for various reactions: <http://hyperphysics.phy-astr.gsu.edu/hbase/NucEne/coubar.html>

The cross sections for the iridium products are listed in table .... Give a brief discussion on the various products. And also, give a discussion of what we expected and what we did not see. THIS IS NOT A FINAL VERSION In this experiment,  $^{188}\text{Pt}$ ,  $^{189}\text{Pt}$ ,  $^{191}\text{Pt}$ ,  $^{193m}\text{Pt}$ ,  $^{188}\text{Ir}$ ,  $^{189}\text{Ir}$ ,  $^{190}\text{Ir}$ ,  $^{192}\text{Ir}$ ,  $^{194}\text{Ir}$ ,  $^{194m2}\text{Ir}$ ,  $^{188}\text{Re}$ ,  $^{189}\text{Re}$  and  $^{190}\text{Re}$  was observed. The products we did not observe was  $^{183}\text{Ta}$  ( $t_{1/2}=5.1$  d),  $^{186}\text{Re}$  ( $t_{1/2}=3.7186$  d),  $^{186}\text{Ta}$  ( $t_{1/2}=10.5$  m),  $^{18}\text{W}$  ( $t_{1/2}=24.0$  h).

$^{183}\text{Ta}$  has a Q-value equal to 0.0 MeV for  $^{191}\text{Ir}(\text{d},\text{d}\alpha)^{183}\text{Ta}$  and 4.020 MeV for  $^{193}\text{Ir}(\text{d},\text{n}t2\alpha)^{183}\text{Ta}$ . The strongest gamma-line ( $E_\gamma = 59.318$  keV,  $I_\gamma = 42.1\%$ ) was not observed in any spectrum, and the second strongest gamma-line ( $E_\gamma = 246.059$  keV,  $I_\gamma = 27.2\%$ ) is within 1 keV from a gamma-line belonging to  $^{189}\text{Ir}$  ( $E_\gamma = 245.1$  keV,  $I_\gamma = 6.0\%$ ). Hence, we conclude that  $^{183}\text{Ta}$  was not observed.

$^{186}\text{Re}$  has a Q-value equal to 0.0 MeV for  $^{191}\text{Ir}(\text{d},\text{t}\alpha)^{186}\text{Re}$  and 13.1264 MeV for  $^{193}\text{Ir}(\text{d},\text{2n}\alpha)^{183}\text{Ta}$ . There is no data in the EXFOR database, and the reaction modelled cross sections provided by TALYS predicts that the cross section is **very low or zero** in this energy range. The two strongest gamma-lines were observed, ( $E_\gamma = 122.64$  keV,  $I_\gamma = 0.603\%$ ,  $E_\gamma = 137.157$  keV,  $I_\gamma = 9.47\%$ ). However, the activity which was estimated was not looking natural, hence the cross section curve is difficult to interpret **Might need some more work**.



# Appendix A

## Statistics

Uncertainty in statistics refers to the standard deviation of the data, which gives a number of the spreading of the data from the mean value of the data citation. The variance is the standard deviation squared, which weights the variables to a higher degree.

$$std = \sqrt{\sigma^2} \quad (\text{A.1})$$

$$\sigma = \sqrt{\frac{1}{N} \sum_{i=1}^N (x_i - \bar{x})^2} \quad (\text{A.2})$$

where N is the number of measurements,  $x_i$  is a measurement and  $\bar{x}$  is the average over all measurements.

$\chi^2$  is an estimation of the goodness of the fit, which includes the weight of the error

$$\chi^2 = \sum_i^n \left( \frac{y_i - \bar{y}}{\sigma_i} \right)^2 \quad (\text{A.3})$$

where  $\bar{y}$  is the mean value of y and  $\sigma_i$  is the error in  $y_i$ . The reduced  $\chi^2$  is defined as the  $\chi^2$  per degree of freedom

$$\chi_\nu^2 = \frac{\chi^2}{\nu} \quad (\text{A.4})$$

where  $\nu$  is the degrees of freedom equal to the number of observations minus the number of fitted parameters. A value close to  $\chi_\nu^2 = 1$  indicates that the observations and fit is in well accordance to the error, while  $\chi_\nu^2 > 1$  indicates an underfitting and a  $\chi_\nu^2 < 1$  indicates an overfitting<sup>1</sup>.

A function  $f$  with input  $x$  and a set of variables  $\vec{\beta} = \beta_1, \beta_2, \dots, \beta_n$  and output y can be written on the following form

$$y = f(x, \vec{\beta}) \quad (\text{A.5})$$

The uncertainty in y is dependent on the uncertainty in the different input variables  $\vec{\beta}$ . The matrix expression for error propagation is (Tellinghuisen, Joel, Statistical error propagation)<sup>2</sup>

$$\sigma_y^2 = \mathbf{J} \cdot \mathbf{V} \cdot \mathbf{J}^T \quad (\text{A.6})$$

where  $\sigma_y^2$  is the variance in y, J is the Jacobian matrix

$$\mathbf{J} = \begin{bmatrix} \frac{\partial f}{\partial \beta_1} & \frac{\partial f}{\partial \beta_2} & \dots & \frac{\partial f}{\partial \beta_n} \end{bmatrix} \quad (\text{A.7})$$

and V is the variance-covariance matrix

---

<sup>1</sup>[https://en.wikipedia.org/wiki/Reduced\\_chi-squared\\_statistic](https://en.wikipedia.org/wiki/Reduced_chi-squared_statistic)

<sup>2</sup>A full derivation of the expression can be found in Uncertainty Propagation for Measurements with multiple output quantities, Dobbert, Schrijver

$$\mathbf{V} = \begin{bmatrix} \sigma_0^2 & \sigma_{0,1} & \cdots & \sigma_{0,n} \\ \sigma_{1,0} & \sigma_1^2 & \cdots & \sigma_{1,n} \\ \vdots & \vdots & \ddots & \vdots \\ \sigma_{n,0} & \sigma_{n,1} & \cdots & \sigma_n^2 \end{bmatrix} \quad (\text{A.8})$$

In the cases where the input parameters are uncorrelated, all non-diagonal elements in the variance-covariance matrix is equal to zero, and the expression for the variance is simplified to

$$\sigma_y^2 = \sum_{i=1}^n \left( \frac{\partial f}{\partial \beta_i} \right)^2 \sigma_{\beta_i}^2 \quad (\text{A.9})$$

Whenever the input parameters are correlated, which means that  $\sigma_{\beta_i, \beta_j} \neq 0$ , we have to apply equation A.6, otherwise, the simplification in equation A.9 will give wrong error propagation.

To evaluate the partial derivatives of  $f$ , the computational derivation is applicable

$$\frac{\partial f}{\partial \beta_i} \approx \frac{f(x, \beta_i + \frac{\Delta \beta_i}{2}) - f(x, \beta_i - \frac{\Delta \beta_i}{2})}{\Delta \beta_i} \quad (\text{A.10})$$

where  $\Delta \beta_i$  is a small number, like  $10^{-8} \beta_i$ .

For a function  $f = xy$ , the variance can be expressed from equation A.6, where

$$\mathbf{J} = [y \quad x]$$

and

$$\mathbf{V} = \begin{bmatrix} \sigma_x^2 & \sigma_{x,y} \\ \sigma_{y,x} & \sigma_y^2 \end{bmatrix}$$

$$\sigma_f^2 = x^2 \sigma_y^2 + y^2 \sigma_x^2 + 2xy \sigma_{x,y} \quad (\text{A.11})$$

If we multiply each term so that we can collect  $f^2$  in the numerator, the variance in  $f$  can be expressed as

$$\sigma_f^2 = f^2 \left( \frac{\sigma_x^2}{x^2} + \frac{\sigma_y^2}{y^2} + \frac{2\sigma_{x,y}}{xy} \right) \quad (\text{A.12})$$

if the variables  $x$  and  $y$  are uncorrelated, the variance is further simplified, and more terms can be included easily. The simplified standard deviation of a function  $f(\bar{\beta}) = \beta_1 \cdot \beta_2 \cdots \beta_n$  with uncorrelated variables is thus

$$\sigma_f = |f| \sqrt{\left( \frac{\sigma_{\beta_1}}{\beta_1} \right)^2 + \left( \frac{\sigma_{\beta_2}}{\beta_2} \right)^2 + \cdots + \left( \frac{\sigma_{\beta_n}}{\beta_n} \right)^2} \quad (\text{A.13})$$

## Appendix B

## Tables

For all tables, the assumption is that the main particle emission is due to alpha, proton or neutron emission. However, triton,  $^3\text{He}$  and deuterons are still fed when above threshold, but from theory, the feeding is low. For triton,  $^3\text{He}$  and deuteron respectively, subtract 8.5, 7.7 or 2.2 respectively from the Q value. Alphaparticles (due to the large binding energy and spin equal to 0) will be more fed. To calculate Q value for alpha emission subtract 28.3 MeV from Q value of 2p2n-reactions. Q values from <sup>1</sup> are used. Q values below 40 MeV are included for comparison to experimental data.

## B.1 Product nuclei, Q-values and gammarays

Table B.1: Products observed on Nickel foils. Nickel has five stable isotopes:  $^{58}\text{Ni}$  (68.077%),  $^{60}\text{Ni}$  (26.223 %),  $^{61}\text{Ni}$  (1.1399%),  $^{62}\text{Ni}$  (3.6346%) and  $^{64}\text{Ni}$  (0.9255%). If the nucleus has provided energy level, the nucleus is an isomer, if nothing then ground state. The table is inspired by Tarkanyi et al 2019 (ir paper))

Nuclide level (keV)	Half life	Decay mode	Reaction route	Q value (keV)	$E_{\gamma}$ (keV)	$I_{\gamma}$ (%)
$^{52}\text{Mn}$ (0.0)	5.591 d 21.1 m	$\epsilon$ : 100%	$^{58}\text{Ni}(\text{d},2\alpha)$ $^{60}\text{Ni}(\text{d},2\text{n}2\alpha)$ $^{61}\text{Ni}(\text{d},3\text{n}2\alpha)$	-1235.6 -21622.6 -29442.7	744.233 935.544 1246.278 1434.092	90.0 94.5 4.21 100.0
$^{54}\text{Mn}$ (0.0)	312.20 d	$\epsilon$ : 100%	$^{58}\text{Ni}(\text{d},2\text{p}\alpha)$ $^{60}\text{Ni}(\text{d},2\alpha)$ $^{61}\text{Ni}(\text{d},\text{n}2\alpha)$ $^{62}\text{Ni}(\text{d},2\text{n}2\alpha)$	-8538.3 -629.6 -8449.7 -19045.4	834.848	99.9760
$^{59}\text{Fe}$ (0.0)	44.490 d	$\beta^-$ : 100%	$^{60}\text{Ni}(\text{d},3\text{p})$ $^{61}\text{Ni}(\text{d},\text{n}3\text{p})$ $^{62}\text{Ni}(\text{d},\text{p}\alpha)$ $^{64}\text{Ni}(\text{d},2\text{n}\text{p}\alpha)$	-12539.5 -20359.6 -2659.7 -19154.9	1291.590	43.2
$^{55}\text{Co}$ (0.0)	17.53 h	$\epsilon$ : 100%	$^{58}\text{Ni}(\text{d},\text{n}\alpha)$ $^{60}\text{Ni}(\text{d},3\text{n}\alpha)$ $^{61}\text{Ni}(\text{d},4\text{n}\alpha)$	-3559.4 -23946.4 -31766.5	385.4 520.0 803.7 931.1 1212.8 1316.6 1370.0 2177.6	0.54 0.83 1.87 75 0.26 7.1 2.9 0.29

<sup>1</sup><https://www.nndc.bnl.gov/qcalc/>

## APPENDIX B. TABLES

$^{56}\text{Co}$ (0.0)	77.236 d	$\epsilon : 100\%$	$^{58}\text{Ni}(\text{d},\alpha)$ $^{61}\text{Ni}(\text{d},2\text{n}\alpha)$ $^{61}\text{Ni}(\text{d},3\text{n}\alpha)$ $^{62}\text{Ni}(\text{d},4\text{n}\alpha)$	6522.5 -13864.5 -21684.6 -32280.4	787.743 846.770 977.372 1175.101 1963.741 2015.215 2034.791	0.3111 99.9399 1.421 2.252 0.707 3.016 7.77
$^{57}\text{Co}$ (0.0)	271.74 d	$\epsilon : 100\%$	$^{58}\text{Ni}(\text{d},\text{n}2\text{p})$ $^{60}\text{Ni}(\text{d},\text{n}\alpha)$ $^{61}\text{Ni}(\text{d},2\text{n}\alpha)$ $^{62}\text{Ni}(\text{d},3\text{n}\alpha)$	-10396.7 -2488.1 -10308.2 -20903.9	122.06065 136.47365	85.60 10.68
$^{58}\text{Co}$ (0.0)	70.86 d	$\epsilon : 100\%$	$^{58}\text{Ni}(\text{d},2\text{n})$ $^{60}\text{Ni}(\text{d},\alpha)$ $^{61}\text{Ni}(\text{d},\text{n}\alpha)$ $^{62}\text{Ni}(\text{d},2\text{n}\alpha)$ $^{64}\text{Ni}(\text{d},4\text{n}\alpha)$	-1823.8 6084.9 -1735.3 -12331.0 -28826.2	810.7593 863.951 1674.725	99.450 0.686 0.517
$^{58m}\text{Co}$ (24.88921)	9.10 h	IT:100%	$^{58}\text{Ni}(\text{d},2\text{n})$ $^{60}\text{Ni}(\text{d},\alpha)$ $^{61}\text{Ni}(\text{d},\text{n}\alpha)$ $^{62}\text{Ni}(\text{d},2\text{n}\alpha)$ $^{64}\text{Ni}(\text{d},4\text{n}\alpha)$	-1848.7 6060.0 -1760.2 -12355.9 -28851.1	-	-
$^{60}\text{Co}$ (0.0)	1925.28 d	$\beta^- : 100\%$	$^{60}\text{Ni}(\text{d},2\text{p})$ $^{61}\text{Ni}(\text{d},\text{n}2\text{p})$ $^{62}\text{Ni}(\text{d},\alpha)$ $^{64}\text{Ni}(\text{d},2\text{n}\alpha)$	-4265.0 -12085.1 5614.8 -10880.4	1173.228 1332.492	99.85 99.9826
$^{56}\text{Ni}$ (0.0)	6.075 d	$\epsilon : 100\%$	$^{58}\text{Ni}(\text{d},3\text{np})$	-24688.4	158.38 480.44 749.95 811.85 1561.80	98.8 36.5 49.5 86.0 14.0
$^{57}\text{Ni}$ (0.0)	35.60 h	$\beta^+ : 100\%$	$^{58}\text{Ni}(\text{d},2\text{np})$ $^{60}\text{Ni}(\text{d},4\text{np})$	-14440.8 -34827.8	1757.55 1919.52 2804.20	5.75 12.3 0.098
$^{65}\text{Ni}$ (0.0)	2.51719 h	$\beta^- : 100\%$	$^{64}\text{Ni}(\text{d},\text{p})$	3873.51	366.27 1481.84 1623.42 1724.92	4.81 23.59 0.498 0.399
$^{60}\text{Cu}$ (0.0)	23.7 m	$\epsilon : 100\%$	$^{60}\text{Ni}(\text{d},2\text{n})$ $^{61}\text{Ni}(2,3\text{n})$ $^{62}\text{Ni}(\text{d},4\text{n})$	-9134.9 -16955.0 -27550.7	467.3 497.9 643.2 952.4 1035.2 1110.5 1293.7 1791.6 1861.6 1936.9 2061.0 2158.9 2403.3 2687.9 2746.1	3.52 1.67 0.97 2.73 3.70 1.06 1.85 45.4 4.8 2.20 0.79 3.34 0.77 0.44 1.06

<sup>61</sup> Cu	3.339 h	$\epsilon : 100\%$	<sup>60</sup> Ni(d,n)	2575.3	282.956	12.2
			<sup>61</sup> Ni(d,2n)	-5244.8	373.050	2.1
			<sup>62</sup> Ni(d,3n)	-15840.5	529.169	0.38
			<sup>64</sup> Ni(d,5n)	-32335.7	588.605	1.17
					625.605	0.040
					656.008	10.8
					816.692	0.31
					841.211	0.21
					902.294	0.083
					1032.162	0.043
					1073.465	0.033
					1132.351	0.090
					1185.234	3.7
					1446.492	0.045
<sup>64</sup> Cu	12.701 h	$\epsilon : 100\%$	<sup>64</sup> Ni(d,2n)	-4681.3	1345.77	0.475
		$\beta^- : 38.5\%$				

APPENDIX B. TABLES

---

Table B.2: Products observed on Iron foils. Iron has five stable isotopes:  $^{54}\text{Fe}$  (5.845%),  $^{56}\text{Fe}$  (91.754 %),  $^{57}\text{Fe}$  (2.119%) and  $^{58}\text{Fe}$  (0.282%). If the nucleus has provided energy level, the nucleus is an isomer, if nothing then ground state. **The table is inspired by Tarkanyi et al 2019 (ir paper)**

Nuclide level (keV)	Half life	Decay mode	Reaction route	Q value (keV)	$E_\gamma$ (keV)	$I_\gamma$ (%)
$^{48}\text{V}$ (0.0)	15.9735 d	$\epsilon : 100\%$	$^{54}\text{Fe}(\text{d},2\alpha)$	-3490.9	944.130	7.870
			$^{56}\text{Fe}(\text{d},2\text{n}2\alpha)$	-23986.1	983.525	99.98
			$^{57}\text{Fe}(\text{d},3\text{n}2\alpha)$		1312.106	98.2
$^{51}\text{Cr}$ (0.0)	27.704 d	$\epsilon : 100\%$	$^{54}\text{Fe}(\text{d},\text{p}\alpha)$	-1381.3	320.0824	9.910
			$^{56}\text{Fe}(\text{d},2\text{n}\alpha)$	-21876.5		
			$^{57}\text{Fe}(\text{d},3\text{n}\alpha)$	-29522.6		
			$^{58}\text{Fe}(\text{d},4\text{n}\alpha)$	-39567.2		
$^{52}\text{Mn}$ (0.0)	5.591 d d	$\epsilon : 100\%$	$^{54}\text{Fe}(\text{d},\alpha)$	5163.6	346.02	0.980
			$^{56}\text{Fe}(\text{d},2\text{n}\alpha)$	-15331.6	744.233	90.0
			$^{57}\text{Fe}(\text{d},3\text{n}\alpha)$	-22977.7	848.18	3.32
					935.544	94.5
					1246.278	4.21
					1333.649	5.07
					1434.092	100.0
$^{54}\text{Mn}$ (0.0)	312.20 d	$\epsilon : 100\%$	$^{54}\text{Fe}(\text{d},2\text{p})$	-2139.1	834.8480	99.9760
			$^{56}\text{Fe}(\text{d},\alpha)$	5661.4		
			$^{57}\text{Fe}(\text{d},\text{n}\alpha)$	-1984.7		
			$^{58}\text{Fe}(\text{d},2\text{n}\alpha)$	-12029.3		
$^{53}\text{Fe}$ (0.0)	8.51 m ????	$\epsilon : 100\%$	$^{54}\text{Fe}(\text{d},2\text{np})$	-15602.9	377.9	42%
			$^{56}\text{Fe}(\text{d},4\text{np})$	-36098.1		
$^{59}\text{Fe}$ (0.0)	44.490 d	$\beta^- : 100\%$	$^{58}\text{Fe}(\text{d},\text{p})$	4356.44	1099.245	56.5
					1291.590	43.2
$^{55}\text{Co}$ (0.0)	17.53 h	$\epsilon : 100\%$	$^{54}\text{Fe}(\text{d},\text{n})$	2839.8	91.9	1.16
			$^{56}\text{Fe}(\text{d},3\text{n})$	-17655.4	477.2	20.2
			$^{57}\text{Fe}(\text{d},4\text{n})$	-25301.5	803.7	1.87
					827.0	0.21
					931.1	75
					1316.6	7.1
					1370.0	2.9
					1408.5	16.9
					2177.6	0.29
					2872.4	0.118
					2938.9	0.057

<sup>56</sup> Co (0.0)	77.236 d	$\epsilon : 100\%$	<sup>56</sup> Fe(d,2n) <sup>57</sup> Fe(d,3n) <sup>58</sup> Fe(d,4n)	-7573 -15219.7 -25264.3	263.434 486.55 733.514 787.743 846.770 852.732 896.510 977.372 996.948 1037.843 1140.368 1159.944 1175.101 1198.888 1238.288 1335.40 1360.212 1771.357 1963.741 2015.215 2034.791 2212.944 2276.131 2598.500	0.0220 0.0540 0.191 0.311 99.9399 0.049 0.073 1.421 0.111 14.05 0.132 0.094 2.252 0.049 66.46 0.1224 4.283 15.41 0.707 3.016 7.77 0.388 0.118 16.97
<sup>57</sup> Co (0.0)	271.74 d	$\epsilon : 100\%$	<sup>56</sup> Fe(d,n) <sup>57</sup> Fe(d,2n) <sup>58</sup> Fe(d,3n)	3802.9 -3843.2 -13887.8	122.06065 136.47356	85.60 10.68
<sup>58</sup> Co (0.0)	70.86	$\epsilon : 100\%$	<sup>57</sup> Fe(d,n) <sup>58</sup> Fe(d,2n)	4729.7 -5314.9	810.7593	99.450

APPENDIX B. TABLES

---

Table B.3: Products observed on Copper foils. Copper has two stable isotopes:  $^{63}\text{Cu}$  (69.15%) and  $^{65}\text{Cu}$  (30.85 %). If the nucleus has provided energy level, the nucleus is an isomer, if nothing then ground state. **The table is inspired by Tarkanyi et al 2019 (in paper)**

Nuclide level (keV)	Half life	Decay mode	Reaction route	Q value (keV)	$E_{\gamma}$ (keV)	$I_{\gamma}$ (%)
$^{59}\text{Fe}$ (0.0)	44.490 d	$\beta^-$ : 100%	$^{63}\text{Cu}(\text{d},2\text{p}\alpha)$	-8782.1	1099.245	56.5
			$^{65}\text{Cu}(\text{d},2\alpha)$	1687.0	1291.590	43.2
$^{60}\text{Co}$ (0.0)	1925.28 d	$\beta^-$ : 100%	$^{63}\text{Cu}(\text{d},\text{p}\alpha)$	-507.6	1173.228	99.85
			$^{65}\text{Cu}(\text{d},2\text{n}\alpha)$	-18334.1	1332.492	99.9826
$^{61}\text{Co}$ (0.0)	1.649 h	$\beta^-$ : 100%	$^{63}\text{Cu}(\text{d},\text{n}3\text{p})$	-19484.2	67.412	84.7
			$^{65}\text{Cu}(\text{d},\text{n}p\alpha)$	-9015.1		
$^{65}\text{Ni}$ (0.0)	2.51719 h	$\beta^-$ : 100%	$^{65}\text{Cu}(\text{d},2\text{p})$	-3580.2	1481.84	23.59
			$^{63}\text{Cu}(\text{d},3\text{np})$	-21962.9	282.956	12.2
$^{61}\text{Cu}$ (0.0)	3.339 h	$\epsilon$ : 100% $\beta^-$ : 38.5	$^{65}\text{Cu}(\text{d},5\text{np})$	-39789.4	656.008	10.8
			$^{63}\text{Cu}(\text{d},\text{p})$	5691.54	1185.234	3.7
$^{64}\text{Cu}$ (0.0)	12.701 h	$\epsilon$ : 61.5% $\beta^-$ : 38.5	$^{65}\text{Cu}(\text{d},2\text{np})$	-12135.0	1345.77	0.475
			$^{63}\text{Zn}(\text{d},3\text{n})$	-15490.0	40.85	25.5
$^{62}\text{Zn}$ (0.0)	9.193 h	$\epsilon$ : 100%	$^{65}\text{Cu}(\text{d},5\text{n})$	-33316.6	243.36	2.52
					246.95	1.90
					260.43	1.35
					304.88	0.29
					394.03	2.24
					548.35	15.3
					596.56	26.0
$^{63}\text{Zn}$ (0.0)	38.47 m	$\epsilon$ : 100%			637.41	0.25
			$^{63}\text{Cu}(\text{d},2\text{n})$	-6373.3	449.93	0.236
			$^{65}\text{Cu}(\text{d},4\text{n})$	-24199.8	669.62	8.2
$^{65}\text{Zn}$ (0.0)	243.93 d	$\epsilon$ : 100%			962.06	6.5
			$^{65}\text{Cu}(\text{d},2\text{n})$	-4358.6	1115.539	50.04

Table B.4: Products observed in Iridium foils. Iridium has two stable isotopes:  $^{191}\text{Ir}$  (37.3%) and  $^{93}\text{Ir}$  (62.7 %). If the nucleus has provided energy level, the nucleus is an isomer, if nothing then ground state. **The table is inspired by Tarkanyi et al 2019 (ir paper)**

Nuclide level (keV)	Half life	Decay mode	Reaction route	Q value (keV)	$E_{\gamma}$ (keV)	$I_{\gamma}$ (%)
$^{188}\text{Ir}$ (0.0)	41.5 h	$\epsilon$ : 100%	$^{191}\text{Ir}(\text{d},4\text{np})$	-24802.0	1209.80	6.9
					1715.67	6.2
					2059.65	7.0
$^{189}\text{Ir}$ (0.0)	13.2 d	$\epsilon$ : 100%	$^{191}\text{Ir}(\text{d},4\text{np})$	-16626.0	95.23	0.38
					216.7	0.52
			$^{193}\text{Ir}(\text{d},5\text{np})$	-30596.0	233.5	0.30
					245.1	6.0
$^{190}\text{Ir}$ (0.0)	11.78 d	$\epsilon$ : 100%	$^{191}\text{Ir}(\text{d},2\text{np})$	-10251.1	294.75	6.6
					380.03	2.03
			$^{193}\text{Ir}(\text{d},4\text{np})$	-24221.2	1036.05	2.42
$^{190m^2}\text{Ir}$ (376.4)	3.087 h	IT:8.6% $\epsilon$ : 91.4%	..	..	361.2	86.72
					502.5	89.38
					616.5	90.14
$^{192}\text{Ir}$ (0.0)	73.829 d	$\epsilon$ : 4.76% $\beta^-$ : 95.24%	$^{191}\text{Ir}(\text{d},\text{p})$	3973.55	201.3112	0.471
					295.95650	28.71
			$^{193}\text{Ir}(\text{d},2\text{np})$	-9996.6	374.4852	0.727
					416.4688	0.670
					468.06885	47.84
					489.06	0.438
					612.46215	5.34
					1061.49	0.0531
			$^{194}\text{Ir}(\text{d},\text{p})$	3842.22	293.541	2.5
					300.741	0.35
					589.179	0.140
					938.69	0.60
					1150.75	0.60
					1468.91	0.19
$^{194m^2}\text{Ir}$ (190+X)	171 d	$\beta^-$ : 100%	..	..	338.8	55
					482.6	97
					562.4	35
					687.8	3.6
$^{188}\text{Pt}$ (0.0)	10.16 d	$\epsilon$ : 99.999974% $\alpha$ : $2.6E - 5\%$	$^{191}\text{Pt}(\text{d},2\text{n})$	-26109.0	195.05	18.4
					381.43	7.4
$^{189}\text{Pt}$ (0.0)	10.87 h	$\epsilon$ : 100%	$^{191}\text{Ir}(\text{d},4\text{n})$	-19389.0	94.34	6.5
					113.82	2.5
					243.50	5.9
					317.65	2.8
					721.38	7.9
$^{191}\text{Pt}$ (0.0)	2.802 d	$\epsilon$ : 100%	$^{191}\text{Ir}(\text{d},2\text{n})$	-4017.0	178.96	12.5
					351.17	42.6
			$^{193}\text{Ir}(\text{d},4\text{n})$	-17988.0	409.44	100
					456.47	42
					538.87	181
					624.06	18.5
$^{193m}\text{Pt}$ (149.783)	4.33 d	IT:100%	$^{193}\text{Ir}(\text{d},2\text{n})$	-3063.5	66.831	7.21
					135.5	0.1145475

Table B.5: Iridium production cross sections produced from Iridium

$E_d$ (MeV)	Production cross section (mb) for iridium radionuclides				
	$^{188m1+g}\text{Ir}_{\text{cum}}$	$^{188m1+g}\text{Ir}_{\text{ind}}$	$^{189}\text{Ir}_{\text{cum}}$	$^{190m1+g}\text{Ir}_{\text{cum}}$	$^{190m1+g}\text{Ir}_{\text{ind}}$
$30.65^{+0.76}_{-0.75}$	$1.37 \pm 0.10$	$0.42 \pm 0.03$	$332.49 \pm 24.20$	$86.65 \pm 2.89$	$85.88 \pm 2.86$
$28.40^{+0.80}_{-0.79}$	$0.45 \pm 0.07$	$0.17 \pm 0.02$	$237.84 \pm 17.44$	$62.80 \pm 2.14$	$62.36 \pm 2.13$
$26.03^{+0.82}_{-0.82}$	$0.34 \pm 0.08$	$0.17 \pm 0.03$	$91.49 \pm 5.47$	$44.26 \pm 1.47$	$44.01 \pm 1.46$
$23.54^{+0.88}_{-0.87}$	-	-	$19.23 \pm 2.65$	$27.29 \pm 1.02$	$27.19 \pm 1.02$
$21.38^{+0.94}_{-0.92}$	-	-	-	$18.73 \pm 0.71$	$18.69 \pm 0.70$
$19.03^{+1.00}_{-0.99}$	-	-	-	$14.02 \pm 0.55$	$14.00 \pm 0.55$
$16.43^{+1.11}_{-1.08}$	-	-	-	$12.40 \pm 0.51$	$12.39 \pm 0.51$
$13.51^{+1.28}_{-1.22}$	-	-	-	$8.26 \pm 0.43$	$8.25 \pm 0.42$
$10.09^{+1.55}_{-1.41}$	-	-	-	-	-
$5.63^{+2.21}_{-1.83}$	-	-	-	-	-

Table B.6: Iridium production cross sections produced from Iridium

$E_d$ (MeV)	Production cross section (mb) for iridium radionuclides			
	$^{190m2}\text{Ir}_{\text{ind}}$	$^{192}\text{Ir}_{\text{cum}}$	$^{194g}\text{Ir}_{\text{cum}}$	$^{194m2}\text{Ir}_{\text{ind}}$
$30.65^{+0.76}_{-0.75}$	$8.87 \pm 0.25$	$188.43 \pm 5.27$	$50.92 \pm 2.18$	-
$28.40^{+0.80}_{-0.79}$	$5.03 \pm 0.15$	$152.55 \pm 4.39$	$51.39 \pm 2.89$	-
$26.03^{+0.82}_{-0.82}$	$2.92 \pm 0.08$	$124.33 \pm 3.42$	$61.37 \pm 2.39$	$0.74 \pm 0.17$
$23.54^{+0.88}_{-0.87}$	$1.16 \pm 0.04$	$100.03 \pm 3.14$	$69.68 \pm 2.76$	$0.68 \pm 0.26$
$21.38^{+0.94}_{-0.92}$	$0.45 \pm 0.01$	$90.41 \pm 2.80$	$86.38 \pm 3.18$	$0.65 \pm 0.13$
$19.03^{+1.00}_{-0.99}$	$0.16 \pm 0.01$	$90.65 \pm 3.01$	$97.79 \pm 3.99$	$0.60 \pm 0.14$
$16.43^{+1.11}_{-1.08}$	0.06 0.00	$99.61 \pm 3.14$	$121.54 \pm 4.54$	$0.50 \pm 0.09$
$13.51^{+1.28}_{-1.22}$	0.03 0.00	$107.41 \pm 3.48$	$143.27 \pm 5.52$	-
$10.09^{+1.55}_{-1.41}$	0.02 0.00	$64.27 \pm 2.56$	$92.78 \pm 4.21$	-
$5.63^{+2.21}_{-1.83}$	0.02 0.00	$6.67 \pm 0.37$	$6.32 \pm 0.42$	-

## B.2 Production cross sections

### B.2.1 ${}^{\text{nat}}\text{Ir}(\text{d},\text{x})$

Table B.7: Platinum production cross sections produced from Iridium

$E_d$ (MeV)	Production cross section (mb) for platinum radionuclides			
	$^{188}\text{Pt}_{\text{ind}}$	$^{189}\text{Pt}_{\text{ind}}$	$^{191}\text{Pt}_{\text{ind}}$	$^{193m}\text{Pt}_{\text{ind}}$
$30.65^{+0.76}_{-0.75}$	$0.94 \pm 0.13$	$486.47 \pm 21.86$	$597.10 \pm 16.55$	$48.11 \pm 6.33$
$28.40^{+0.80}_{-0.79}$	$0.30 \pm 0.09$	$341.24 \pm 16.64$	$483.60 \pm 13.79$	$46.78 \pm 2.19$
$26.03^{+0.82}_{-0.82}$	$0.17 \pm 0.05$	$172.11 \pm 8.03$	$353.99 \pm 9.67$	$55.68 \pm 2.17$
$23.54^{+0.88}_{-0.87}$	-	$30.72 \pm 1.48$	$165.12 \pm 5.15$	$51.79 \pm 2.12$
$21.38^{+0.94}_{-0.92}$	-	$1.04 \pm 0.07$	$71.05 \pm 2.19$	$58.31 \pm 1.96$
$19.03^{+1.00}_{-0.99}$	-	$0.09 \pm 0.02$	$77.53 \pm 2.57$	$77.98 \pm 2.89$
$16.43^{+1.11}_{-1.08}$	-	-	$128.24 \pm 4.03$	$115.33 \pm 4.09$
$13.51^{+1.28}_{-1.22}$	-	-	$137.37 \pm 4.42$	$148.98 \pm 5.54$
$10.09^{+1.55}_{-1.41}$	-	-	$53.45 \pm 2.12$	$56.18 \pm 2.85$
$5.63^{+2.21}_{-1.83}$	-	-	$1.05 \pm 0.06$	$1.56 \pm 0.12$

Table B.8: ....

$E_d$ (MeV)	Production cross section (mb) for ...				
	$^{48}\text{V}_{\text{cum}}$	$^{51}\text{Cr}_{\text{cum}}$	$^{52}\text{Mn}_{\text{cum}}$	$^{54}\text{Mn}_{\text{ind}}$	$^{53}\text{Fe}_{\text{cum}}$
$29.57^{+0.68}_{-0.68}$	$0.12 \pm 0.01$	$7.54 \pm 0.23$	$16.00 \pm 0.36$	$23.85 \pm 0.70$	$5.12 \pm 0.65$
$27.26^{+0.73}_{-0.72}$	$0.09 \pm 0.01$	$7.86 \pm 0.25$	$5.48 \pm 0.16$	$24.18 \pm 0.72$	$2.77 \pm 0.44$
$24.80^{+0.77}_{-0.76}$	$0.06 \pm 0.00$	$8.51 \pm 0.29$	$0.91 \pm 0.03$	$26.12 \pm 0.79$	$1.29 \pm 0.30$

Table B.9: ....

$E_d$ (MeV)	Production cross section (mb) for ...			
	$^{59}\text{Fe}_{\text{ind}}$	$^{55}\text{Co}_{\text{ind}}$	$^{57}\text{Co}_{\text{ind}}$	$^{58}\text{Co}_{\text{ind}}$
$0.16 \pm 0.02$	$27.15 \pm 0.80$	$35.91 \pm 1.06$	$1.50 \pm 0.05$	$29.57^{+0.68}_{-0.68}$
$27.26^{+0.73}_{-0.72}$	$0.15 \pm 0.02$	$20.44 \pm 0.60$	$38.37 \pm 1.13$	$1.62 \pm 0.05$
$24.80^{+0.77}_{-0.76}$	$0.18 \pm 0.04$	$13.82 \pm 0.40$	$42.63 \pm 1.27$	$2.05 \pm 0.07$

Table B.10: ....

$E_d$ (MeV)	Production cross section (mb) for ...					
	$^{59}\text{Fe}_{\text{cum}}$	$^{60}\text{Co}_{\text{cum}}$	$^{61}\text{Co}_{\text{cum}}$	$^{65}\text{Ni}_{\text{ind}}$	$^{61}\text{Cu}_{\text{cum}}$	$^{64}\text{Cu}_{\text{ind}}$
$30.03_{-0.67}^{+0.67}$	$0.21 \pm 0.03$	$9.49 \pm 0.52$	$1.62 \pm 0.09$	$3.42 \pm 1.76$	$4.54 \pm 0.87$	$170.76 \pm 7.76$
$27.74_{-0.71}^{+0.72}$	$0.18 \pm 0.02$	$11.38 \pm 0.51$	$0.82 \pm 0.07$	$3.84 \pm 1.94$	$2.07 \pm 0.95$	$153.78 \pm 8.20$
$25.32_{-0.76}^{+0.77}$	$0.17 \pm 0.02$	$12.02 \pm 0.51$	$0.29 \pm 0.05$	$2.89 \pm 1.48$	$1.18 \text{ pm } 0.72$	$132.56 \pm 6.93$
$22.77_{-0.81}^{+0.83}$	$0.12 \pm 0.01$	$11.36 \pm 0.43$	-	$1.92 \pm 1.14$	-	$121.54 \pm 7.12$
$20.57_{-0.87}^{+0.89}$	$0.07 \pm 0.01$	$9.27 \pm 0.41$	-	-	-	$106.07 \pm 5.81$
$18.14_{-0.94}^{+0.97}$	$0.03 \pm 0.01$	$5.65 \pm 0.26$	-	$1.46 \pm 0.95$	-	$95.92 \pm 7.14$
$15.43_{-1.04}^{+1.08}$	-	$1.53 \pm 0.12$	-	-	-	$123.79 \pm 6.62$
$12.34_{-1.20}^{+1.27}$	-	-	-	-	-	$156.65 \pm 8.20$
$8.68_{-1.43}^{+1.62}$	-	-	-	-	-	$209.38 \pm 11.27$
$3.94_{-2.22}^{+2.25}$	-	-	-	-	-	$73.54 \pm 5.70$

# Bibliography

- [1] Chai-Hong Yeong, Mu-hua Cheng, and Kwan-Hoong Ng. Therapeutic radionuclides in nuclear medicine: current and future prospects. *Journal of Zhejiang University SCIENCE B*, 15(10):845–863, oct 2014.
- [2] M. Shamsuzzoha Basunia. Nuclear Data Sheets for A=193. *Nuclear Data Sheets*, 143:1–381, jul 2017.
- [3] Roger W. Howell, Dandamudi V. Rao, De-Yan Hou, Venkat R. Narra, and Kandula S. R. Sastry. The Question of Relative Biological Effectiveness and Quality Factor for Auger Emitters Incorporated into Proliferating Mammalian Cells. *Radiation Research*, 128(3):282, dec 1991.
- [4] Roger W. Howell. Radiation spectra for Auger-electron emitting radionuclides: Report No. 2 of AAPM Nuclear Medicine Task Group No. 6. *Medical Physics*, 19(6):1371–1383, nov 1992.
- [5] Syed M. Qaim. Nuclear data for production and medical application of radionuclides: Present status and future needs. *Nuclear Medicine and Biology*, 44:31–49, jan 2017.
- [6] E. Browne and J.K. Tuli. Nuclear Data Sheets for A = 137. *Nuclear Data Sheets*, 108(10):2173–2318, oct 2007.
- [7] Yu. Khazov, A. Rodionov, and F.G. Kondev. Nuclear Data Sheets for A = 133. *Nuclear Data Sheets*, 112(4):855–1113, apr 2011.
- [8] M.J. Martin. Nuclear Data Sheets for A = 152. *Nuclear Data Sheets*, 114(11):1497–1847, nov 2013.
- [9] Huo Junde, Huo Su, and Yang Dong. Nuclear Data Sheets for A = 56. *Nuclear Data Sheets*, 112(6):1513–1645, jun 2011.
- [10] Kazimierz Zuber and Balraj Singh. Nuclear Data Sheets for A = 61. *Nuclear Data Sheets*, 125:1–200, mar 2015.
- [11] Caroline D. Nesaraja, Scott D. Geraedts, and Balraj Singh. Nuclear Data Sheets for A = 58. *Nuclear Data Sheets*, 111(4):897–1092, apr 2010.
- [12] Alan L. Nichols, Balraj Singh, and Jagdish K. Tuli. Nuclear Data Sheets for A = 62. *Nuclear Data Sheets*, 113(4):973–1114, apr 2012.
- [13] BAI ERJUN and HUO JUNDE. Nuclear Data Sheets for A = 63. *Nuclear Data Sheets*, 92(1):147–252, jan 2001.
- [14] E. Browne and J.K. Tuli. Nuclear Data Sheets for A = 65. *Nuclear Data Sheets*, 111(9):2425–2553, sep 2010.
- [15] Yang Dong and Huo Junde. Nuclear Data Sheets for A = 52. *Nuclear Data Sheets*, 128:185–314, sep 2015.

## BIBLIOGRAPHY

---

- [16] A. Hermanne, S. Takács, R. Adam-Rebeles, F. Tárkányi, and M.P. Takács. New measurements and evaluation of database for deuteron induced reaction on Ni up to 50MeV. *Nuclear Instruments and Methods in Physics Research Section B: Beam Interactions with Materials and Atoms*, 299:8–23, mar 2013.
- [17] S. Takács, F. Tárkányi, B. Király, A. Hermanne, and M. Sonck. Evaluated activation cross sections of longer-lived radionuclides produced by deuteron induced reactions on natural nickel. *Nuclear Instruments and Methods in Physics Research Section B: Beam Interactions with Materials and Atoms*, 260(2):495–507, jul 2007.
- [18] Ahmed Rufai Usman, Mayeen Uddin Khandaker, Hiromitsu Haba, Masashi Murakami, and Naohiko Otuka. Measurements of deuteron-induced reaction cross-sections on natural nickel up to 24 MeV. *Nuclear Instruments and Methods in Physics Research Section B: Beam Interactions with Materials and Atoms*, 368:112–119, feb 2016.
- [19] N. Amjad, F. Tárkányi, F. Ditrói, S. Takács, and H. Yuki. Activation cross-sections of deuteron induced reaction of natural Ni up to 40MeV. *Applied Radiation and Isotopes*, 82:87–99, dec 2013.
- [20] Yang Dong and Huo Junde. Nuclear Data Sheets for A = 54. *Nuclear Data Sheets*, 121:1–142, sep 2014.
- [21] M. Shamsuzzoha Basunia. Nuclear Data Sheets for A=59. *Nuclear Data Sheets*, 151:1–333, jul 2018.
- [22] Huo Junde. Nuclear Data Sheets for A = 55. *Nuclear Data Sheets*, 109(4):787–942, apr 2008.
- [23] K. Ochiai, M. Nakao, N. Kubota, S. Sato, M. Yamauchi, N. H. Ishioka, T. Nishitani, and C. Konno. Deuteron induced activation cross section measurement for IFMIF. In *ND2007*, Les Ulis, France, may 2007. EDP Sciences.
- [24] M. Avrigeanu, E. Šimečková, U. Fischer, J. Mrázek, J. Novák, M. Štefánik, C. Costache, and V. Avrigeanu. Deuteron-induced reactions on Ni isotopes up to 60 MeV. *Physical Review C*, 94(1):014606, jul 2016.
- [25] S. Takács, M. Sonck, A. Azzam, A. Hermanne, and F. Tárkányi. Activation Gross Section Measurements of Deuteron Induced Reactions on nat Ni with Special Reference to Beam Monitoring and Production of for 61Cu Medical Purpose. *Radiochimica Acta*, 76(1-2), jan 1997.
- [26] J. Zweit, A.M. Smith, S. Downey, and H.L. Sharma. Excitation functions for deuteron induced reactions in natural nickel: Production of no-carrier-added 64Cu from enriched 64Ni targets for positron emission tomography. *International Journal of Radiation Applications and Instrumentation. Part A. Applied Radiation and Isotopes*, 42(2):193–197, jan 1991.
- [27] M.R. Bhat. Nuclear Data Sheets for A = 57. *Nuclear Data Sheets*, 85(3):415–536, nov 1998.
- [28] Caroline D. Nesaraja, Scott D. Geraedts, and Balraj Singh. Nuclear Data Sheets for A = 58. *Nuclear Data Sheets*, 111(4):897–1092, apr 2010.
- [29] E. Browne and J.K. Tuli. Nuclear Data Sheets for A = 60. *Nuclear Data Sheets*, 114(12):1849–2022, dec 2013.
- [30] E. Browne and J.K. Tuli. Nuclear Data Sheets for A = 65. *Nuclear Data Sheets*, 111(9):2425–2553, sep 2010.
- [31] Balraj Singh. Nuclear Data Sheets for A = 64. *Nuclear Data Sheets*, 108(2):197–364, feb 2007.
- [32] Mayeen Uddin Khandaker, Hiromitsu Haba, Masashi Murakami, Naohiko Otuka, and Hasan Abu Kassim. Deuteron-induced activation cross-sections on natural copper up to 24 MeV. *Journal of Radioanalytical and Nuclear Chemistry*, 302(2):759–764, nov 2014.

- [33] S. Takács, F. Tárkányi, B. Király, A. Hermanne, and M. Sonck. Evaluated activation cross sections of longer-lived radionuclides produced by deuteron-induced reactions on natural copper. *Nuclear Instruments and Methods in Physics Research Section B: Beam Interactions with Materials and Atoms*, 251(1):56–65, sep 2006.
- [34] M. Nakao, J. Hori, K. Ochiai, N. Kubota, S. Sato, M. Yamauchi, N.S. Ishioka, and T. Nishitani. Measurements of deuteron-induced activation cross-sections for IFMIF accelerator structural materials. *Nuclear Instruments and Methods in Physics Research Section A: Accelerators, Spectrometers, Detectors and Associated Equipment*, 562(2):785–788, jun 2006.
- [35] Mirko Dikšić, Jean-Louis Galinier, Heather Marshall, Leo Yaffe, Robert B. Moore, and Dallas C. Santry. Absolute cross sections for  $^{64}\text{Cu}$  and  $^{61}\text{Cu}$  produced by deuteron-induced reactions in copper. *Nuclear Instruments and Methods*, 159(1):171–175, feb 1979.
- [36] E. Šimečková, P. Bém, M. Honusek, M. Štefánik, U. Fischer, S. P. Simakov, R. A. Forrest, A. J. Koning, J.-C. Sublet, M. Avrigeanu, F. L. Roman, and V. Avrigeanu. Low and medium energy deuteron-induced reactions on  $\text{Cu}_{63}^{65}$  nuclei. *Physical Review C*, 84(1):014605, jul 2011.
- [37] F. O. Bartell, A. C. Helmholz, S. D. Softky, and D. B. Stewart. Excitation Functions for Spallation Reactions on Cu. *Physical Review*, 80(6):1006–1010, dec 1950.
- [38] C.B. Fulmer and I.R. Williams. Excitation functions for radioactive nucleides produced by deuteron-induced reactions in copper. *Nuclear Physics A*, 155(1):40–48, oct 1970.